Norwegian University
of Life Sciences

Master's Thesis 2019 30 ECTS
Faculty of Science and Technology

The Performance of Household PV Systems in Southeastern Norway

Aksel Pettersen
Environmental Physics and Renewable Energy

Preface

This study of the photovoltaic (PV) system performance in southeastern Norway was done in collaboration with Institute for Energy Technology (IFE) and Sivilingeniør Carl Christian Strømberg AS in the period January to May 2019. This thesis is a part of the engineering degree in Environmental Physics and Renewable Energy at Norwegian University of Life Sciences (NMBU) as a part of the Master's program Environmental physics and renewable energy.

First, I want to thank Josefine Selj, my supervisor at IFE, for giving me the opportunity to dig deep into the PV system performance, for your guidance, and for your honest feedback. I also want to thank Espen Olsen, my supervisor at NMBU for helping me with the thesis. Second, I want to thank Mari Øgaard for your patience when answering all my questions and for helping me with the writing. A final thank to Lisa Kvalbein for answering my question regarding Apelsvoll weather station.

I will also thank Helene Tømmerbakken and Sivilingeniør Carl Christian Strømberg AS for answering all my questions, for helping me with the test of the inverter, and for providing the data. This would not be possible without you.

I will also thank my friends at NMBU for all the interesting conversation, discussions, and excursions. The last five years would not have been the same without you, and I am happy for all the memories. A special thank to my father and mother the endless support, and Marianne Fredhjem for the endless patience and positivity the last semester. This would be much harder to complete without you.

Ås, May 2019

Aksel Pettersen

Abstract

The recent price reduction of rooftop photovoltaic (PV) systems has led to an increased the demand in Norway. However, poor system design and modelling may cause the system cost to increase and the system credibility to decrease. To prevent this, it is important to illuminate the system performance, to assess the models used to estimate in-plane irradiance, to study the effect of data used in the models, and to assess loss factors connected to the systems.

The purpose of this thesis is to assess the performance of rooftop PV systems in southeastern Norway. This starts with an assessment of the available irradiance models to ensure quality and improve the accuracy of the PV system performance evaluation. The second part is to find out whether it is possible to use irradiance data collected in another location compared to the PV systems. The third part is the performance evaluation of the individual PV systems and their loss factors, before the orientation dependent performance is being investigated in the fourth part. In the final part, the performance of the inverters was assessed to further study the loss factors present in the systems.

Based on the evaluation of irradiance models in the period December to March, the Dirint/Isotropic model combination got the lowest *RMSE* with a value of 24.48 W/m^2 compared to 27.28 W/m^2 for the Disc/Isotropic model combination, and 28.04 W/m^2 for the Dirint/Perez model. The higher performance of the Isotropic sky model is connected to the low irradiance in Norway, especially during the winter period, that is suitable for the Isotropic model. The Dirint decomposition model had the best performance explained by the larger data set used to determine the empirical coefficients.

The study has also shown that it is possible to use irradiance data collected from other areas. However, it is important to note that the uncertainty increase towards winter, and that the local environment and climate impact the result.

Although large uncertainty, the PR_{corr} is above 0.8 for most systems in large periods of

the year. The total PR is however greatly reduced due to the low production during the winter months as there are available irradiance but close to zero production. *PR* was also shown to be in the same range of performance ratios reported by other assessments.

Due to the large measurement uncertainty of the inverters and the pyranometers, and the environment differences between PV and pyranometer locations, it is not possible to conclude whether the performance is different between systems oriented east compared to west, or not. The comparison of total PR_{corr} did not show any evidence of better performance for east faced systems compared to west. This is explained by the large impact of the low production on the performance during the winter months. However, comparing monthly values during the summer period showed higher PR_{corr} of systems oriented to the east compared to systems in the west.

The inverter study confirmed that the inverter performance correspond to the performance characteristics that are given by the producer, and that the inverter performance was predominantly above 95%. The inverter test show a better specific yield of the largest inverter string. Although the difference in specific yield, it is not possible to confirm the hypothesis as the inverter reading uncertainty is to high.

Sammendrag

De siste årenes pris reduksjon for solcellesystem har økt etterspørselen for slike systemer i Norge. Dårlig design og modellering kan imidlertid øke prisen og kredibiliteten for systemene. For å unngå dette er det viktig å belyse solcellesystemers ytelse, vurdere modellene som blir brukt til å estimere innstråling i planet, studere hvilken effekt data som er målt i et annet område har på resultatet av PV system ytelsen, og å vurdere tapsfaktorer tilknyttet systemene i Norge.

Formålet med denne avhandlingen er derfor å vurdere ytelsen til solcellesystemer installert på tak i sør-øst Norge. Dette starter med en vurdering av de tilgjengelige innstrålingsmodellene for å sikre kvalitet og minske usikkerheten til systemytelse evalueringen. Del to er å evaluere om bruk av data målt på en annen lokasjon kan brukes til å evaluere ytelsen til solcellesystem. I del tre vil ytelsen til 12 forskjellige solcellesystem bli evaluert samt tapsfaktorer og andre usikkerhetsmoment, før en evaluering av ytelsens avhengighet av orientering. Til slutt vil omformerne bli studert for videre evaluering av tapsfaktorer i systemet.

Evaluering av innstrålingsmodellene i perioden desember til mars viste at dekomponeringsmodellen Dirint og den Isotropiske transponeringsmodellen hadde minst $RMSE$ på 24.48 W/m^2 sammenliknet med 27.28 W/m^2 for modelkombinasjonen Disc/Isotropic og 28.04 W/m^2 for modelkombinasjonen Dirint/Perez. Den høyere ytelsen til modelkombinasjonen Dirint/Isotropisk kan knyttes til den lave innstrålingen i Norge, spesielt på vinteren noe som kan være gunstig ved bruk av modelkombinasjonen Dirint/Isotropisk.

Studien viser også at det er mulig å bruke data fra en annen lokasjon. Det er imidlertid viktig å påpeke at usikkerheten øker dess nærmere vinteren og at lokale variasjoner påvirker resultatet.

Generelt sett er PR_{corr} over 0.8 for de fleste systemer i store perioder av året. Den totale PR_{corr} blir sterkt påvirket av den lave produksjonen i vintermånedene, selv om sollys er til stedet. Systemenes PR var også vist til å være i samme område som rapporterte ytelser i andre

systemevalueringer.

På grunn av den høye usikkerheten knyttet til omformerne og pyranometerne, og lokale ulikheter mellom lokasjonen til PV system og pyranometer, er det ikke mulig å konkludere om det faktisk er en forskjell på ytelsen til systemer orientert mot øst sammenliknet med systemer orientert mot vest. Dette forklares med en stor reduksjon av PR_{corr} i vintermånedene. Sammenlikning av månedlige verdier i sommerperioden viste at de kalkulerte verdiene til østvendte system er større enn vestvendte system. Det er imidlertid umulig å konkludere om det faktisk er en forskjell pga. den nevnte måleusikkerheten.

Studien av omformerne bekreftet at omformerytelsen korresponderer med dens karakteristikk gitt av produsenten. Evalueringen viste også at virkningsgraden til omformerne er over 95% i store deler av tiden. Invertertesten viste at den spesifikke ytelsen er størst for strenger med mange moduler sammenliknet med en streng av få moduler. Også her er usikkerheten for stor til å konkludere om det faktisk er en forskjell mellom strengene.

Nomenclature

Abbreviations

Symbol	Description	Unit
AC	Alternating current	–
AM	Air Mass	–
BAPV	Building attached photovoltaic	–
CEC	Calefornian Energy Comission	–
DC	Direct current	–
DHI	Diffuse horizontal irradiance	–
DNI	Direct normal irradiance	–
EDNI	Extra terrestrial direct normal irradiance	–
FF	Fill Factor	–
GHG	Greenhouse gas	–
GHI	Global horizontal irradiance	–
mpp	maximum power point	–
mppt	maximum power point tracker	–
oc	open circuit	–
POA	Plane of Array	–

POA	Point of Array	–
PV	Photovoltaic	–
SCR	Space Charge Region	–
STC	Standard Test Condition	–

Constants

Symbol	Description	Unit
h	Planck's constant	$6.626069 \cdot 10^{-34}$ Js

Symbols

Symbol	Description	Unit
α_1	Upper limit for the difference between measured and estimated mean GHI (Clear sky model)	W/m^2
α_2	Upper limit for the difference between measured and estimated max GHI (Clear sky model)	W/m^2
α_3	Lower limit of the Line length (Clear sky model)	
α_4	Upper limit of the Line length (Clear sky model)	–
α_5	Upper limit of the standard deviation of the rate of change (Clear sky model)	
α_6	Upper limit between for the difference between the change of measured and estimated GHI (Clear sky model)	W/m^2
α_7	Number of hours taken into account (Clear sky model)	hr
α_8	Number of itterations	–
β	DNI fraction of total irradiance	–
β_{Erbs}	Fraction of DHI	–
η	Angle	$^\circ$

η	Efficiency	%
γ	Temperature Coefficient of the PV Power	%/°C
θ	Angle	°
A	Anisotropy index	–
a	Empirical factor connected to the angle between the Sun and module normal vector (Perez model)	–
a_2	Empirical coefficient of the upper limit of T_{cell} under low wind high irradiance	–
AM	Air mass	–
b	Empirical factor connected to the angle between zenith angle and angle of incident (Perez model)	–
b_2	Empirical coefficient of the rate of change of T_{cell} dependent on wind speed	$(m/s)^{-1}$
E	Energy	eV or J
f	frequency	Hz
F_1	Circumsolar Brightening Coefficient (Perez model)	–
F_2	Horizon Brightening Coefficient (Perez model)	–
G	Irradiance	W/m^2
I	Electrical current	A
I_{ph}	Photogenerated current	A
K_n	Direct beam transmittance	–
K_T	Global horizontal transmittance	–
k_T	Clearness index	–
L	Line length (Clear sky model)	–

N	Number of data points	–
n_1	ideality factor of diode 1	–
n_2	ideality factor of diode 2	–
P	Power	W
PR	Performance Ratio	%
R	Resistance	Ω
r	Fraction of POA DNI of GHI	–
$rMSE$	root mean square error	W/m^2
T	Temperature	°C or K
V	Voltage	V
v	Wind speed	m/s
X	Dirint modification factor	–
Y	Yield	kWh
y	Specific yield	kWh/kW_p

Subscripts

Symbol	Description
A	Ambient
a	Azimuth
bs	Back-side
$corr$	Temperature corrected
d	diode
E	Estimated

e	Elevation
G	Band gap
HD	Hay-Davies
I	Isotropic
i	time period i
M	Measured
max	Maximum
n	Angle of incidence
o	Orientation
P	Perez
P	peak
p	Parallel
ph	photon
$rated$	name plate rating
s	Series
t	Tilt
tot	Total
$x\%$	x% of given tilt or orientation
z	Zenith

Contents

1 Introduction

Up till now, fossil fuels have been the main source of energy powering an incredible economic growth. However, the use of fossil fuels has also led to an accumulation of carbon dioxide in the atmosphere, as seen in figure 1.1[1]. There is a scientific consensus for the connection between an increased CO_2 concentrations from human activities and global warming[2], resulting in an increasing global mean temperature, melting ice caps, a rising sea level, and an increased frequency of extreme weather events[3]. Consequently, most countries of the world came together and negotiated the Paris agreement stating that the global average temperature increase should be prevented to exceed two degrees[4].

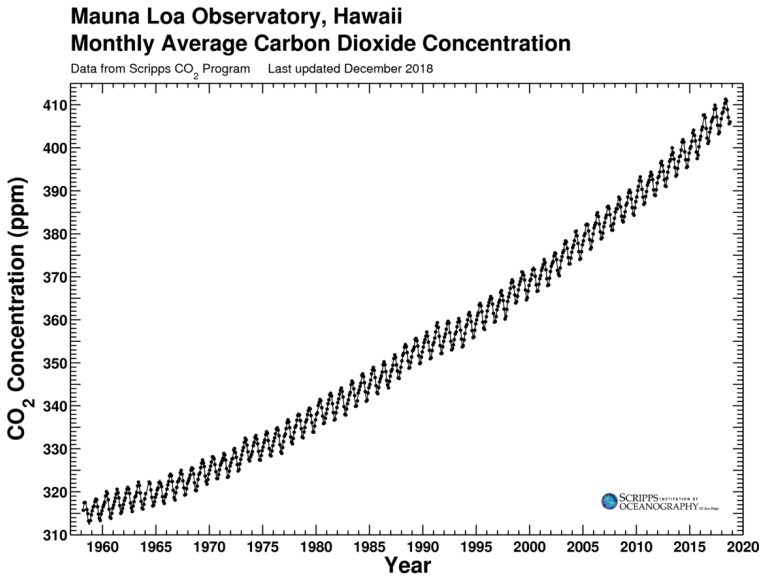

Figure 1.1: *The Keeling curve depicting the increasing CO_2 concentration in the atmosphere observed at the Mauna Loa observatory, USA. Taken from [1].*

As seen in figure 1.2, electricity and heat production is the largest source of emissions of greenhouse gasses (GHG) and according to Enerdata, global energy consumption is increas-

ing[5]. This calls for an energy transition to reduce the emissions, and photovoltaic (PV) energy conversion technologies is one promising technology.

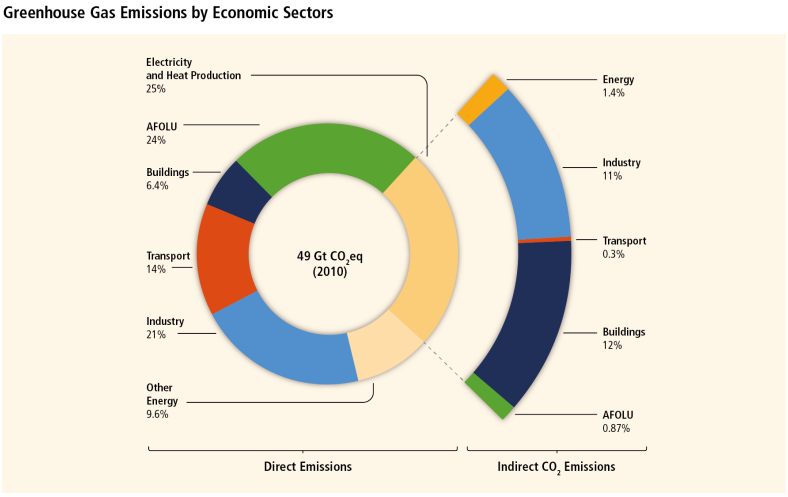

Figure 1.2: *The distribution of global GHG emissions ($GtCO_2eq./year$) dependent on sector. Electricity and heating is the largest fraction describing indirect emissions from for example energy production, transportation, and industry. The chart is taken from [6]*

The global PV market is rapidly growing and 96 MW_p was installed in 2017 corresponding to a 26% increase compared to 2016[7]. Considering that solar PV systems convert solar irradiance to electrical energy, the system performance is directly linked to the system's location. Areas with high irradiation, such as the Sahara desert, are more suited for this purpose compared to Norway. Despite this, the popularity of solar energy is increasing in Norway due to the cost reduction in the recent years. From 2011 to 2016, the cost of residential PV systems has been reduced by 40-60% and the installed capacity has increased by 164%[8].

To utilise the available space and reduce the emissions per kWh produced electrical energy from solar energy systems it is required to improve the system design process and increase the system performance. This leads to the purpose of this thesis. The first purpose is to investigate the performance of PV systems installed on private houses to illuminate the feasibility of PV systems in Norway. The second purpose is to investigate if PV systems oriented to the east has a better performance compared to systems oriented to the west. This assessment is to provide installers the necessary information for installing the best systems possible. To achieve a good performance evaluation, it is necessary to evaluate the irradiance model performance. These models are used to decompose and transpose irradiance data to available irradiance for

the PV systems to harvest. This is important for securing the quality of the study and as the performance of the irradiance models in Norwegian conditions is unknown. Finally, the inverter performance will be evaluated to investigate the losses connected to the inverter, and hence increase the credibility of PV systems in Norway.

This is accomplished by studying irradiance data from multiple weather stations located in the southeastern part of Norway. This data is decomposed and transposed and compared to measured values to asses the quality of irradiance models. Furthermore, different meteorological stations are used for comparison to see if PV systems can be analysed with irradiance data collected from another location. Finally, the performance of household PV systems is assessed by studying 12 systems located in the Southeastern part of Norway, before the inverter performance is studied in the end.

Research on grid-connected PV system performance dependent on orientation and angle has not yet been done. However, research from M. Adaramola et al. and A. Imenes et al. have indicated well-suited conditions in the southern part of Norway for harvesting solar energy[9][10]. There has been no larger study of inverters under Norwegian climates, but M. Adaramola's study showed an annual average inverter efficiency of 88.8%[9] for a system oriented to the south.

2 Theory

The purpose of this chapter is to provide the basic knowledge needed for understanding this thesis. The following content is mainly taken from the books *Solar Energy*[11] and *Physics of solar cells*[12], and the web page *PVeducation*[13], while all other sources are specified.

2.1 The solar resource

In the focus of Earth's ellipsoid orbit, with the mean distance of 149,6 million kilometers, is the Sun. Fuelled by Nuclear fusion, the temperature of the Sun holds about 5800 °C and it irradiates approximately $6.4 \cdot 10^7$ W/m^2 which is dispersed into space.

Due to Earth's size and distance to the Sun, as illustrated in Figure 2.1, only a small fraction of the solar irradiance hits the Earth, and an even smaller fraction is available for harvesting. At Earth's atmosphere, only 1361 W/m^2 is available. This is called the *Solar constant* which is defined as the total irradiance of the Sun at the mean distance on a plane perpendicular to the Sun outside Earth's atmosphere.

The total irradiation at a horizontal surface on Earth is called *Global Horizontal Irradiance*

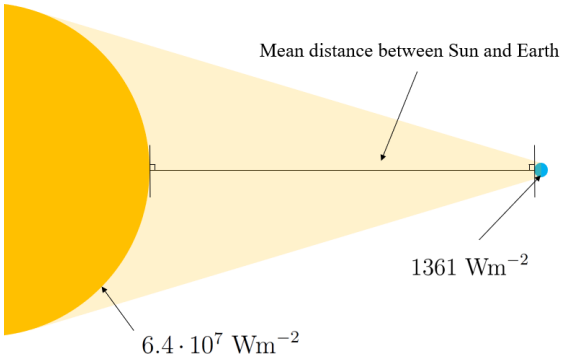

Figure 2.1: *A figure of what the solar constant is, and its size compared to the intensity at the surface of the Sun.*

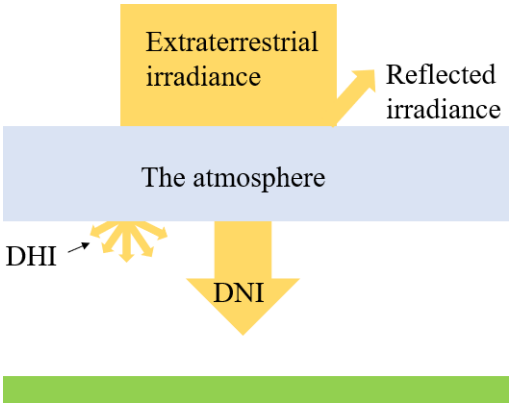

Figure 2.2: *An illustration of DNI and DHI from the extraterrestrial irradiation. DNI is the fraction of irradiance coming directly from the Sun, while DHI is scattered in all directions. The sum of DNI and DHI equals GHI.*

(GHI), and can be divided into *Direct Normal Irradiance* (DNI) and *Diffuse Horizontal Irradiance* (DHI). DNI is the fraction of sunlight which comes directly from the Sun, whereas DHI is the fraction of the irradiance which is scattered in all directions by the atmosphere (see Figure 2.2). Two of the scattering mechanisms are *Rayleigh scattering*, caused by molecules and it mainly affects the high energy irradiation, and *Mie scattering*, caused by larger particles such as dust and aerosols.

2.1.1 Air mass

The attenuation of the solar irradiation through the atmosphere is dependent on the path length that depends on the time of the day and the time of the year. This attenuation is quantified by the *air mass* (AM) factor. The air mass factor is defined as the fraction of atmosphere the photons travel through at a given time and location, compared to the fraction of atmosphere when the Sun is in the *zenith* position under clear sky conditions (illustrated in Figure 2.3). Air mass can be estimated in different ways, and Kasten and Young[14] defined *relative air mass* (refraction corrected air mass) as

$$AM = \frac{1}{\cos(\theta_z) - 0.50572(96.07995 - \theta_z)^{-1.6364}}, \tag{2.1}$$

where θ_Z is the angle between the zenith and the Sun.

One standard frequently used is called *AM1.5*. AM1.5 is defined as the spectrum received by a 37° tilted plane on a clear day, and it corresponds to 1000 W/m^2.

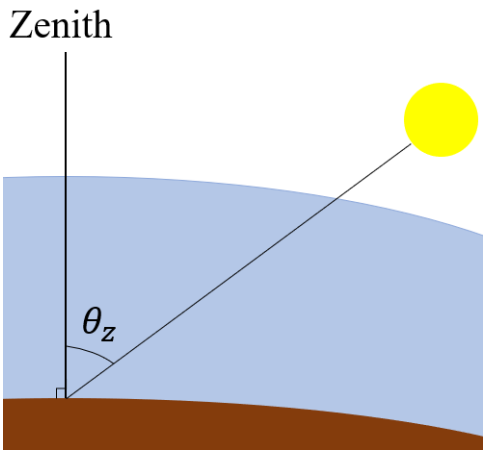

Figure 2.3: *A sketch of the paths of the solar irradiation at zenith position and at an arbitrary position, and the angle, θ_z, that separates them.*

2.1.2 The solar spectrum

The solar spectrum is the power density dependent on the wavelength emitted from the Sun. The *Blackbody spectrum* is depicted in Figure 2.4, which is the irradiance spectrum from a black body as stated by the *Planck law*. Given a specific temperature, a body irradiates different amounts of energy depending on the wavelength, as seen in the same figure. The yellow area is the spectrum that reaches the atmosphere while the red area is the irradiance that reaches the surface of the Earth.

As the light travels through the atmosphere, it is attenuated due to absorption and reflection. Molecules such as Hydrogen gas (H_2) and Carbon dioxide (CO_2) absorb and reflect light in different wavelength ranges (as seen in Figure 2.4) resulting in less energy available at the terrestrial surface.

2.1.3 Irradiation on a tilted plane

Figure 2.5 and 2.6 depict the relevant angles describing a PV system (PV systems will be described in section 2.3), and the incoming irradiance. The module is described by the tilt, θ_t, and the orientation, Ψ_o, while the Sun's position on the sky is described by the elevation from the horizon, θ_e, and the azimuth, Ψ_a. The orientation of 0° is defined as North, 90° as east, 180° as south, and 270°as west. The solar position relative to the PV module is described by the angle of incidence (angle between the module's normal vector and the Sun-module vector),

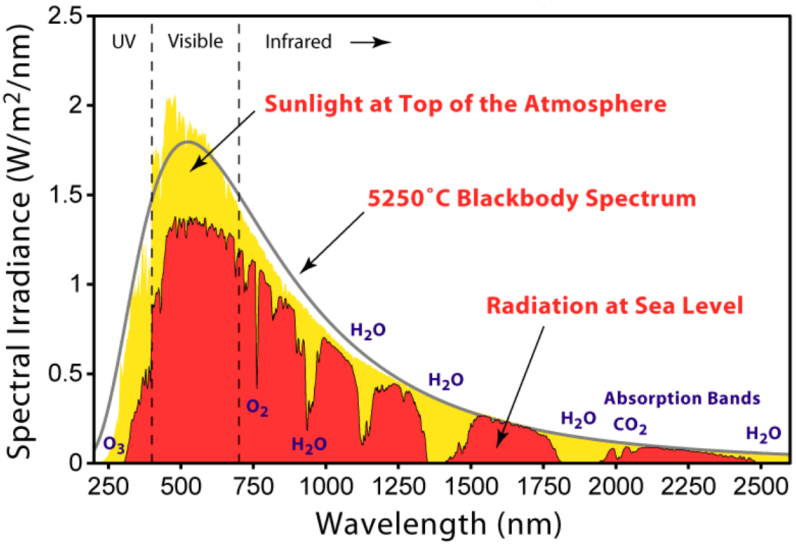

Figure 2.4: *A depiction of the solar irradiance as a black body, at the top of the atmosphere and at sea level. The AM1.5 spectrum is similar to the red are in the figure. The picture is Robert A. Rohde's work and it is taken from [15].*

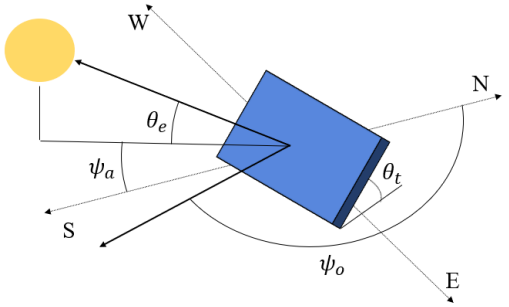

Figure 2.5: *A sketch showing the angles describing the orientation of the module and position of the Sun. Ψ_o is the orientation angle where north equals 0°, Ψ_a is the solar azimuth angle, θ_t is the angle between the horizon and the module, and θ_e is the elevation angle between the irradiance and the horizon.*

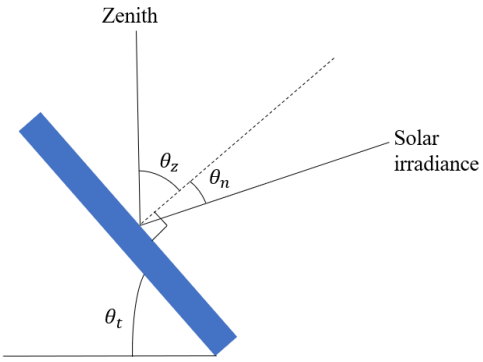

Figure 2.6: *The angles describing the irradiance on the PV module. θ_n is the angle between the solar irradiance and the module's normal vector, and θ_z is the angle between incoming irradiance and zenith.*

θ_n, and the azimuth angle, Ψ_a.

2.1.4 Decomposition and transposition models

Decomposition and *transposition* models are needed to transform the GHI data into *plane of array* (POA) irradiance. POA irradiance is the irradiance in the plane of, for example, the PV module. Decomposition is to transform GHI to DNI and DHI, and transposition is to project horizontal irradiance to POA irradiance. There are many solutions to this problem. Based on available models in PVlib and their simplicity, the following decomposition models were chosen: the Erbs model, the DISC model, and the Dirint model. There are also several transposition models available in PVlib, and the following models were chosen: the Isotropic model, the Hay-Davies model, and the Perez model. The Isotropic model was chosen due to its simplicity and because few input parameters are needed. The Hay-Davies model was chosen due to its performance in the assessment by W. Hayes et al.[16]. The Perez model was chosen based on its complexity and that many input parameters are needed. All models are listed below.

Decomposition models:

- Erbs model
- DISC model
- Dirint model

Transposition models:

- Isotropic model
- Hay-Davies model
- Perez model

2.1.4.1 Solar position

The solar position is needed to calculate the DNI and DHI, and National Renewable Energy Laboratory's (NREL) algorithm *Solar Position Algorithm for Solar Radiation Applications*[17] is used in this thesis. It is based on Meeus' description[18] from 1998, and it provides an algorithm for solar position estimation from year -2000 to 6000 with a uncertainty of ±0.0003°[17]. This algorithm calculates the solar azimuth, elevation, and zenith.

2.1.4.2 Decomposition models

The Erbs model

D. G. Erbs et al. developed a correlation based model to estimate hourly DHI from hourly GHI by using its relationship to the *clearness index*, k_T[19]. The clearness index is a metric of how clear the sky is (i.e. how much scattered light), and Erbs et al. used data collected from four sites in the US to estimate the fraction of DHI, β_{Erbs}, by using the correlation between GHI and k_T. The results were compared to a similar study done in Australia by J. F. Orgill et al.[20], which were found to be similar. The equation developed is

$$G_{Erbs,DHI} = G_{GHI}\beta_{Erbs}, \tag{2.2}$$

where $G_{Erbs,DHI}$ is the DHI estimated by the Erbs model, G_{GHI} is the GHI, and β_{Erbs} is the fraction of DHI of the total irradiance.

The DISC model

The *Direct Insolation Simulation Code* (DISC) model use the relationship between *Direct beam transmittance*, K_n, and *effective Global horizontal transmittance*, K_t, to calculate the hourly DNI from hourly GHI. K_n is the fraction of DNI at the surface of the Earth to the extraterrestrial DNI, while K_t is the ratio between GHI and extraterrestrial GHI. Those two factors are dependent on air mass, cloud cover, water in the atmosphere, and albedo (a factor of how much the ground reflects the total irradiance). The air mass, which is the dominant force that affects the relationship between global and direct irradiation according to the study, is used in Bird's physical clear sky model to calculate the direct component as a reference used to calculate the change of the direct irradiance component. The data was again fit to a polynomial to give a relationship between K_n and air mass.

Secondly, two data sets collected from two meteorological stations located 20 miles apart were plotted against air mass, and an exponential function was fit to the data. The coefficients of the exponential function were determined by finding a correlation to K_t.

Finally, the DNI is calculated by equation

$$G_{DISC,DNI} = G_{GHI}K_n, \tag{2.3}$$

where $G_{DISC,DNI}$ is the DNI estimated by the DISC model.

The Dirint model

The *Dirint* model is a development from the DISC irradiance model by P. Ineichen et al.[21] as shown in the following equation

$$G_{Dirint,DNI} = G_{DISC,DNI}X, \tag{2.4}$$

where $G_{Dirint,DNI}$ is the DNI estimated by the Dirint model, and X is a factor that modifies the DISC irradiance model. This model differs from the DISC by using GHI, time, location, and surface dew-point temperature to calculate X. Additionally, the model is derived from a larger data set collected from different climate conditions located in North America and Europe.

2.1.4.3 The connection between GHI, DNI, and DHI

Since the models above only estimates either DNI or DHI, the last component is needed to be calculated. That is done by the relation

$$G_{GHI} = G_{DHI} + G_{DNI}\sin(\theta_e), \tag{2.5}$$

where θ_e is the elevation angle of the Sun with respect to the horizon.

2.1.4.4 Transposition models

The Isotropic model

The *isotropic* model was developed by H.C. Hottel et al.[22] that assumed uniformly spread diffuse irradiation over the celestial sphere (zero circumsolar brightening and horizontal brightening) and all ground reflected light is diffuse. The total irradiation is then calculated by

$$G_{tot,I} = G_{DNI}r + G_{DHI}(\frac{1+\cos(\theta_t)}{2}) + G_r(\frac{1-\cos(\theta_t)}{2}), \tag{2.6}$$

where $G_{tot,I}$ is the total POA irradiance estimated by using the Isotropic model, r is a ratio describing the DNI on a tilted surface compared to the horizontal irradiance, G_{DHI} is the DHI, G_r is the ground reflected irradiance dependent on the albedo, and θ_t is the plane's tilt with respect to the horizontal surface.

The Hay-Davies model

The model described by Hay and Davies[23] is similar to the Isotropic sky model, except that it divides the irradiation from the celestial sphere into isotropic and *circumsolar brightening*, a brightening effect around the Sun.

The equation for total irradiance given by P.G. Loutzenhiser et al. [24] with reference to [23] is

$$G_{tot,HD} = (G_{DNI} + G_{DHI}A)r + (1-A)G_{DHI}(\frac{1+\cos\theta_t}{2}) + G_r(\frac{1-\cos\theta_t}{2}), \tag{2.7}$$

where $G_{tot,HD}$ is the total POA irradiance estimated by using the Hay-Davies model. A is the *Anisotropy index* which is the fraction of direct normal irradiance of DHI caused by the brightening effect around the Sun.

The Perez model

The *Perez* model was derived by Perez et al.[25], and it is similar to both the Isotropic and the Hay-Davies model, but it also includes horizontal brightening, a brightening effect at the horizon. Perez also developed other factors for estimating the different brightening effects. P.G. Loutzenhiser et al.[24] presented the following equation for the Perez model

$$G_{tot,P} = G_{DNI}R + G_{DHI}\left[(1-F_1)\frac{1+\cos\theta_t}{2} + F_1\frac{a}{b} + F_2\sin\theta_t\right] + G_r\frac{1-\cos\theta_t}{2}, \tag{2.8}$$

where $G_{tot,P}$ is the total POA irradiance estimated by the Perez model, F_1 is the *Circumsolar brightening coefficient*, F_2 is the *Horizon brightening coefficient* both which is derived from empirical data. Finally, a and b is factors that take the angle between the Sun and the normal vector of the plane, θ_n, and the zenith angle, θ_z, into account.

2.1.4.5 Clear sky detection

M. J. Reno and C. W. Hansen developed a method to detect clear sky days[26]. This algorithm compares typical clear sky values with the measured values to detect periods of clear sky. For a period to be defined as clear, it needs to pass five criteria:

- measured mean GHI must not differ the clear sky mean GHI by more than a limit ($\alpha_1 \leq 75\ \frac{\mathrm{W}}{\mathrm{m}^2}$ by default).

- measured max GHI must not differ the clear sky max GHI by more than a limit($\alpha_2 \leq 75\ \frac{\mathrm{W}}{\mathrm{m}^2}$ by default).
- *Line length*, a metric describing the variability of the data (the more variability the larger line length) that must be within a certain range ($\alpha_3 \leq L \geq \alpha_4$, where $\alpha_3 = -5$ and $\alpha_4 = 10$ by default).
- The standard deviation of the rate of change (a metric of how variable the irradiance is through the day) must be lower than a certain limit ($\alpha_5 \leq 0.005$ by default).
- The difference between the change of measured and estimated GHI of two time steps must be under a certain limit ($\alpha_6 \leq 8\ \frac{\mathrm{W}}{\mathrm{m}^2}$ by default).

The estimated clear sky GHI values were obtained by Ineichen and Perez's algorithm [27][28] with the zenith position of the Sun, air mass, *Linke Turbidity* (a metric describing the fraction of light that is absorbed and scattered in the atmosphere), altitude, and Extraterrestrial DNI (EDNI) as input.

2.2 Fundamentals of photovoltaic energy conversion

2.2.1 The principles of semiconductor materials

In the core of PV energy conversion lies the semiconductor material. The semiconductor is different from other materials, such as metals and insulators, by having an intermediate sized gap between the *conduction band* and the *valence band*. The conduction band in an ideal semiconductor is defined as the energy state where no electrons are located at 0 K, while the valence band is defined as the upper energy state occupied by electrons at 0 K. At this temperature, all electrons are bound to the material unable to move, resulting in zero current. At higher temperatures, however, some electrons are energetic enough to excite into the conduction band where they are free to move. It is the difference between the valence band and the conduction band, also called the *Band gap*, that determines how many electrons at a certain temperature that are free to move. The explanation is that there are no energy states for electrons to occupy, and thus only electrons excited by the energy equal to, or larger than, the band gap energy to be

located in the conduction band. It is these electrons in the conduction band that contributes to the current in the semiconductor material.

2.2.1.1 Doping

Doping is a method used to increase the number of free electrons, or holes, in a semiconductor material to increase conductivity and current. This is done by adding an atom with one, or more, electrons, or holes, than the original material. For example, if Silicon is doped with Phosphorous, a Silicon atom is replaced by a Phosphorous atom. Four of the Phosphorous atom's five valence electrons bonds with the neighbouring Silicon, while the last electrons are bound to the Phosphorous atom. This binding is weak, and thus, by adding energy, it is easily freed from the atom where it can move in the crystal lattice. Conversely, if Boron is added, a Silicon atom is replaced by a Boron atom. Since Boron only has three valence electrons, only three of the neighbouring atoms can form bindings. However, a neighbouring atom can, by adding energy available at room temperature, break a bound to another neighbouring Silicon atom to bind with the Boron atom creating another hole. Holes are in this way able to move around in the crystal lattice. This is called n-, and p-doping respectively.

2.2.2 Photovoltaic effect

Another important phenomenon is the conversion of solar irradiance into electrical energy by utilising the *Photovoltaic effect*. The Photovoltaic effect is the process of absorbing *photons* that excite electrons into another material generating a voltage between the materials. A photon is light described as an energy package with energy given by the equation

$$E_{ph} = hf, \tag{2.9}$$

where E_{ph} is the photon energy, h is Planck's constant, and f is the frequency of the light wave. Photons are emitted by light sources in a range of wavelengths dependent on the temperature of the light source as previously discussed.

For a photon to be absorbed by the semiconductor material, the photon energy must be equal to, or larger than, the band gap energy, E_G, of the particular cell material. For example, Silicon material has a band gap of 1.12 eV resulting in no absorption of photons that have lower

energy. The excess energy ($E_{ph} - E_G$) is also lost, and it will be further discussed in section 2.2.4.

2.2.3 The photovoltaic cell

A photovoltaic cell is constructed by a n-doped and p-doped semiconductor material put together into a *PN junction*. At this junction, immediately after the connection, electrons from the n-doped side and holes from the p-doped side diffuse over to the other material and recombine leaving charged atomic cores behind. These charges create an electric field, often called the *Built-in field*, from the n-doped material to the p-doped material. The area it extends is called the *Space charge region* (SCR), and it is illustrated in Figure 2.7. At equilibrium, this field prevents more holes from entering the n-doped side and vice versa.

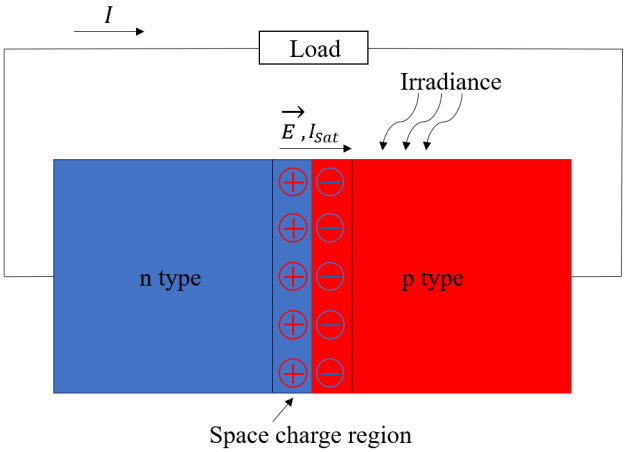

Figure 2.7: *A sketch of a PN junction with the SCR, the different currents and field, and their directions.*

The silicon PV cell produces energy by absorbing light. The absorbed Photons generate minority carriers that move over to the other material in the PN-junction. These minority carriers can be utilised as electrical energy if an external circuit is connecting the two materials in the PN-junction.

2.2.3.1 Current, voltage, and power

The voltage produced by the solar cell is a consequence of the band gap of the material in use, doping, and the field inside the cell, and it varies depending on the cell temperature. During *open circuit* (oc) condition, no net current is flowing out of the PN-junction. In an illuminated cell under open circuit condition, the number of electrons and holes are increasing in the n-

and p-region respectively. This result in a field in the opposite direction compared to the built-in field, thus reducing the net field inside the cell. This allows a larger current flow through the Space Charge Region, called *saturation current*, which increase the recombination inside the cell. The Saturation current will increase until it balances out the light generated current causing no net current out of the solar cell. The corresponding voltage across the cell in this state is called the *open circuit voltage*, V_{oc}.

The current produced by the solar cell is a result of photons exciting electrons in a semiconductor material, and therefore, it varies with the solar irradiation. In an illuminated cell under *short circuit* (sc) condition, there is no voltage across the cell, and it is the largest possible current produced by the cell. The short circuit current is a function of cell area, light intensity, solar spectrum, absorption, reflection, and properties of the material such as minority carrier lifetime and band gap.

The power is the product of these parameters, and its peak is called the *maximum power point* (mpp) depicted on the IV curve in Figure 2.8. The IV curve is the characteristics of a cell for a given temperature and level of irradiance, and it illustrates how the current change from short-circuit current to open-circuit voltage.

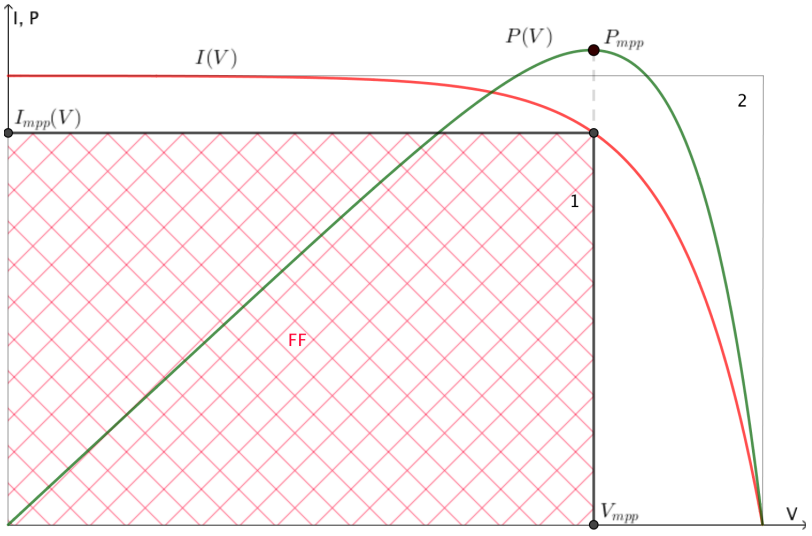

Figure 2.8: *A sketch of the IV curve (red) and the power curve (green) with the maximum power point indicated. The area underneath the mpp (area 1) divided by area 2 is the Fill factor.*

In the same figure, it is indicated FF which is the abbreviation for *Fill factor*. Fill factor is a measure of how well the maximum power point rectangle (the rectangle indicated by 1 in the

IV curve) fits the theoretical power of rectangle 2. It is calculated by

$$FF = \frac{I_{mpp}V_{mpp}}{I_{sc}V_{oc}}, \tag{2.10}$$

where I_{mpp} and V_{mpp} are the mpp current and voltage respectively.

The efficiency of the cell is a measure of how much of the energy of light is converted to electrical energy. This can be calculated by

$$\eta = \frac{FFI_{sc}V_{oc}}{I_{POA}}, \tag{2.11}$$

where G_{POA} is the POA irradiance.

2.2.3.2 The diode model

The equivalent circuit for a solar cell is called the diode model. A commonly used model for a PV cell is called the *two diode model*, and the equivalent circuit is illustrated in Figure 2.9. This model describes the behaviour of a solar cell by the equation

$$I = -I_{ph} + I_{d,1}[\exp(\frac{V - IR_s}{n_1 k_B T_{cell}}) - 1] + I_{d,2}[\exp(\frac{V - IR_s}{n_2 k_B T_{cell}}) - 1] + \frac{V - IR_s}{R_p}, \tag{2.12}$$

where I and V are the current and voltage of the PV cell. I_{ph} is the photogenerated current, while $I_{d,1}$, $I_{d,2}$, and I_p are the currents through diode one, diode two, and the parallel resistor respectively. R_s is the series resistance that is connected to the resistance in the current collectors, and R_p is the parallel resistance which denotes the losses due to shunts in the material. n_1

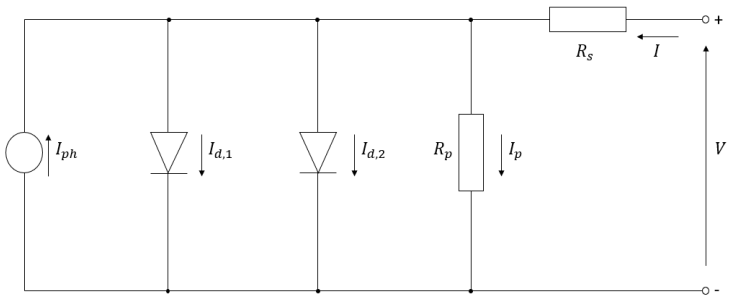

Figure 2.9: *A circuit diagram of the equivalent circuit describing the behaviour of a solar cell based on the two diode model. I_{ph} is the photo generated current from the cell, $I_{d,1}$ is the current through diode one, $I_{d,2}$ is the current through diode two, R_s is the series resistance, R_p is the parallel resistance, I is the current through the cell and V is the voltage over the cell.*

and n_2 is the ideality factor of diode one and two. Diode one is an ideal diode with an ideality factor of 1 which assume band to band recombination or via traps in the bulk material only. Diode two is a non-ideal diode representing recombination in the SCR. T_{cell} and k_B is the cell temperature and Stefan-Boltzmann constant respectively.

2.2.4 PV cell loss mechanism

There are multiple loss mechanisms connected to a PV cell, and some of them are briefly described in this section.

2.2.4.1 Spectral mismatch

The most important loss factor is *spectral mismatch*. Spectral mismatch is the loss connected to photons with energy different from the band gap energy. Firstly, all photons with energy lower than the band gap are lost solely because the electron cannot be excited into the conduction band. Secondly, if the photon energy is larger compared to the band gap energy, the difference between the band gap energy and the photon energy is lost due to *Thermalisation*. Thermalisation is the loss related to electrons being excited to energy levels above the band gap. However, as the lower energy levels in the conduction band are not full, the electron quickly releases the energy in form of heat.

2.2.4.2 Temperature losses

A side effect of losing the photon energy to Thermalisation is that heat is generated. This heat increase the cell temperature which again cause losses in the conversion of solar energy into electrical energy. When the cell temperature increase, the band gap decrease is causing a small increase of short circuit current since more photons are now able to excite electrons into the conduction band. The voltage, however, is reduced by a larger proportion eliminating the positive effect of an increased current resulting in a net loss.

2.2.4.3 Optical losses

The last loss mechanism that will be described is loss connected to reflection. Reflection is connected to material properties, angle of incidence and wavelength by Snell's law. If the angle between the incoming wave and the surface normal vector is small, typically up to 50°,

the total reflection is usually small for solar cells. This is a result of different measures taken by the cell manufacturer such as adding an *anti-reflection coating* and making the cell surface textured. However, at angles larger than 50°, the reflection starts to increase[29].

2.3 The PV system

2.3.1 The PV module

One single PV cell does not produce the voltage, current, and power on the needed scale for most applications. To solve this problem, many PV cells are connected in a series to increase the output voltage. The net voltage of the series is the sum of the cell voltages in the series, while the current is determined by the cell which produce the lowest current. It is therefore important to match the cells used in each module to prevent *mismatch loss*.

Bypass diodes are also often used to prevent generation of *hot spots* by providing an alternative path for the current. A hot spot is an area in the module that generates heat due to reverse biasing the shaded cell.

PV modules can also be connected in series, called a *string*. This will increase the output voltage of the string, while the current is decided by the module that has the lowest output current. The current can be increased by connecting multiple strings in parallel, and the voltage is determined by the string with the lowest voltage output. Finally, the power is also increased according to the equation

$$P = VI, \tag{2.13}$$

where V is the voltage, and I is the current.

2.3.2 Converters and inverters

Since the voltage provided by a PV module is varying with the incoming irradiation and cell temperature, and that electrical applications need a voltage at a certain range, a *DC/DC converter* is used to convert the voltage to the level of interest. This can be done by the *Buck-Boost converter* that use switches, inductors, and capacitors to convert the voltage up and down depending on the switching pattern.

As PV modules generate DC signal, an *inverter* is used to transform it into AC signal. For

grid-connected systems, the inverter also has to *synchronise* the AC signal with the grid (i.e. having the same phase as the grid). One example of a DC/AC inverter is the *full bridge inverter* which use four switches working in pairs.

There are numerous different inverter technologies, and two examples are the *string inverter* and the *micro inverter*. A micro-inverter is normally used in small systems, while a string inverter is normally used in larger systems.

2.3.2.1 Maximum power point tracker

As mentioned before, the PV module's current and voltage output will vary depending on solar irradiation and cell temperature. Consequently, the mpp of the PV module will co-vary, and the module will operate in a sub-optimal state. This problem is solved by a *maximum power point tracker* (mppt) that optimises the operation of the system. The mppt is normally included in the inverter.

There are different kinds of algorithms used in mppts, and one is called *Perturb and observe*. This algorithm simply perturbs the operation voltage of the cell and observes what the effect is on the power output. If the power increase, the voltage will be set as the new operation voltage and a new perturbation will be executed. This will result in an operation point close to the maximum power point, but it will not be constantly located at the mpp due to its constant process of perturbation. Another disadvantage is that it struggles to follow rapidly changing irradiation because the direction of perturbation is decided by the direction of last change in voltage. That means if the last voltage change resulted in an increase in power, it will further increase the voltage. Consequently, if the irradiation is reduced since the last voltage increase, it will take time before the algorithm realise that the voltage was altered in the wrong direction. Thus, if the irradiation rapidly changes from low to high and back again, the operation condition of the module will constantly be sub-optimal.

2.3.2.2 Inverter efficiency

The inverter efficiency is a measure of how well it inverts the DC current to AC current, and it is defined as

$$\eta = \frac{P_{AC}}{P_{DC}}, \tag{2.14}$$

where P_{Ac} is the output power and P_{DC} is the input power. The efficiency will vary dependent on both voltage and power input.

Another way of expressing the efficiency of an inverter is the *weighted efficiency*. This metric takes the output power into account to provide a more accurate efficiency simulating real conditions. *European efficiency* (EU) and *California energy commission efficiency* (CEC) are two examples of weighted efficiencies.

2.3.3 System loss mechanisms

One of the loss mechanisms connected to obstruction of light from reaching the module is called *shadowing*. Shadowing affects the current produced because it prevents photons from reaching the module. If one module in a string is shaded, the loss is especially large since the output current in the string is reduced. As a result, all modules will operate under sub-optimal conditions. Micro inverters might attenuate this loss because every module can be constantly operated in an optimal state. Another loss mechanism connected to obstruction of light is *Soiling*, dust and dirt preventing light from being absorbed by the semiconductor material.

A second loss mechanism is called *Module mismatch* which is losses caused by different characteristics of modules in a string. This is caused by the fact that optimal operation conditions vary between cells, and it is therefore important to use as equal cells as possible in a string.

The inverter is, like every other electronic device, not 100% efficient. The losses are caused by for example switches that need to be controlled, electrical resistance in the cables, and power needed to operate the device.

2.3.4 System evaluation parameters

To evaluate the system performance, *yield*, *specific yield*, *performance ratio*, and *temperature corrected performance ratio* are used in this thesis.

Yield is defined as

$$Y = \Sigma_{i=1}^{t} E_i, \tag{2.15}$$

where E_i is the energy produced by the system in a specific time period i, and t is the total number of time periods.

Specific yield is defined as

$$y = \frac{Y}{P_{rated}}, \tag{2.16}$$

where P_{rated} is the rated power of the system.

The performance ratio is a metric of a PV system's quality, and it is defined as

$$PR = \frac{\Sigma_i^n P_i / P_{rated}}{\Sigma_i^n G_i / G_{STC}}, \tag{2.17}$$

where P_i is the power produced at time i, G_i is the irradiance at time i, and G_{STD} is the irradiance under standard test conditions (STD). Temperature corrected performance ratio was later defined by T. Dierauf et al.[30] as

$$PR_{corr} = \frac{\Sigma_i^n P_i / P_{rated}}{\Sigma_i^n (G_i / G_{STC})(1 + \gamma[T_{cell,i} - T_{STC}])}, \tag{2.18}$$

where γ is the temperature coefficient of the PV module, $T_{cell,i}$ is the inner temperature of the cell (also called cell temperature) at time i, and T_{STC} is the temperature under STC. This metric was developed to achieve a better comparison of PV systems in different climates.

As the cell temperature is rarely known, an estimation method is needed. D.L. King et al. at Sandia National Laboratories developed a model for estimating the cell temperature by first estimating back surface temperature before this is used to estimate the cell temperature[31]. The back surface temperature can be estimated by the equation

$$T_{bs} = G_{tot} \exp(a_2 + b_2 v) + T_A, \tag{2.19}$$

where T_{bs} is the module's back surface temperature, G_{tot} is the total POA irradiance, a_2 is an upper limit for the module temperature under low wind and high irradiance conditions, b_2 is the rate of change of back surface temperature dependent on the wind speed, v is the wind speed, and T_A is the ambient temperature. a_2 and b_2 is empirical determined coefficients and are dependent on system type.

The estimated cell temperature is estimated by

$$T_{cell} = T_{bs} + \frac{I_{tot}}{I_{STC}} \Delta T, \tag{2.20}$$

where ΔT is the temperature difference between T_{bs} and T_{cell} under G_{STC}.

2.3.4.1 Standard test conditions

Standard test conditions where developed to provide a standard for testing PV modules enabling comparison of different panels. The STC irradiance and the cell temperature is defined as $G_{STC} = 1000\ \frac{\mathrm{W}}{\mathrm{m}^2}$ (AM1.5) and $T_{STC} = 25°\mathrm{C}$ respectively.

3 Method

This chapter provides a description of the meteorological stations, the PV systems, the inverter test, and the method used for data analysis.

3.1 Meteorological data

3.1.1 Locations

The meteorological data used was collected from The Norwegian Meteorological Institute historical weather database[32] using their Frost API. A Python program was programmed to do this automatically. The weather stations are located at Apelsvoll, Ilseng, and Gausdal which is in the proximity of the PV systems analysed in this thesis. These stations measure hourly mean GHI data and hourly mean temperature from two meters above ground level. The pyranometer in Apelsvoll is Kipp & Zonen CMP11[33] with an uncertainty of <2% for daily GHI measurements [34]. The locations of the meteorological stations are shown in Figure 3.1 indicated with red markers. The weather stations provide time series that expands many years. However, only the period from January 2018, to March 2019, is used. Information regarding station number, location, and time zone used is given in Table 3.1.

Table 3.1: *Information of the meteorological systems' location and data.*

Station number	Station name	Latitude	Longitude	Data range	Time zone
11500	Apelsvoll	60.7002	10.8695	01.01.2018 - 31.03.2019	UTC
12180	Ilseng	60.8028	11.2028	01.01.2018 - 31.03.2019	UTC
13030	Gausdal	61.2247	10.2588	01.01.2018 - 31.03.2019	UTC

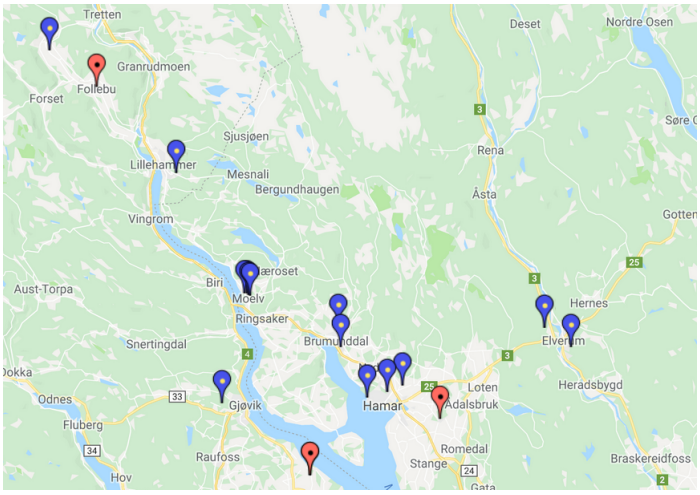

Figure 3.1: *The locations of the meteorological stations used and the PV systems analysed in this thesis. The blue and the red markers indicate PV systems and meteorological stations respectively.*

3.1.2 Data collection

The data is collected from 01.01.2018 00:00:00 to 31.03.2019 00:00:00 and every data point has a date stamp using UTC as time zone. All data from Apelsvoll, Ilseng, and Gausdal was used except from a period from 12.11.2018 to 31.03.2019 collected by Ilseng weather station. In this period, the measured values were unreasonably high and irregular, as seen in Figure 3.2. To further evaluate the Ilseng irradiance data, the hourly production and estimated POA irradiance for 13.11.2018 are plotted in Figure 3.3. As illustrated in the plots, the irradiation measured in Ilseng is unreasonable high during night and day. This caused the result to be useless in comparison with the results from the other stations. Therefore, the meteorological station in Ilseng was not further used in the analysis.

There are, however, some models that estimate the POA irradiance to be zero where others have a non-zero estimate, as seen in Figure 3.3. The reason behind this might be that the Air Mass in the Perez model is affecting the result during night time. However, this was not further studied.

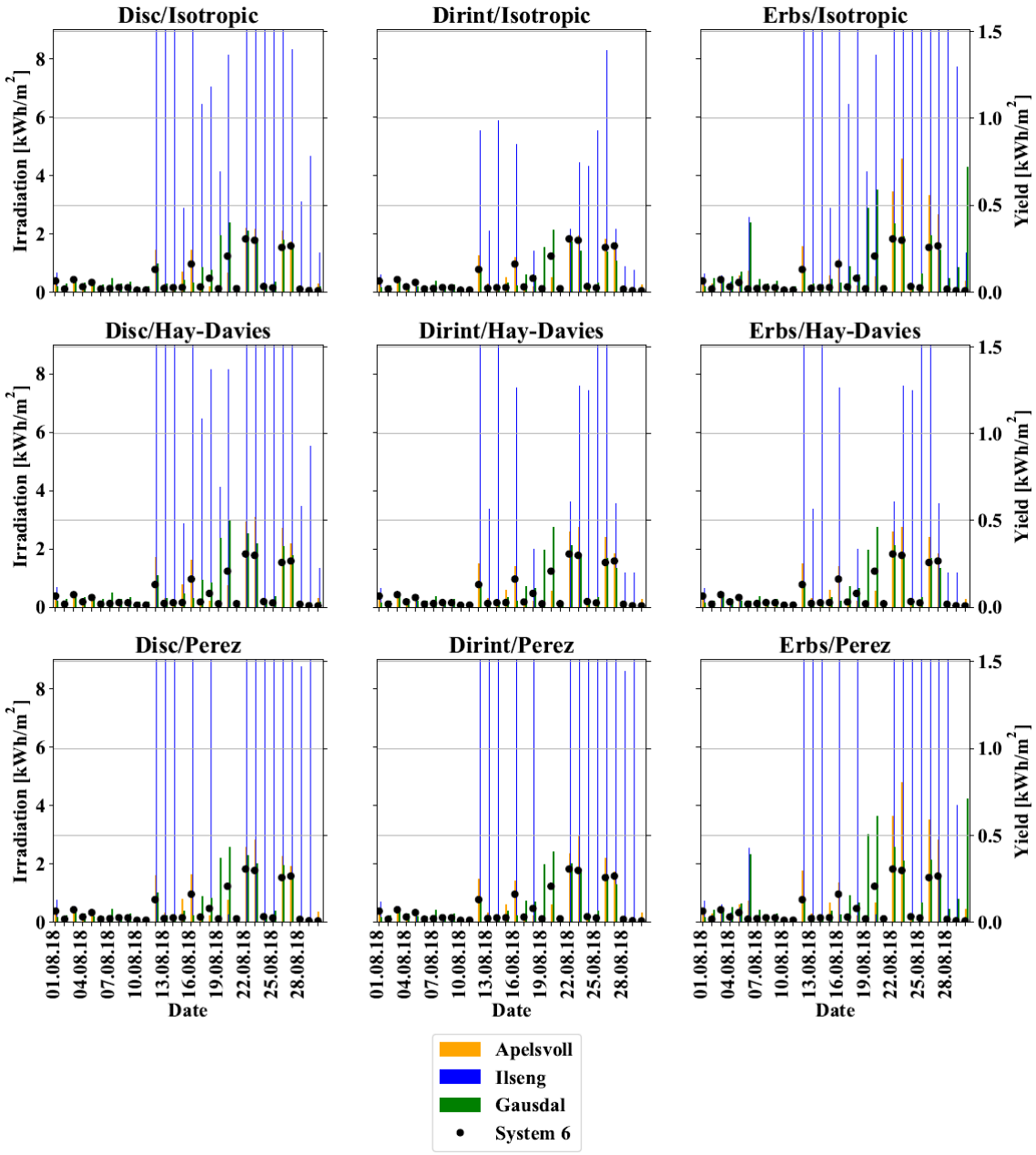

Figure 3.2: *The figures show nine different model combinations for system 6. Along the first axis is every day in November. The estimated POA irradiation per square meter (yellow, blue, and green bars corresponding to Apelsvoll, Ilseng, and Gausdal meteorological station) is along the second axis, while the yield per square meter (black dot) along the third axis. The third axis is scaled by the max efficiency of the PV module to enable comparisons.*

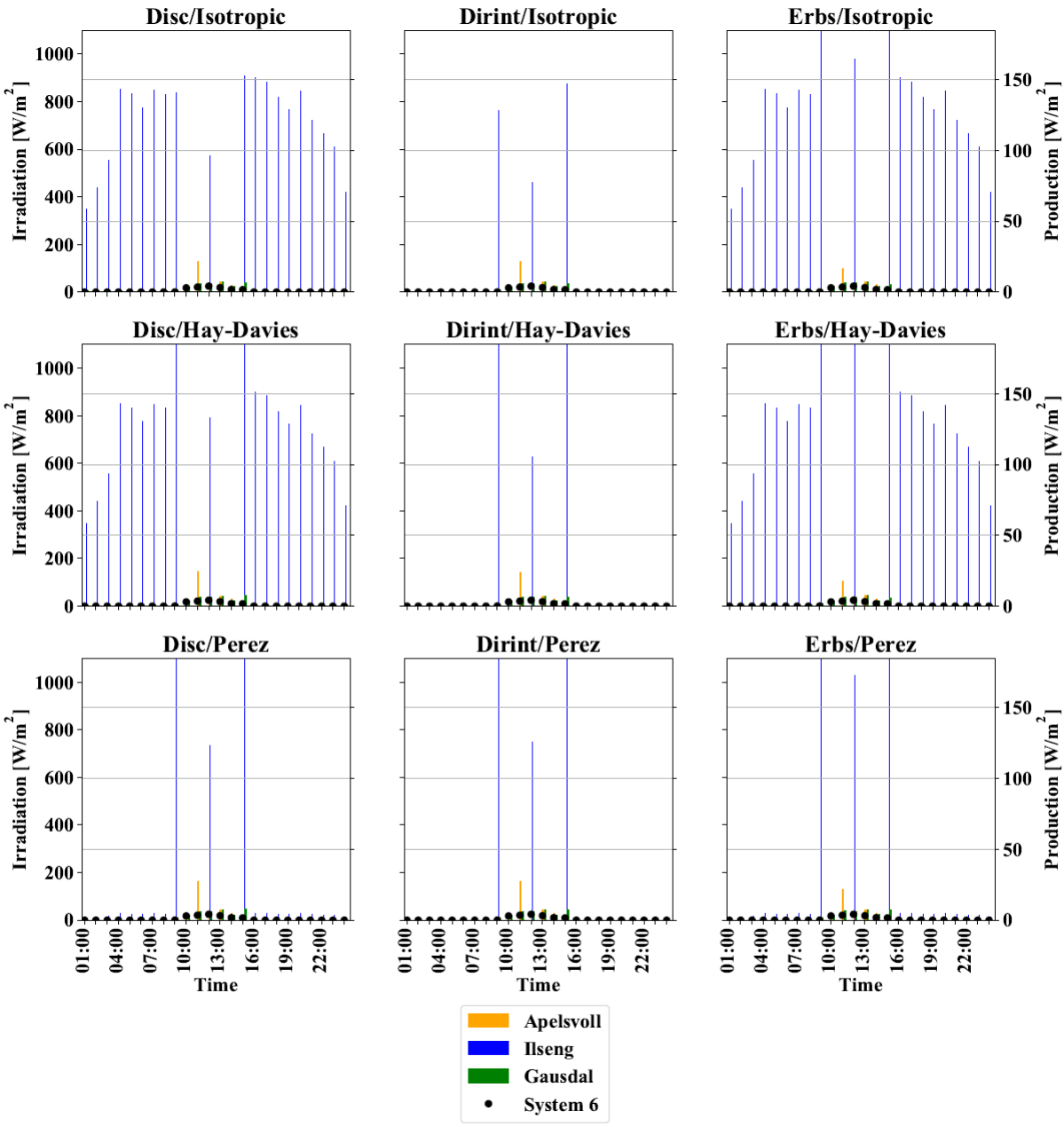

Figure 3.3: *Plots of nine different model combinations for system 6. Along the first axis is every hour of 13.11.18. The estimated POA irradiance (not irradiation as stated in the plots) per square meter (yellow, blue, and green bars corresponding to Apelsvoll, Ilseng, and Gausdal meteorological station) is along the second axis, while the yield per square meter (black dot) along the third axis. The third axis is scaled by the max efficiency of the PV module to enable comparisons.*

3.2 PV systems

3.2.1 Locations

In this thesis, 13 different PV systems were studied. They are located in Oppland or Hedemark county in the southeastern part of Norway, and all of them are indicated in Figure 3.1 with blue markers. All systems are installed on inclined rooftops by Sivilingeniør Carl Christian Strømberg AS, and the installed capacities range from 3.0 kW_p to 6.36 kW_p.

The orientation of the systems range from 130° to 250° where 0° is north as defined in section 2.1.3, whereas the tilt of the systems range from 25° to 50°. All available system characteristics are found in Table 3.2.

3.2.2 Characteristics

The module used in the systems studied is IBC SOLAR's IBC PolySol 265 CS4, and the module characteristics is found in Table 3.3.

Table 3.3: *A summary of the PV module characteristics found in the data sheet[35]. $P_{max,STC}$ is the maximum power under STC conditions, A is the module area, η is the STC efficiency, and γ is the temperature coefficient of P_{mpp} of the module.*

Name	$P_{max,STC}$ [W]	A [m^2]	η [%]	V_{oc} [V]	γ [%/°C]
IBC Solar PolySol 265 CS4	265	1.62689	16.2	38.6	-0.423

All systems contain one of, or a combination of, three inverters: coolcept StecaGrid 3010, Fronius Galvio Light 3.0-1, and Fronius Primo 3.6-1. A summary of the inverter characteristics is found in Table 3.4. Note that the mppt voltage range is the voltage range the inverter is designed for. Outside this range, there are either no production or the mppt does not work properly. The mppt algorithm used in the inverters are not published, but most inverters on the market use a version of the perturb and observe algorithm outlined in section 2.3.2.1.

All PV systems studied in this thesis are installed by using mounting systems from IBC Solar. This system results in an air gap of approximately five cm between the PV module and the roof to enable air flow to cool the modules.

Table 3.2: *A summary of the PV system characteristics. The orientation, Ψ_o, and the tilt, θ_t, is according to the definitions made in section 2.1.3 while distance is the distance to the closest weather station measured in kilometres.*

System	Latt.	Long.	Ψ_o [°]	θ_t [°]	P_{rated} [kW]	number of modules	inverter	Distance [km]
1	60.87169	11.58451	239	29	3.18	12	StecaGrid 3010	43.4 (Apelsvoll)
2	60.89740	11.51449	172	38	3.18	12	StecaGrid 3010	41.5 (Apelsvoll)
3	60.18867	11.98596	203	46	3.18	12	StecaGrid 3010	83.9 (Apelsvoll)
4	60.81098	11.08373	221	26	3.18	12	StecaGrid 3010	17.0 (Apelsvoll)
5	61.26543	10.15562	211	24	3.18	12	StecaGrid 3010	9.2 (Gaustad)
6	60.87125	10.95718	158	40	3.18	12	StecaGrid 3010	19.6 (Apelsvoll)
7	61.10268	10.50674	216	35	5.30	20	2x StecaGrid 3010	18.3 (Gaustad)
8	60.79731	10.62853	192	38	3.18	12	Fronius Galvo Light 2.5-1, Fronius Primo 3.6-1	18.6 (Apelsvoll)
9	60.93983	10.70643	205	38	6.36	24	StecaGrid 3010	29.6 (Apelsvoll)
11	60.94095	10.70320	131	33	3.18	12	StecaGrid 3010	29.6 (Apelsvoll)
12	60.89823	10.94661	208	29	3.18	12	StecaGrid 3010	22.4 (Apelsvoll)
14	60.80366	11.02740	153	46	4.24	16	StecaGrid 4200	14.4 (Apelsvoll)
15	60.94215	10.69252	227	28	3.18	12	StecaGrid 3010	29.6 (Apelsvoll)

Table 3.4: *A summary of the the inverter characteristics found in the product data sheets.*

Name	$P_{AC,rated}$ [W]	η_{max} [%]	$V_{DC,max}$ [V]	$V_{mppt\ range}$ [V]
StecaGrid 3010 [36]	3000	98.6	600	[125,500]
StecaGrid 4200 [36]	4200	98.6	845	[350,700]
Fronius Galvio Light 2.5-1 [37]	2500	96.1	550	[165,440]
Fronius Primo 3.6-1 [38]	3600	98.0	1000	[200,800]

3.2.2.1 Shadowing

To study the reason behind the result of specific yield and temperature corrected performance ratio, shadow detection is necessary.

The algorithm developed by M. J. Reno and C. W. Hansen (section 2.1.4.5) was used to detect the clear sky days in the irradiance data set. Due to failure of detecting any clear days by using default settings, the criteria were altered to the values shown in Table 3.5.

Table 3.5: *An overview of the parameters used in the clear day detection algorithm.*

α_1	α_2	α_3	α_4	α_5	α_6	α_7	α_8
150	150	10	20	0.5	8	10 hours	20

The hourly production and the hourly estimated POA irradiation for the detected clear days are plotted to assess if shadows are a significant source of system loss. A shadow is detected if the rate of change of irradiance and the rate of change of production is dissimilar or the production is suddenly reduced. Clear sky days were used because clouds also can be a source of a production reduction.

A trip to the systems was also arranged to look for sources of shadows near the system.

System 1

The system has a house located in the front for the system which may cause shadow losses. However, the production plots of clear days did not provide any evidence of any shadow losses.

System 2

The system has a large house located east for the system. This house is tall which may cause shadow losses during the morning. Additionally, there is a small forest located south and southwest for the system that may cause shadow losses.

By looking at the production data (Figure 3.4), the production barely increases from 7 to 8 o'clock in 14.04.18 in Figure (a day defined as clear by the algorithm). This does however not happen during summer when the Sun's elevation is larger, as Figure 3.4b shows. This is also true for 12.04.18 and 13.04.18. Thus, this may indicate a shadow from the house causing losses.

There are no signs of losses connected to the mentioned forest.

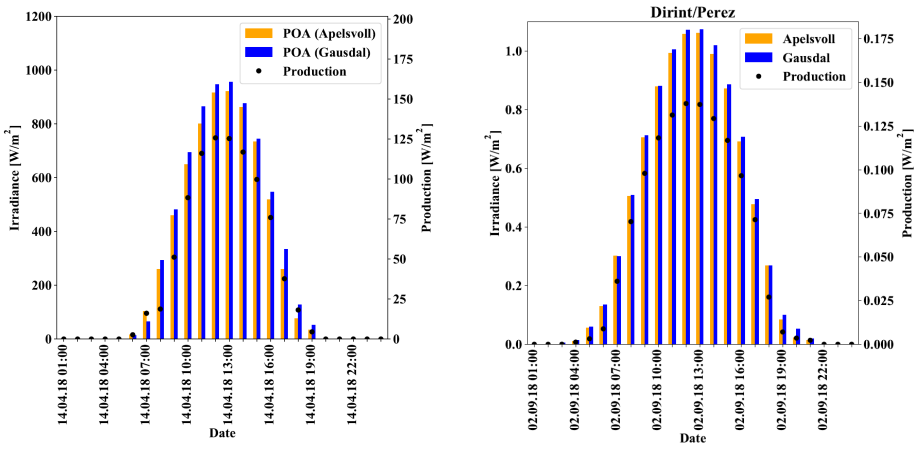

(a) *14.04.2018* (b) *30.06.2018*

Figure 3.4: *Plots of hourly plots from three different days. Figure 3.4a shows a slowly increasing curve at the beginning of the day that might indicate morning shadow. Figure 3.4b depicts a clear day without any sign of shadowing during the day.*

System 3

System three was not visited, and the clear day production plots did not provide any evidence of any shadows losses. Hence, it is not possible to detect any shadows losses.

System 4

There is a large tree located south and a house located west for the system that may cause shadow losses. The clear day production plots did, however, not provide any evidence for any shadow losses.

System 5

There are no nearby objects that can cause any shadow losses, but as the system is located in a valley, there is a mountain that may cause a shadow in the morning and evening. Clear day production plots did not provide any evidence of shadow losses, which may be explained by the weather station being located in the same valley.

System 6

There is no nearby object that can cause any shadow losses as the system is located at a higher altitude compared to the houses in front of the systems. The clear day plot did not provide evidence for any shadow losses either.

System 7

This system has two strings installed on each side of a dormer that will cause a shadow on each string dependent on the time of the day. Additionally, there are trees located to the west that may cause losses when the elevation of the Sun is low.

The clear day production plots of each string (Figure 3.5) show that the production of string 2 is above the production of string 1 in the last couple hours of the day, while the production is similar the rest of the day. This is true for clear days in general (see Appendix B for more plots of the system 7 data). which may be an indication of shadow losses. Although there should be a shadow on string 2 during the morning, there is no evidence confirming that.

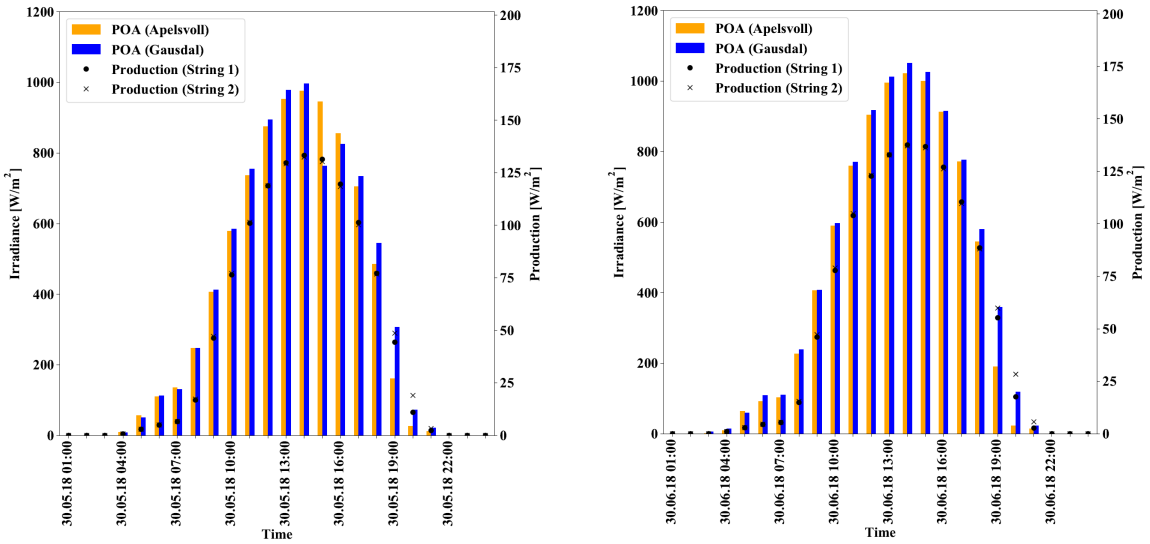

(a) *30.05.2018* (b) *30.06.2018*

Figure 3.5: *Plots with hourly resolution from three different days. Both plots shows that string 2 has a larger production compared to string 1, which may be explained by a shadow from the dormer in between the strings.*

System 8

The system is installed on the east side of a dormer on the roof which causes a shadow during the evening. There is also a large tree in front of the house that may cause losses. The clear day plots do not give any evidence of any shadow losses.

System 9

System 9 also has a dormer separating the two strings that may cause shadow losses. As the data set is small, it is not clear whether it is losses connected to the dormer's shadow, or not. However, two relatively clear days is shown in Figure 3.6. The figure illustrates that string 1 is producing more during morning hours, less during night hours, and relatively similar in the middle of the day compared to string 2.

System 11

A couple of trees are located east for the system that may cause losses during the morning. The clear day plots did not show any evidence for losses connected to shadows from these trees.

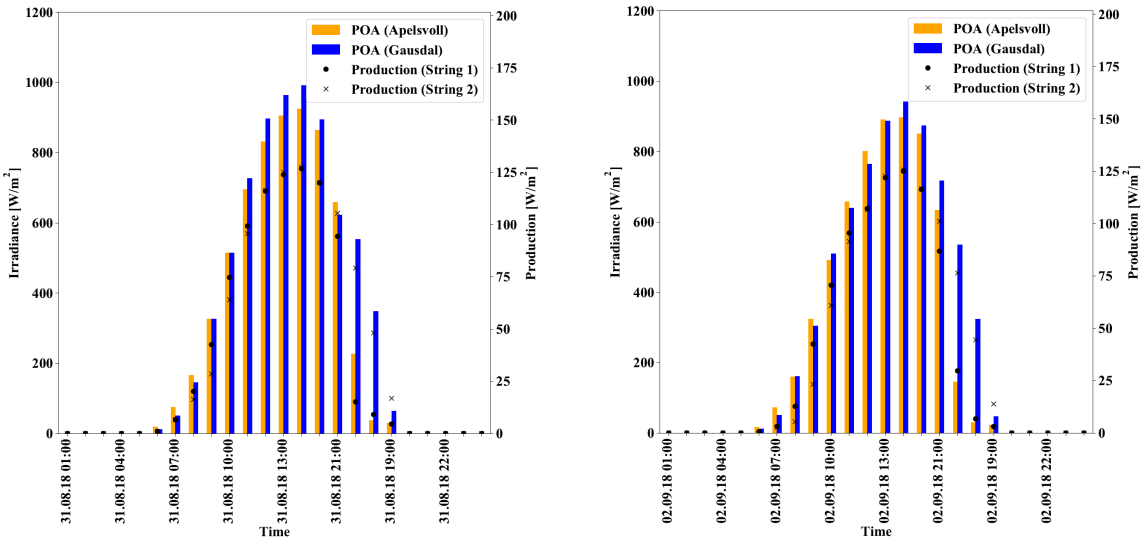

(a) *31.08.2018* (b) *02.09.2018*

Figure 3.6: *Plots of hourly data from two different days. Both plots shows that string 1 produce more during the morning, and less during the night compared to string 2, while the mid day production is relative equal. This may be explained by a shadow from the dormer in between the strings.*

System 12

The system was not visited, and the clear day plots did not show any evidence for shadow losses due to the data set's size. Hence, it is not possible to detect any losses connected to

System 14

A large house is located right in front of the system which might cause losses during the day in the spring and autumn. However, there are no indications of shadow losses in the clear day production plots.

System 15

There are no object that can cause any shadow losses, and the clear day production plots did not provide any evidence for shadow losses either.

3.2.2.2 Thermal imaging

Thermal images of the systems were taken to check if the modules have any damages causing losses. The images were taken by Testo 872 from ground level. A thermal imaging camera

work similarly to a normal camera as it uses sensors to detect electromagnetic waves, turn them into electrical signals, and correlate the signals to colours. It differs from a normal camera of which electromagnetic waves it detects. Where a normal photo camera detects photons with wavelengths in the visible range, the thermal camera detects photons in the infrared range. The different colours on the image correlates to different temperatures of the objects.

The result depicts most likely no damages on any module in any of the PV systems. An example is shown in Figure 3.7, while the rest is shown in appendix C. Note that the absolute temperatures shown in the images are wrong. This is because there was not possible to set the correct emissivity and temperature reference for the systems.

However, the pictures show a constant temperature over the PV modules, while the roof has another constant colour indicating a temperature difference. Thus, if there were any hot spots in the PV modules, there should be an area on the modules with a different colour compared to the rest of the modules.

The colours of the objects are not only due to temperature but also reflection. An example of this is shown in Figure 3.8, where a reflection of the chimney is visible on the panels. Even though reflection is a part of the images, the temperature differences should be visible. Thermal images were taken from different angles to remove uncertainty connected to reflection.

Note that system 3 and 12 were not visited, and system 7 was impossible to get good images of.

3.2.3 Data collection

The data from the PV systems is collected from the inverter and stored by using Solar-log. DC- and AC voltage, DC- and AC power, and cumulative energy in 5-minute intervals were logged. If the system has multiple strings, the DC voltage and DC Power are given for each string. The uncertainty connected to these readings is not known. However, a study has shown that a badly monitored system has between 4% and 6% uncertainty on the calculation of PR[39].

The data is stored online as java-files. This had to be downloaded through FTP servers and turned into a usable format for Python. This was done by loading the data as text files before iterating through every line of information. Each number is converted from a string to a float with appropriate separators in between.

Before analysing the data, it was transformed into one-hour intervals to correspond to the

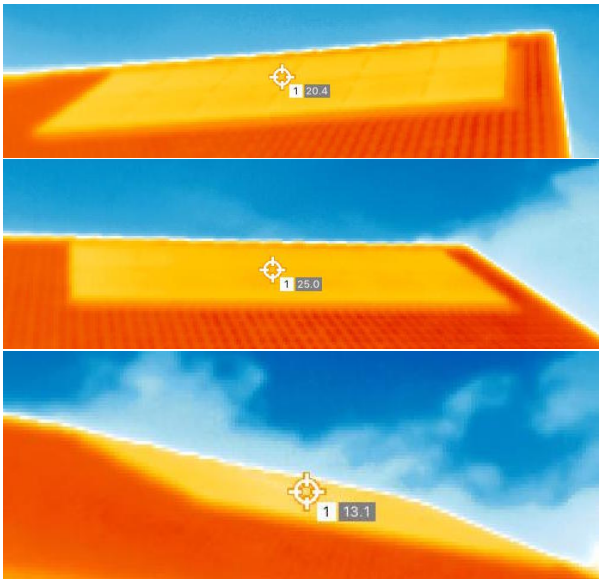

Figure 3.7: *Three thermal images of system 11 taken from different angles. These images indicate a constant temperature over the entire system. Note that the absolute temperatures shown in the images are wrong as temperature and emissivity references were not possible to set.*

Figure 3.8: *Two thermal images of system 15, taken from different angles, indicating a constant temperature over the entire system. The images of the system from different angles show that the darker area is due to the pipe. Note that the absolute temperatures shown in the images are wrong as temperature and emissivity references were not possible to set.*

weather data. In this thesis, one hour is defined as the time period from XX:05 to YY:00, for example, the data collected between 01.01.2018 11:05:00 and 01.01.2018 12:00:00 is defined as 01.01.2018 12:00:00. The hourly yield is calculated by subtracting the yield at XX:00 by (XX-1):05 since the data is stored as a sum until XX:00. The hourly voltage and power were calculated by taking the mean of every data point from XX:05 to (XX+1):00.

The data range from every system varies due to different installation dates, and the respective data ranges are found in Table 3.6.

Table 3.6: *The different periods where data are collected for the systems, including time zone used.*

System	Data range	Time zone
1	05.08.17 - 31.03.19	
2	05.04.18 - 31.03.19	
3	19.08.18 - 31.03.19	
4	26.05.18 - 31.03.19	
5	18.02.18 - 31.03.19	
6	01.01.18 - 31.03.19	
7	25.03.18 - 31.03.19	
8	26.05.18 - 31.03.19	GMT+1/CEST
9	22.08.18 - 31.03.19	GMT+1/CEST
11	26.05.18 - 31.03.19	GMT+1/CEST
12	10.08.18 - 31.03.19	GMT+1/CEST
14	07.08.18 - 31.03.19	GMT+1/CEST
15	28.06.18 - 31.03.19	GMT+1/CEST

The blank spaces in Table 3.6 indicates that the time zones used to log data, and whether daylight saving time is used or not, is unknown. This problem was solved by using the meteorological data as a reference to adjust the data to the UTC time zone. It turned out that all systems had the GMT+1 time zone including the use of daylight saving time.

To prevent mistakes in the data caused by, for example, the pyranometer's offset and uncertainty, irradiance and production were set to zero when the sun is below the horizon. Therefore, the solar position algorithm was used to calculate the solar elevation for every hour. For every hour with negative elevation, meaning the Sun is below the horizon, the PV system data was set to zero. Additionally, all negative irradiance data was set to zero, as it is not possible to have negative irradiance.

3.2.4 Modelling

In this thesis, the Python package *PVlib*[40] was used to analyse the data. The package contains different classes and functions that are used for simulating PV systems. It was originally de-

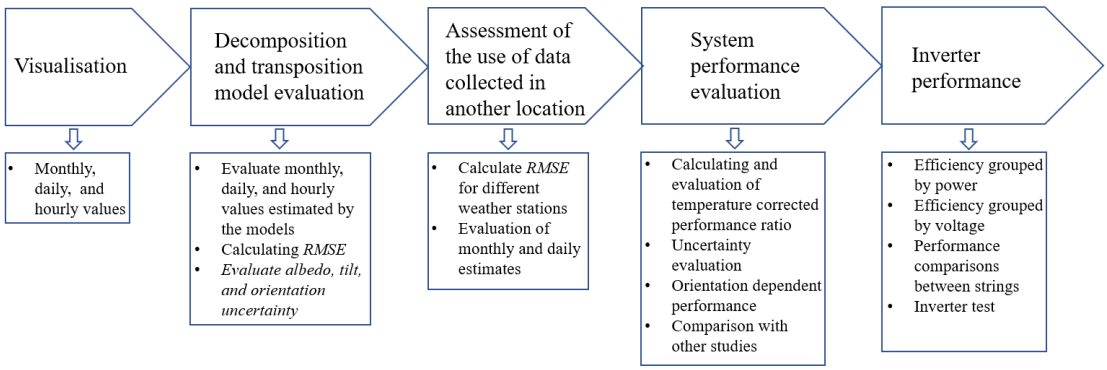

Figure 3.9: *A visualisation of the data processing and analysis followed in this thesis.*

veloped by Sandia Laboratories for MATLAB and later extended to Python. The theory behind the functions used in this thesis is explained in section 2.1.4.

3.3 Analysis methods

The analysis process is illustrated in Figure 3.9. The performance analysis starts with a general visualisation to get an overview of irradiance data and PV system data. The reason is to assess the quality of the data, remove data that is wrong, and to find periods where the system is out of service. The second step is to analyse the decomposition and transposition model combinations to verify which model combination that performs best in Norwegian climate. This is necessary because none of the meteorological stations measure the POA irradiance, nor does the the household systems. The next step is to assess if irradiance measurements from another location than the PV system can be used to analyse the PV system performance. This step is needed to ensure the quality of the analysis as very few household systems have irradiance measurements. The fourth step is to analyse the total system performance before the performance of the inverter is evaluated.

3.3.1 Modelling and visualisation

The first step in analysing the data was to choose a set of decomposition and transposition models to estimate the POA irradiance. Based on the available models in the Python library PVlib, complexity, and performance, the models listed below were chosen.

Decomposition models:	Transposition models:
• Erbs' model	• Isotropic model
• DISC model	• Hay-Davies model
• Dirint model	• Perez model

The second step was to visualise the estimated irradiance data together with production data to detect mistakes and to confirm that the nine model combinations have a similar shape as the production data in hourly, daily and monthly time resolution. To do this, different input data had to be given to estimate the POA irradiance. For every decomposition model (i.e. the conversion from GHI to DNI and DHI) the solar zenith and the date were needed as input. The solar zenith was calculated by using the method briefly described in section 2.1.4.1 with date and position as input. This resulted in either DNI or DHI depending on which model that was used, and eq. (2.5) was used to calculate the last component. Also, as the dew point temperature of the system locations is unknown, it was not used in the Dirint model.

For the transposition models (i.e. the shifting from horizontal irradiance to POA irradiance) the input is GHI, DNI, and DHI together with system tilt, orientation, solar zenith, and solar azimuth angle (also found by the solar position algorithm). Henceforth, the models differ by the inputs EDNI, AM, albedo, and surface type. EDNI is needed to calculate the effective Global horizontal transmittance (see section 2.1.4.2), AM to calculate the attenuation through the atmosphere, and albedo and surface type to calculate reflected irradiance. Most of these parameters were set to default settings when possible, while AM was estimated by using F. Kasten's model discussed in section 2.1.1. The different input parameters used in the different models are found in Table 3.7.

3.3.2 Decomposition and transposition model performance

To verify which decomposition and transposition model that performs best in Norwegian conditions, data from Nibio Apelsvoll's test system was used. The system is oriented 172.8° with a 46° tilt. GHI data was collected from the same location, and the pyranometers have an uncertainty of $\pm 2\%$[34]. The data range from 01.06.2018 to 31.03.2019, and it contains global POA irradiance measurements. The POA irradiance data set is used as a reference for the estimated

Table 3.7: *An overview of the transposition models' input parameters used in the analysis.*

Model	EDNI*	Air mass	Albedo	Surface type
Isontropic	None**	None	0.25++	None
Hay-Davies	1361+	None	0.25	None
Perez	1361	Kasten	0.25	None

* Extraterrestrial DNI

** no input since no data was available

+ the model in which it is required use the mean value

++ standard value for albedo corresponding to something in between grass and concrete

global POA irradiance obtained by the model combinations.

To decide which model to use in the system analysis, the root mean square error (*RMSE*) was calculated. *RMSE* is defined as

$$RMSE = \sqrt{\frac{\Sigma_i^N (G_{i,E} - G_{i,M})^2}{N}}, \tag{3.1}$$

where N is the number of data points, $G_{i,E}$ is the estimated POA irradiance, and $G_{i,M}$ is the measured POA irradiance of time period i. The model with the smallest *RMSE* was chosen as the model to use in the analysis.

Another metric of measuring differences is the *normalised root mean square error* (*NRMSE*) defined as

$$NRMSE = \sqrt{\frac{\Sigma_i^N (G_{i,E} - G_{i,M})^2}{N}} \frac{1}{G_{mean,M}}, \tag{3.2}$$

where $G_{mean,M}$ is the mean measured irradiance of that period.

3.3.3 Assessment of irradiance model performance using data from another location

To study the effect of distance between the location of GHI measurement and the location of interest, GHI data from multiple meteorological stations were studied (see Figure 3.10 and Table 3.8 for a full overview). This data was decomposed and transposed, and compared to the POA irradiance measurement in Apelsvoll by plotting them in the same graph and calculating the *RMSE*.

Table 3.8: *A summary of the meteorological stations' meta data used to analyse the effect of distance.*

Station number	Station name	Latitude	Longitude	Data range	Time zone	Distance [km]
11500	Apelsvoll	60.7002	10.8695	01.06.2018-30.03.2019	UTC	0
20540	Gran	60.3558	10.5592	01.06.2018-30.03.2019	UTC	38
13030	Gausdal	61.2247	10.2588	01.06.2018-30.03.2019	UTC	66
20280	Hønefoss	60.1403	10.2662	01.06.2018-30.03.2019	UTC	68
5660	Roverud	60.2537	12.0913	01.06.2018-30.03.2019	UTC	82
18700	Oslo	59.9423	10.7200	01.06.2018-30.03.2019	UTC	85
13150	Fåvang	61.4582	10.1872	01.06.2018-30.03.2019	UTC	92
19940	Lier	59.7908	10.2598	01.06.2018-30.03.2019	UTC	98
26820	Hokksund	59.7613	9.8922	01.06.2018-30.03.2019	UTC	116
26990	Sande	59.6193	10.2150	01.06.2018-30.03.2019	UTC	134

The meteorological stations used in this assessment is spread over an area in southeastern part of Norway. The specific locations are found in Table 3.8 and Figure 3.10.

Before the analysis, all irradiance data was set to zero in the periods where the POA irradiance measurement equipment was out of service. Additionally, all data was set to zero in periods where snow or ice influenced the measurements. This resulted in a total of 16 days being removed.

3.3.4 PV system performance

After deciding which irradiation model to use, the performance of the different systems was evaluated. First, the total temperature corrected performance ratio (PR_{corr}) was calculated for the period 22.08.18 to 30.03.19. The temperature measurements used were measured by the same weather station as the irradiance measurements, and the period was chosen because all systems are operating from this date. The monthly PR_{corr} was also calculated. The results were studied, and possible loss and uncertainty factors were discussed. Moreover, the PR_{corr} was compared between systems oriented east and west. For example, the systems oriented between 150° and 160° (system 6 and 14) were compared to systems oriented between 200°

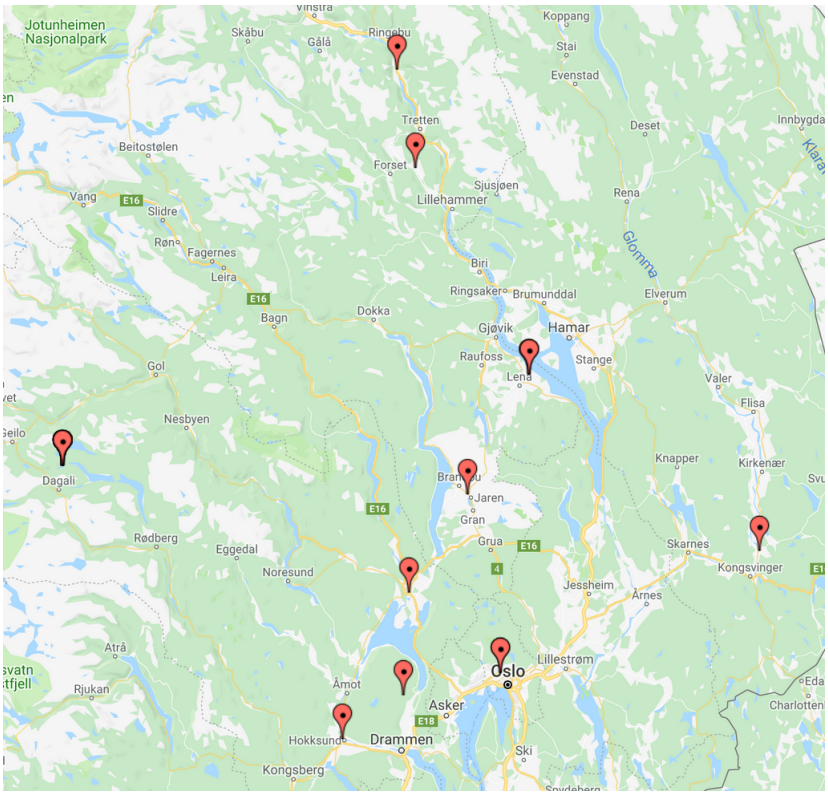

Figure 3.10: *A map of the weather stations used to assess the impact of distance to the decomposition and transposition models.*

and 210° (system 3, 9, and 12) as both groups are 20°-30° away from 180°.

Secondly, the specific yield and performance ratio were calculated and compared with other studies.

3.3.5 Inverter performance

3.3.5.1 Inverter efficiency evaluation

After evaluating the overall system performance, the performance of the different inverters was assessed in two ways. First by grouping the data by 5% intervals of the fraction of rated power ($\frac{P}{P_{rated}}$). For every group, the sum of the AC power was divided by the DC power to calculate the efficiency. This was repeated by grouping by 5% intervals of the fraction of maximum operating voltage ($\frac{V}{V_{max,op}}$). The result was plotted together with the yield.

Additionally, system 7 and 9 (the system configurations are shown in Figure 3.9) were studied to see how different number of modules in each string affect the performance.

Table 3.9: *An overview of the configurations of the systems analysed.*

System	String 1	string 2
7	10	10
9	15	9

3.3.5.2 Inverter test

The system used is located in Fredrikstad, Norway and belongs to Sivilingeniør Carl Christian Strømberg AS. The system orientation is 213° with 20 IBC Solar 265 W PV modules tilted 10°. For assessing the importance of voltage on the system efficiency, the modules are divided into two strings with 15 modules in string 1 and five modules in string 2 with equal orientation and tilt. The number of modules on each string was chosen on the basis on the inverter's mppt voltage range (120-550 V). String 2 has five modules corresponding to 158.5 V, while string 1 has 15 modules corresponding to 475.5 V under mpp conditions. The inverter used is MG4K6TL-2M, and total yield, total AC- power, DC-power for each string, and voltage for each string were logged during the period 03.05.19 to 08.05.19.

3.3.5.3 Analysis method

As the data did not contain AC power for the individual strings, specific yield was used to evaluate the string performance.

4 Results and Discussion

4.1 Decomposition and transposition model evaluation

4.1.1 Visualisation

The analysis starts by visualising the monthly estimated POA irradiation and monthly yield per square meter. The POA irradiance is estimated using measurements from three weather stations located in different distances to the PV system, and the result for system 6 is shown in Figure 4.1. The first axis represents the months, the second axis represents the irradiation, and the third axis represents the yield, which is scaled by the module STC efficiency to enable comparison. In Figure 4.1, the yield follows the irradiation well every month. However, there are some deviations due to, for example, the modules' efficiency is not constant, resistance in the cables, and inverter loss. The differences are larger for all model combinations during May, June, and July that may be explained by an increased cell temperature. Ilseng meteorological station (the blue bars) shows large estimates compared to the other meteorological stations indicating a failure in that system. From the beginning of November until the end of February, the data from the meteorological station in Ilseng is incorrect and therefore, the station was removed from further use.

Figure 4.2 illustrates daily estimated POA irradiation per square meter and daily yield per square meter for system 6 in August. These plots show that the yield follows the irradiation well, as seen in the monthly plots (Figure 4.1). During days of low yield, the difference between yield and irradiation is smaller compared to days of high yield. For example, the difference for 10.08.18 and 22.08.18, which is two of the days with the lowest yield, have top three of the smallest relative difference (the difference between yield and irradiation normalised by the mean production) using the closest meteorological station.

Figure 4.3 is an example from system 6 of a clear day (30.06.2018). Again, two things are to be noted. First, the yield follows the irradiation well for all meteorological stations. And second, the difference between the hourly production and the estimated POA irradiance is largest during midday. This complements the observations for the daily values, as the cell temperature is at its highest during this period. Another observation is that the relative difference is largest during the morning and smallest during the night, which will be further discussed in section 4.3.

By further studying the plots, the difference between production and POA irradiance after midday is smaller compared to the equivalent hour before midday. For example, the relative difference for the data point 30.06.18 16:00 is smaller compared to the 30.06.18 08:00, where both are four hours from midday. This is also true for the other data points after sunrise and before sunset. This may be explained by the tilt and orientation of the system is somewhat inaccurate. For example, this system is oriented southwest (144°), and if the orientation is further west (<144°) the system will have a larger production after midday compared to a system oriented towards further south. The effect of orientation and tilt of the system will be further examined in section 4.1.2.1. Another explanation is that the apex of the plot does not correspond to the true apex of the Sun.

By looking at all the data, it was ensured that the data was as expected without any large out of service periods.

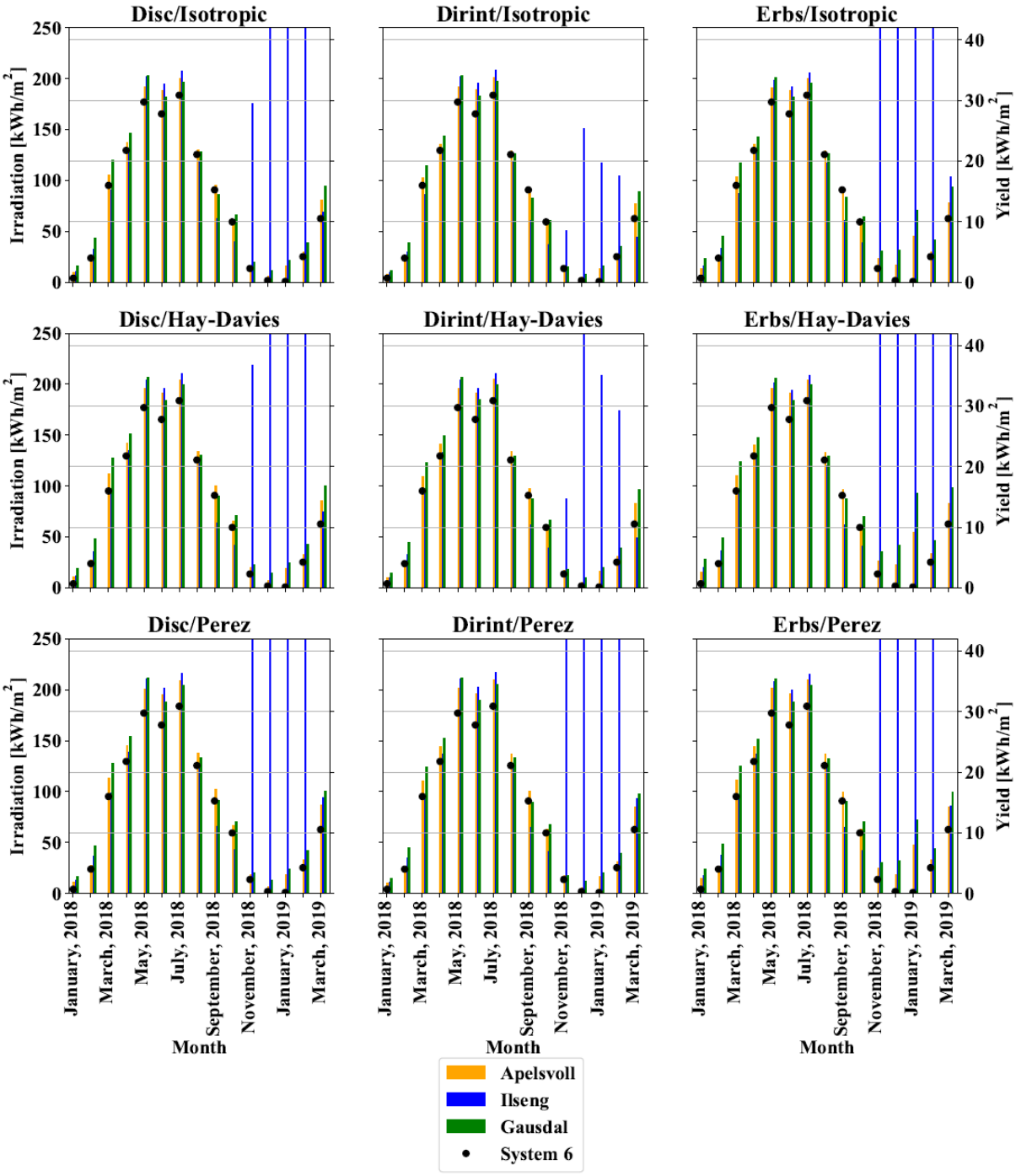

Figure 4.1: *Plots of nine different model combinations of system 6. Along the first axis is every month from January 2018 to March 2019. The estimated POA irradiation per square meter (yellow and blue bars corresponding to Apelsvoll, and Gausdal meteorological station) is along the second axis, while the yield per square meter (black dot) along the third axis. The third axis is scaled by the max efficiency of the PV module to enable comparisons.*

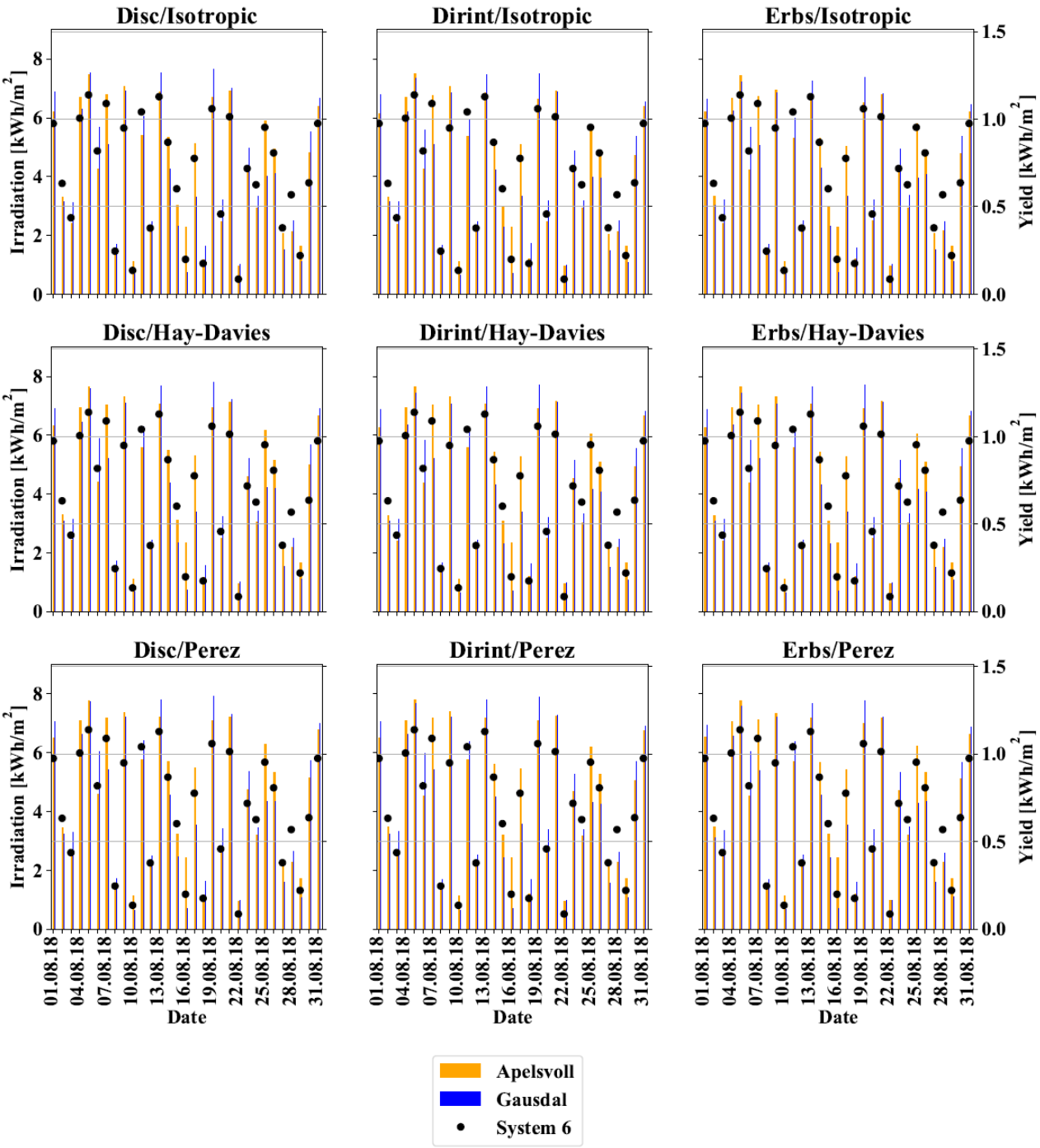

Figure 4.2: *Plots of nine different model combinations of system 6. Along the first axis is every day in August. The estimated POA irradiation per square meter (yellow and blue bars corresponding to Apelsvoll, and Gausdal meteorological station) is along the second axis, while the yield per square meter (black dot) along the third axis. The third axis is scaled by the max efficiency of the PV module to enable comparisons.*

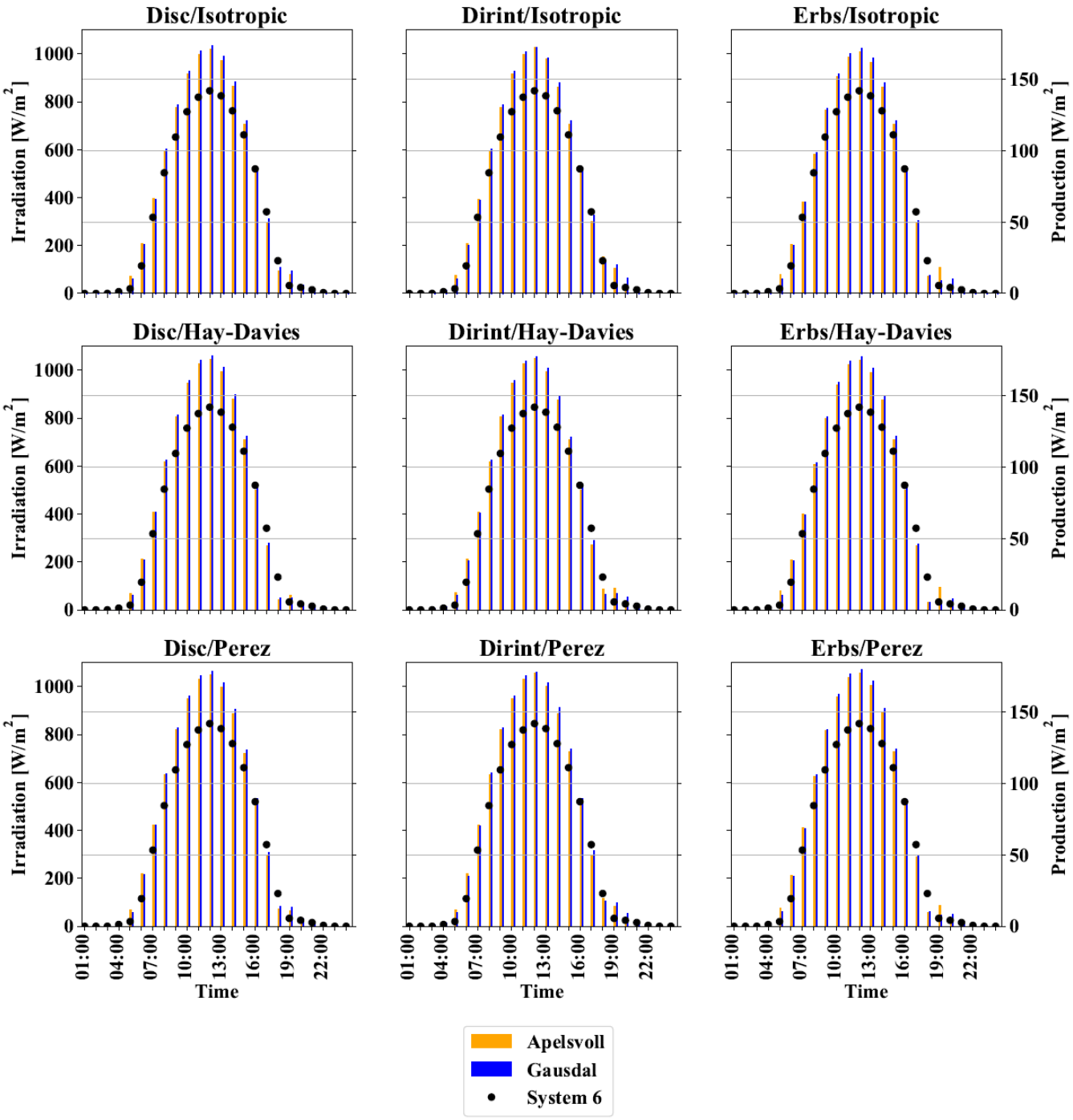

Figure 4.3: *Plots of nine different model combinations of system 6. Along the first axis is every hour of 30.06.2018. The estimated POA irradiance per square meter (yellow and blue bars corresponding to Apelsvoll and Gausdal meteorological station) is along the second axis (wrongly spelled in the plots), while the production per square meter (black dot) along the third axis. The third axis is scaled by the max efficiency of the PV module to enable comparisons.*

4.1.2 Model performance

To achieve an accurate evaluation of the models, measured POA irradiance data is needed for reference. The measurements were collected by CMP11 pyranometer produced by Kipp & Zonnen[33] oriented 173° with a 46° tilt, while GHI data was collected from the exact same location. This data was used to calculate *RMSE*, and the result is shown in Table 4.1. The *RMSE* was calculated five times with the albedo of 0.05, 0.10, 0.15, 0.25, and 0.35. The reason for the repetition was to evaluate the impact of albedo on the result because it is unknown. For reference, PVSyst define the different albedo ranges as follows[41]: 0.15-0.22 as urban environment, 0.15-0.25 as grass (0.26 for wet grass), 0.09-0.15 as dry asphalt (0.18 for wet asphalt), 0.25-0.35 as concrete (0.33 for red tiles), and 0.08 as dirty galvanised steel. The *RMSE* is calculated using data from the period December to March due to the correction of the tilt and orientation that was done in the beginning of December. The correction of tilt and orientation and its impact on the result are discussed later.

Table 4.1: *The RMSE of different models and albedos in the period from December to March.*

Models	$RMSE_{0.05}$ [W/m^2]	$RMSE_{0.10}$ [W/m^2]	$RMSE_{0.15}$ [W/m^2]	$RMSE_{0.25}$ [W/m^2]	$RMSE_{0.35}$ [W/m^2]
Disc/Isotropic	27.24	27.26	27.28	27.36	27.49
Disc/Hay-Davies	37.35	37.55	37.75	38.18	38.64
Disc/Perez	32.66	32.88	33.10	33.58	34.09
Dirint/Isotropic	25.04	24.88	24.74	24.48	24.28
Dirint/Hay-Davies	29.37	29.50	29.63	29.94	30.28
Dirint/Perez	27.36	27.52	27.70	28.04	28.43
Erbs/Isotropic	1159	1159	1159	1159	1159
Erbs/Hay-Davies	1654	1654	1654	1654	1654
Erbs/Perez	1159	1159	1159	1160	1160

The table shows that the albedo does not impact the result to a large extent, as the largest change of *RMSE* equals 1.43 W/m^2. Hence, it is decided to use the standard value of 0.25 as it is unknown and its low impact on the result.

Every model combination using Erbs has a very large *RMSE*. This can be explained by

overestimating the POA irradiance in days with low irradiance. One example is depicted in Figure 4.4. This may be explained by the small data set used to develop the model and the location it was collected. However, it was decided not to study this further. Other plots indicating the same is shown in appendix A.

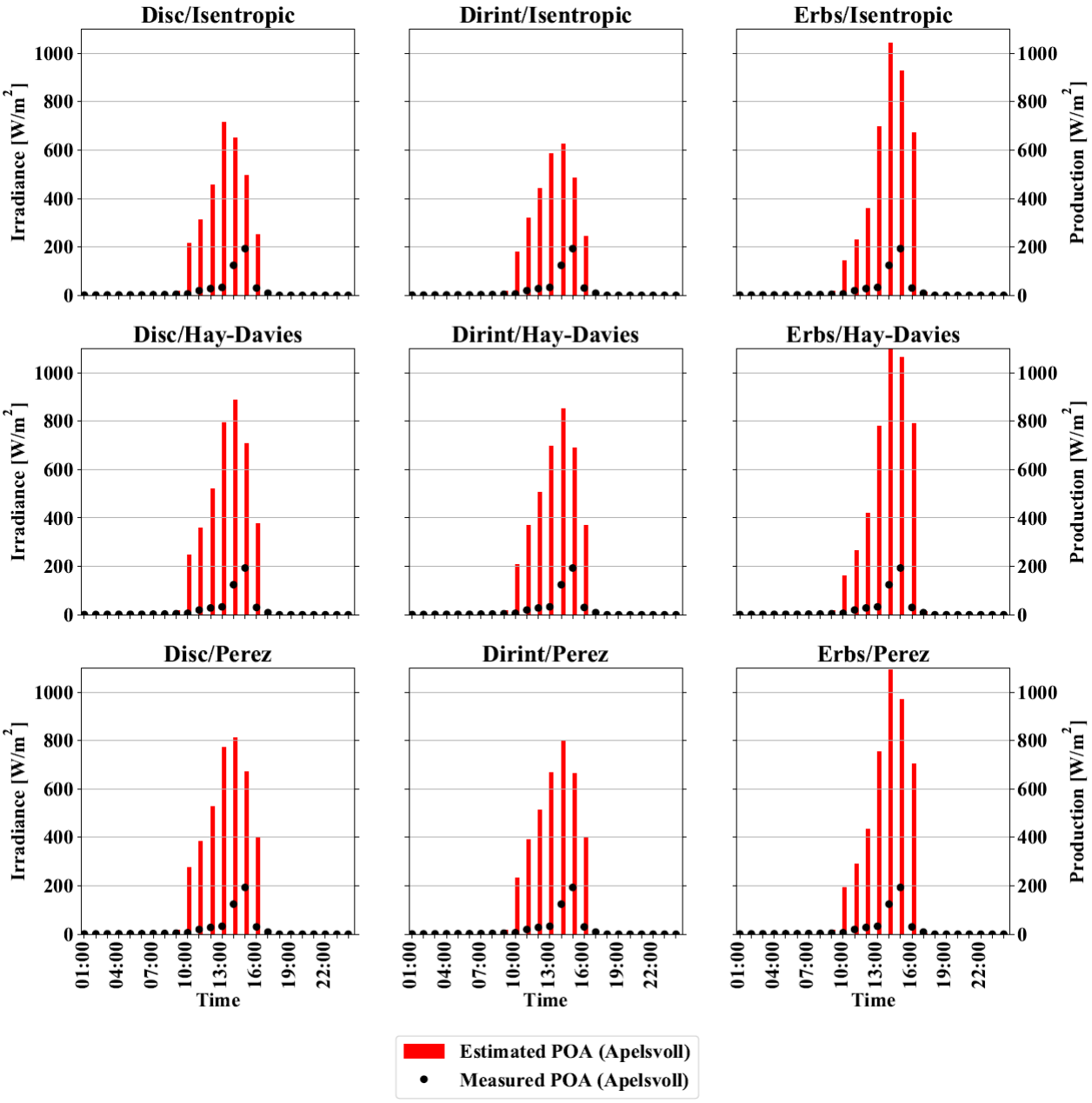

Figure 4.4: *Plots of nine different model combinations together with the measured POA irradiance of 11.02.19. It shows that models using Erbs tend to overestimate low irradiance. Along the first axis is time, estimated POA irradiance per square meter (red bars) is along the second axis, while the production per square meter (black dots) is along the third axis.*

The monthly, daily, and hourly values of the three model combinations with the smallest $RMSE_{0.25}$ (Dirint/Isotropic, Disc/Isotropic, and Dirint/Perez) were chosen to be studied further. The monthly plot is shown in Figure 4.5, the daily plot is shown in Figure 4.6, and the hourly plot is shown in Figure 4.7 and 4.9.

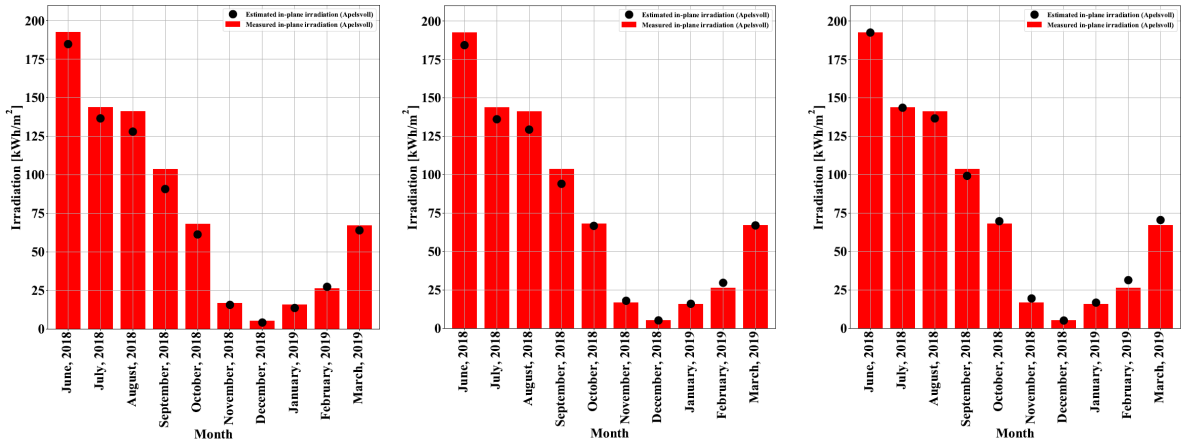

(a) *Dirint/Isotropic model combination*

(b) *Disc/Isotropic model combination*

(c) *Dirint/Perez model combination*

Figure 4.5: *Plots of the monthly measured (red) and estimated (black) in-plan irradiation for Apelsvoll test system. The data range from June, 2018 to March, 2019.*

Until December, the monthly plots shows that the Dirint/Isotropic (Figure 4.5a) and the Disc/Isotropic (Figure 4.5b) model combination slightly underestimate the true POA irradiation, while the Dirint/Perez model combination (Figure 4.5c) is more accurate. This is confirmed by calculating *RMSE* from June to December. After November, the Dirint/Isotropic model combination differs less to the true POA irradiation. The calculated *RMSE* in this period confirms this as well.

The change of performance may be explained by the correction of tilt and orientation that happened at the beginning of December. Another explanation is the different model combinations. M. Lave et al. found that the Isotropic sky model estimates a lower POA irradiance compared to the Hay-Davies model and the Perez model[16]. A smaller estimate provided by the Isotropic may benefit in Norwegian conditions as the irradiance is low during the winter period.

The plots of the daily values (Figure 4.6) in August illustrate the same. For days of high yield (for example 05.08.2018, 13.08.2018, and 21.08.2018), the Dirint/Perez model

combination (Figure 4.6c) approximate values closer to the true irradiance compared to the Dirint/Isotropic (Figure 4.6a) and the Disc/Isotropic (Figure 4.6b) model combination. This is also true for less clear days such as 16.08.2018. In general, for low irradiation days (e.g. 10.08.18, 18.08.18, and 22.08.18) are all models somewhat accurate by using the closest meteorological station. This may indicate that the Dirint/Isotropic model combination performs best in locations where the total POA irradiance is low, while the Dirint/Perez performs best in high irradiance periods.

Finally, the POA irradiance estimates for a clear day (30.06.18) in hourly resolution are shown in Figure 4.7. The plots show that all model combinations perform well. The Dirint/Perez model combination (Figure 4.7c) is more accurate before noon, while the Dirint/Isotropic (Figure 4.7a) and Disc/Isotropic (Figure 4.7b) model combination are more accurate after noon.

To assess whether this change of performance is only an effect of a wrong instrument tilt, a plot of a clear day in March is shown in Figure 4.8. This is important as the measured tilt of the pyranometer and the tilt of the systems, which is further studied in section 4.1.2.1, is somewhat uncertain. Due to a mismatch between estimated and measured irradiance, only the second half of the day can be used for this purpose. The second part, indicate that the Dirint/Perez provide an estimate more accurate for midday conditions (i.e. high irradiance), and overestimates periods with less irradiance. In contrast, the Disc/Isotropic and the Dirint/isotropic are less accurate

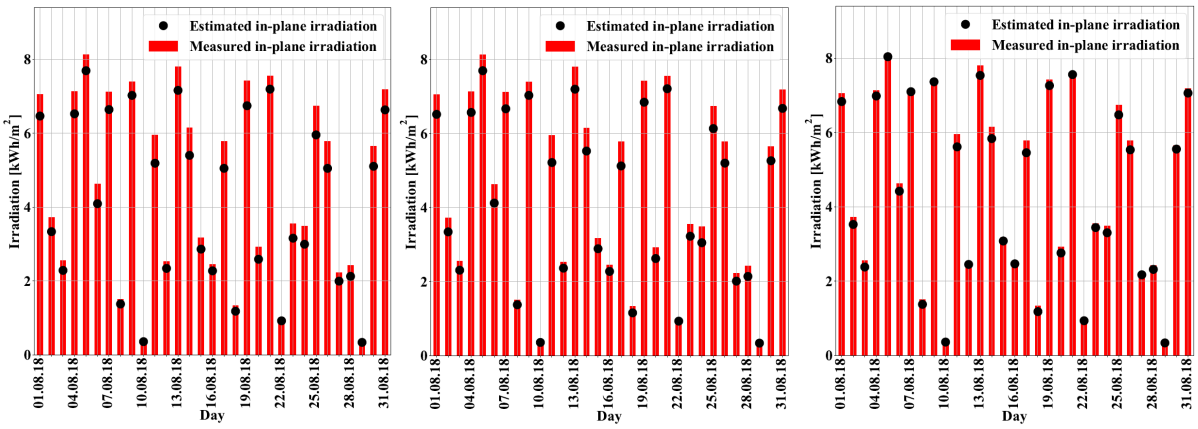

(a) *Dirint/Isotropic model combination*

(b) *Disc/Isotropic model combination*

(c) *Dirint/Perez model combination*

Figure 4.6: *Plots of the daily measured (red) and estimated (black) in-plan irradiation for Apelsvoll test system. The data is from August, 2018.*

during the high irradiance period, but more accurate during periods with lower irradiance.

Regarding the periods 05:00-06:00 and 19:00-20:00 in Figure 4.7, all models estimate a larger irradiance compared to the actuall irradiance. The diffuse fraction is large during these periods that suggest that the diffuse irradiance is overestimated in clear periods (also found by M. Lave et al. [16]). Another reason may be the increased uncertainty of the pyranometer under low irradiance.

A plot of a cloudy day is illustrated in Figure 4.9. This shows that the Dirint/Perez overestimates cloudy days while Dirint/Isotropic model combination estimates more accurately, which was also confirmed by calculating *RMSE* for this day. This may be explained by the data set used to estimate the empirical coefficients in the Perez model. Another explanation may be the AM estimation used in the Perez model.

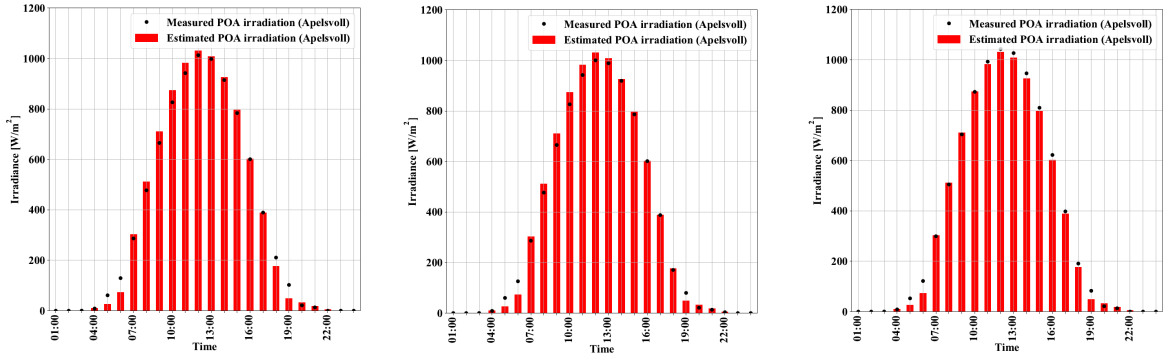

(a) *Dirint/Isotropic model combination*

(b) *Disc/Isotropic model combination*

(c) *Dirint/Perez model combination*

Figure 4.7: *Plots of the hourly measured (red) and estimated (black) in-plan irradiation for Apelsvoll test system on a clear day (30.06.2018).*

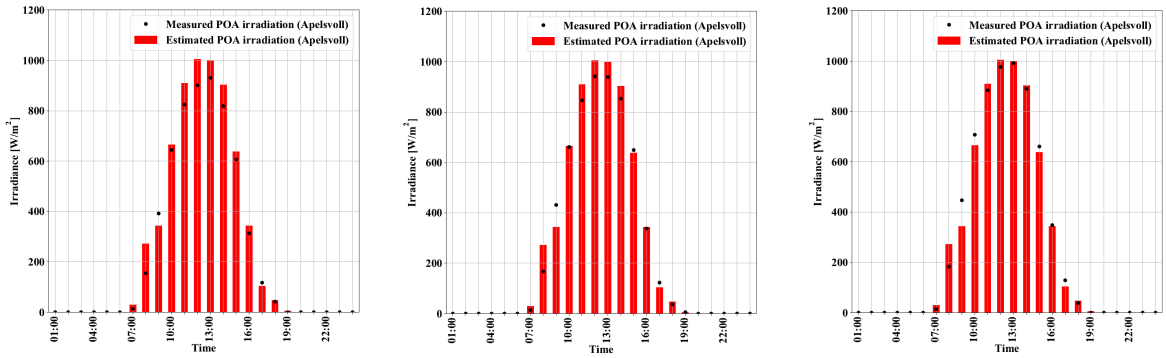

(a) *Dirint/Isotropic model combination*

(b) *Disc/Isotropic model combination*

(c) *Dirint/Perez model combination*

Figure 4.8: *Plots of the hourly measured (red) and estimated (black) in-plan irradiation for Apelsvoll test system on a clear day (20.03.2019).*

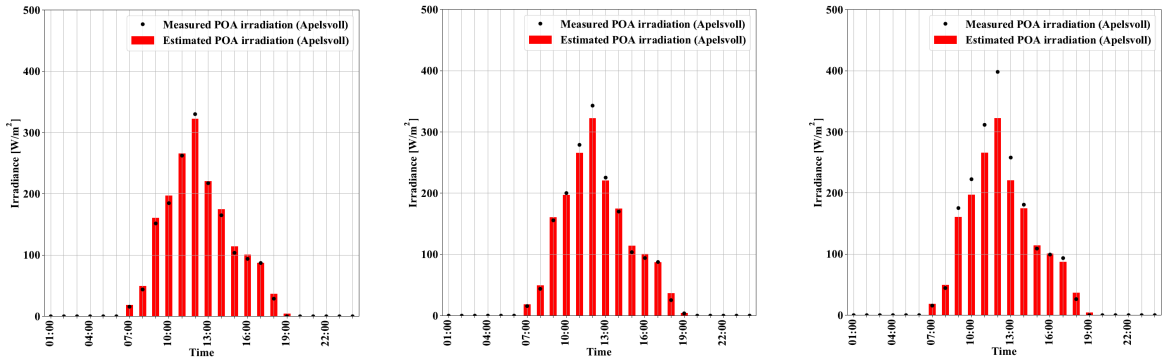

(a) *Dirint/Isotropic model combination*

(b) *Disc/Isotropic model combination*

(c) *Dirint/Perez model combination*

Figure 4.9: *Plots of the hourly measured (red) and estimated (black) in-plan irradiance for Apelsvoll test system on a cloudy day (15.11.2018).*

4.1.2.1 Orientation and tilt

To assess the effect of system tilt on the irradiance models, the *RMSE* was calculated for 90%, 100%, and 110% of given tilt. The result is shown in Table 4.2. Most models respond to a decrease of tilt by a decrease of *RMSE*. This can be explained by a lower tilt before correction. On the other hand, the Dirint/Isotropic model combination reacts in the opposite way. For the chosen models (Disc/Isotropic, Dirint/Isotropic, and Dirint/Perez), the largest change of *RMSE* is 3.91 W/m^2. That means that tilt causes a larger change compared to the effect of albedo. However, it is still small compared to the irradiance on a clear day in the summer.

Table 4.2: *The RMSE for different models and tilts. Note that $RMSE_{t,100\%}$ is equal $RMSE_{0.25}$, and that the orientation is kept constant.*

Models	$RMSE_{t,90\%}$ [W/m^2]	$RMSE_{t,100\%}$ [W/m^2]	$RMSE_{t,110\%}$ [W/m^2]
Disc/Isotropic	26.33	27.36	28.75
Disc/Hay-Davies	34.41	38.18	41.79
Disc/Perez	30.59	33.58	36.52
Dirint/Isotropic	25.10	24.48	24.38
Dirint/Hay-Davies	27.64	29.94	32.37
Dirint/Perez	26.18	28.04	30.09
Erbs/Isotropic	1066	1159	1245
Erbs/Hay-Davies	1519	1654	1778
Erbs/Perez	1066	1160	1246

To study the effect of system orientation, the *RMSE* was calculated for 90%, 100%, and 110% of the given orientation, and put into Table 4.3. The result shows that the orientation of the system affects the performance more compared to albedo and tilt, as expected. The $RMSE_{o,90\%}$ (i.e. a orientation further west compared to given orientation) is lower for most model combinations compared to $RMSE_{o,100\%}$ and $RMSE_{o,110\%}$. The explanation for the large increase of the 110% orientation may be due to the system's plane is oriented towards the south receive much more irradiance during the day. Thus, the deviation becomes larger.

4.1.2.2 Uncertainties

As the tilt and orientation of the pyranometer is uncertain in the period June until December, it was decided not to use this period in the *RMSE* calculation. This is because the tilt and orientation has a large impact on the total irradiation received by a plane. That being said, the result for this period suggested that the Perez has a better performance, especially during the summer. Also, the uncertainty of the pyranometer increase in low irradiance resulting in a larger uncertainty in the winter.

Table 4.3: *The RMSE for different models and orientations. Note that $RMSE_{o,100\%}$ is equal $RMSE_{0.25}$, and that the tilt is kept constant.*

Models	$RMSE_{o,90\%}$ [W/m^2]	$RMSE_{o,100\%}$ [W/m^2]	$RMSE_{o,110\%}$ [W/m^2]
Disc/Isotropic	26.80	27.36	34.95
Disc/Hay-Davies	31.88	38.18	47.70
Disc/Perez	28.85	33.58	42.63
Dirint/Isotropic	27.35	24.48	29.59
Dirint/Hay-Davies	26.89	29.94	38.25
Dirint/Perez	25.82	28.04	35.92
Erbs/Isotropic	789	1159	1440
Erbs/Hay-Davies	1099	1654	2073
Erbs/Perez	789	1160	1441

4.1.3 Section summary and conclusion

The first subsection illustrated the data to follow the irradiance well on monthly and daily time resolution. It also indicated, although not shown, that the data was continuous without any large periods out of service.

As discussed in the second subsection, the Perez/Dirint model combination performs best in high irradiance periods, while it often overestimates the low irradiance period. The Dirint/Isotropic model combination is opposite. It performs well under low irradiance periods, while it underestimates high irradiance periods. This also corresponds to another study[16] that found the Perez model provides a larger estimate compared to the Isotropic model. Furthermore, the *RMSE* for the period from December to March is the smallest for the Dirint/Isotropic model combination. Therefore, it may be beneficial to use the Isotropic sky model in Norway as the irradiance is low, especially during winter.

A final argument for the Isotropic model is that it requires fewer input parameters compared to Perez. As most household PV systems do not have devices that measure all the required input parameters, it is better to avoid models that require them as input. This is to reduce uncertainty in the calculation.

The Dirint model was chosen as the transposition model since its performance is best throughout this study. Compared to Disc, the Dirint model is very similar. However, the empirical coefficients in the Dirint model are based on a larger data set collected from a broader range of climatic conditions. This may explain why the Dirint model generalise well to Norway's irradiance conditions. Based on this, it is decided to use the Dirint/Isotropic model combination in the later analysis of the PV systems.

4.2 Assessment of irradiance model performance using data from another location

After deciding which decomposition and transposition models to use, it was necessary to study how accurate GHI data is over large distances. This is important as most areas do not have pyranometers. To do this, data from 10 different meteorological stations were chosen and used to calculate the *RMSE* for the period December to March. The result is shown in Table 4.4, and a plot of the monthly irradiation is shown in Figure 4.10.

Table 4.4 shows that the *RMSE* varies from 61.59 W/m^2 to 82.19 W/m^2, which is large compared to the result using data from Apelsvoll. However, it does not look like the performance is explained by the distance alone. Altitude does neither explain the variation of performance. For all systems located south for Apelsvoll, the *RMSE* is below 72 W/m^2, while all stations located North, East, and West has a *RMSE* above 72 W/m^2. This indicate that cardinal directing is affecting the performance more than distance itself. This may be explained by the local climate at that location. For example, station 13030 is located within a valley, while the Apelsvoll is close to a lake resulting in different local climates. Station 20540, 18700, and 19940 are also located close to lakes suggesting similar climate conditions and lower *RMSE*. Another example is station 26990. This weather station is located nearby mountains that may result in different climate compared to Apelsvoll, hence a larger *RMSE*.

Figure 4.10 shows that until December, all meteorological stations underestimated the irradiance compared to the true irradiance in Apelsvoll, with 18700 as the exception. This corresponds to the previous findings where Dirint/Isotropic underestimate the irradiance before the correction of orientation and tilt. However, after November, the estimated irradiance vary more for the different stations.

Table 4.4: *The RMSE values for the meteorological stations spread over the southeastern part of Norway. Distance is the length between the meteorological station and the location of the POA irradiance measurements. The cardinal (or intercardinal) direction means in which direction (North, South, East, West) the meteorological stations are located compared to Apelsvoll.*

Station number	Station name	*RMSE*	Distance [km]	Cardinal Direction	Altitude
11500	Apelsvoll	24.48	0		264
20540	Gran	61.59	38	S	245
13030	Gausdal	75.93	66	N	375
20280	Hønefoss	67.73	68	S	126
5660	Roverud	82.19	82	SE	170
18700	Oslo	70.96	85	S	94
13150	Fåvang	75.24	85	N	200
19940	Lier	71.07	98	S	39
26820	Hokksund	69.78	116	S	15
26990	Sande	78.53	134	SW	60

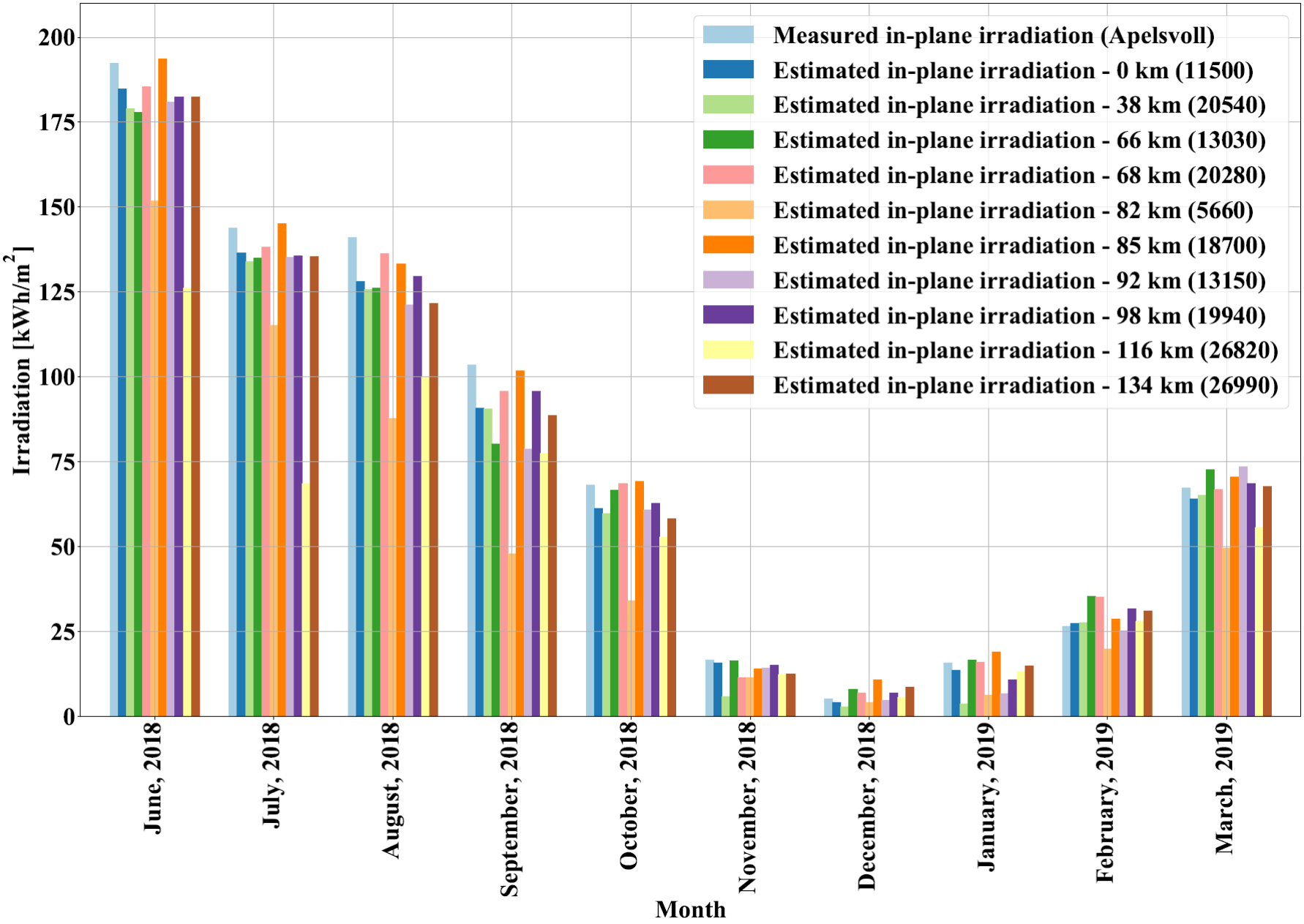

Figure 4.10: *A plot of the monthly measured irradiance and the monthly estimated POA irradiance using the different meteorological stations.*

During June and July, the monthly estimates are reasonably close to the POA irradiance measurements in Apelsvoll, having the underestimation in mind. However, in the autumn and winter, the difference between the weather stations increase. While station 5660 and 26820 are constantly providing too low estimates, other stations, such as 11500, 20540, and 26900, differ more in August, September, and October. In the mid-winter period, most stations are providing similar results as the irradiance is low. Also in February and March is the total irradiation reasonably close.

Figure 4.11 shows that most meteorological stations are not generally useful in daily time resolution, especially during the winter, spring, and autumn. For example, scattered clouds do not evenly spread out resulting in different irradiance in Apelsvoll compared with Gausdal. However, in clear periods as illustrated in Figure 4.12, all meteorological stations are estimating similar results close to the true value. Besides, the meteorological stations are estimating similar results for the day with the lowest irradiation. This suggests that for clear days, and days with complete cloud cover, most meteorological stations located in similar local climates measure similar irradiance.

To further investigate the variation during the different months, *NRMSE* (*RMSE* normalised by the mean irradiance) was calculated and put into Table 4.5. The result shows an increasing *NRMSE* moving towards December before it decreases when moving towards summer again. That suggests that meteorological stations in another location are most accurate during summertime, where the number of clear days is largest.

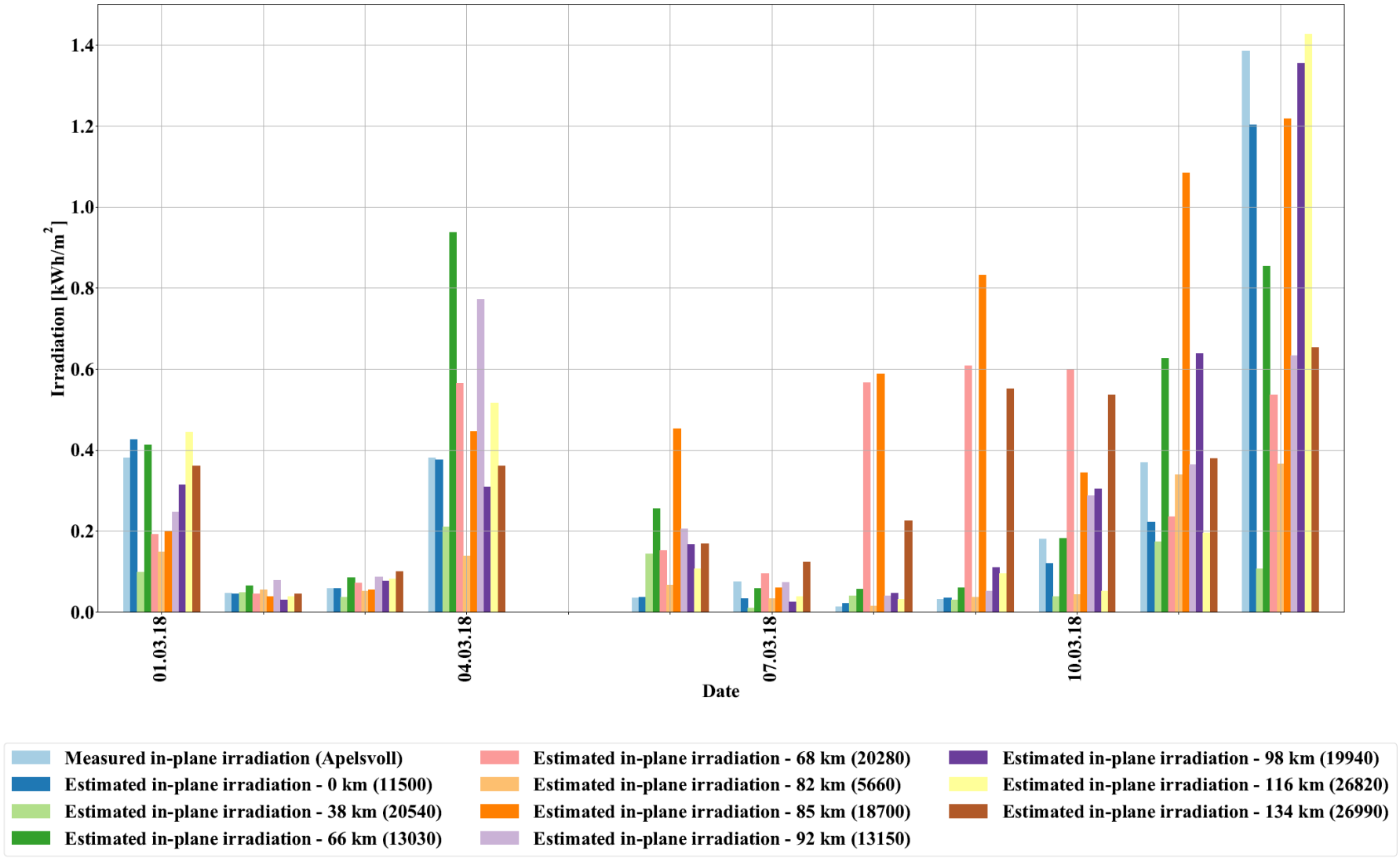

Figure 4.11: *A plot of the daily measured irradiance and the daily estimated POA irradiance in a part of December using the different meteorological stations.*

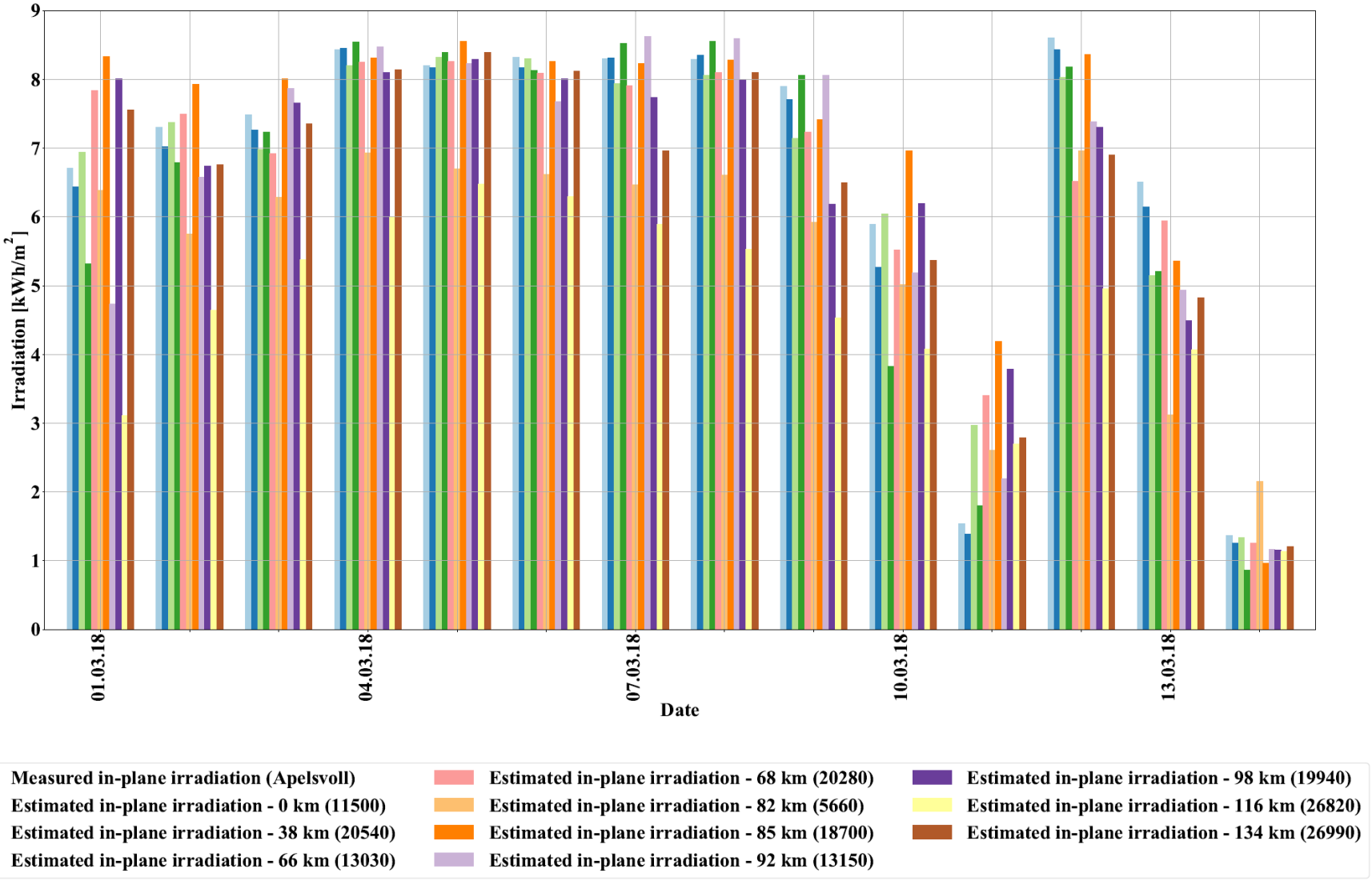

Figure 4.12: *A plot of the daily measured irradiance and the daily estimated POA irradiance in a part of June using the different meteorological stations.*

Table 4.5: *An overview of the monthly NRMSE for the different weather stations.*

Station	Jun [%]	Jul [%]	Aug [%]	Sep [%]	Oct [%]	Nov [%]	Dec [%]	Jan [%]	Feb [%]	Mar [%]
Apelsvoll	10.2	14.9	18.4	29.4	42.4	81.4	171	147	56.7	31.9
20540	39.9	44.4	56.5	75.2	118	320	432	358	140	78.7
13030	46.8	47.0	60.7	93.7	119	255	522	257	248	105
20280	45.8	44.1	57.8	88.7	120	219	482	355	187	85.0
5660	69.1	78.4	93.4	147	172	258	402	292	213	134
18700	46.2	42.5	58.8	85.6	117	255	606	268	234	89.4
13150	46.2	54.8	69.3	102	127	206	395	334	220	106
19940	46.8	53.8	64.1	103	124	219	353	334	207	96.7
26820	75.8	121	82.8	100	138	175	285	326	201	97.3
26990	46.9	51.4	78.6	112	142	254	528	343	214	113

4.2.1 Uncertainties

Another explanation of large *NRMSE* of the winter months is that the low irradiance causes the pyranometers to be more inaccurate. Additionally, the Sun has a lower elevation during the winter months causing the weather station to be prone for shadows disturbing the measurements. A final explanation is that hourly values are used. There are more clouds during the winter resulting in different hourly measurements, although the total irradiation may not vary that much.

As seen in Table 4.5, the *NRMSE* are above 100% during a large periods of the year. This is explained by the mean taken of the month also include night time values causing a lower monthly mean. The result shows nonetheless the general conclusion: meteorological stations located away from the wanted area are more accurate under clear periods.

4.2.2 Section summary and conclusion

Although some differences, it is shown that most meteorological stations in the chosen area are estimating similar irradiation in monthly time resolution. In daily time resolution, the differences vary more due to different cloud conditions. On the other hand, clear days (i.e. days with irradiation) and cloudy days (complete cloud cover and low irradiation) do provide similar irradiation, as expected.

Therefore, it was decided that Apelsvoll and Gausdal can be used in the analysis of the PV systems as long as they are located in the same area.

4.3 PV system

4.3.1 System performance

The total temperature corrected performance ratio was calculated according to eq. (2.18), and the result is shown in Table 4.6.

Table 4.6: *An overview of the total and monthly temperatuer corrected performance ratio (PR_{corr}) for the systems.*

Month	1	2	3	4	5	6	7	8	9	11	12	14	15
January	0.176	0.000	0.000	0.000	0.000	0.446	0.000	0.000	0.000	0.000	0.000	0.000	0.000
February	0.000	0.000	0.000	0.000	0.204	0.936	0.000	0.000	0.000	0.000	0.000	0.000	0.000
March	0.410	0.000	0.000	0.000	0.482	0.951	0.395	0.000	0.000	0.000	0.000	0.000	0.000
April	0.860	0.935	0.000	0.000	0.835	1.015	0.781	0.000	0.000	0.000	0.000	0.000	0.000
May	0.956	0.978	0.000	0.942	0.897	1.041	0.790	0.961	0.000	1.004	0.000	0.000	0.000
June	0.940	0.938	0.000	0.919	0.915	0.984	0.948	0.922	0.000	0.947	0.000	0.000	0.914
July	0.940	0.964	0.000	0.967	0.895	1.050	0.942	0.942	0.000	0.987	0.000	0.000	0.927
August	0.947	0.929	0.802	0.983	0.888	1.063	0.957	0.895	0.918	0.999	0.928	1.123	0.973
September	0.972	0.866	0.914	0.900	0.855	1.056	0.920	0.837	0.877	0.908	0.953	1.028	0.904
October	0.891	0.661	0.759	0.775	0.711	1.073	0.823	0.735	0.819	0.921	0.878	1.102	0.850
November	0.568	0.264	0.288	0.534	0.524	0.885	0.762	0.739	0.753	0.787	0.759	0.798	0.673
December	0.223	0.088	0.088	0.202	0.106	0.334	0.073	0.315	0.806	0.342	0.293	0.622	0.259
January	0.000	0.000	0.061	0.039	0.013	0.048	0.018	0.125	0.713	0.000	0.051	0.571	0.000
February	0.435	0.200	0.668	0.470	0.023	0.896	0.110	0.582	0.860	0.000	0.000	0.862	0.284
March	0.545	0.501	0.806	0.450	0.498	0.826	0.416	0.609	0.914	0.198	0.000	0.994	0.647
Aug.-Mar.	0.728	0.604	0.735	0.671	0.579	0.925	0.616	0.696	0.864	0.613	0.559	0.992	0.718
Total	0.815	0.846	0.750	0.844	0.756	0.987	0.782	0.835	0.864	0.841	0.603	1.01	0.0828

In general, all systems perform above 0.7 in the period April to October, while it drops for most systems in November. Looking at PR_{corr} in hourly resolution may explain why the systems are not closer to 1. Figure 4.13, 4.14, and 4.15 are examples of hourly PR_{corr} for system 1, 4, and 5 in the period 29.06.18 to 01.07.18, which were defined earlier as clear days. Similar plots from other systems are shown in appendix E.

These plots show that the systems have a reduction of performance during the early morning before it increases again and stabilises during midday. In the evening, the performance increase above 1. This is a general pattern followed by most systems, as seen in appendix E.

Reason for $PR_{corr} < 1$

The low performance may be explained by the following factors:

- Overestimation of irradiance in clear periods
- Height differences between the horizons of the PV system and meteorological system
- Nearby objects causing shadows
- Reflection
- Difference between irradiance conditions between the PV system and the meteorological system location
- Soiling
- Cable and inverter losses

Overestimation of irradiance in clear periods may be another explanation for low performance. For example, system 1,4, and 5 (Figure 4.13, 4.14, and E.2), which are oriented to the west, have a low morning performance. The reason is that systems oriented to the west have a larger fraction of diffuse irradiance on their modules as the Sun is in the east. As the input data is of a clear day, and as the Isotropic sky model is assuming constant diffuse irradiance from the entire celestial sphere, it may overestimate the diffuse fraction. The explanation may be the model's assumption of reflection from the entire sky dome and ground when it is mostly reflected from the ground since the celestial sphere has no clouds during a clear day. **Usikker på siste argument**

This argument can be strengthened by looking at a cloudy day. A temperature corrected PR plot from 30.03.2019 is shown in Figure 4.16. This shows a better performance throughout the day because there are more clouds, thus more reflection, and a more accurate diffuse irradiation estimate.

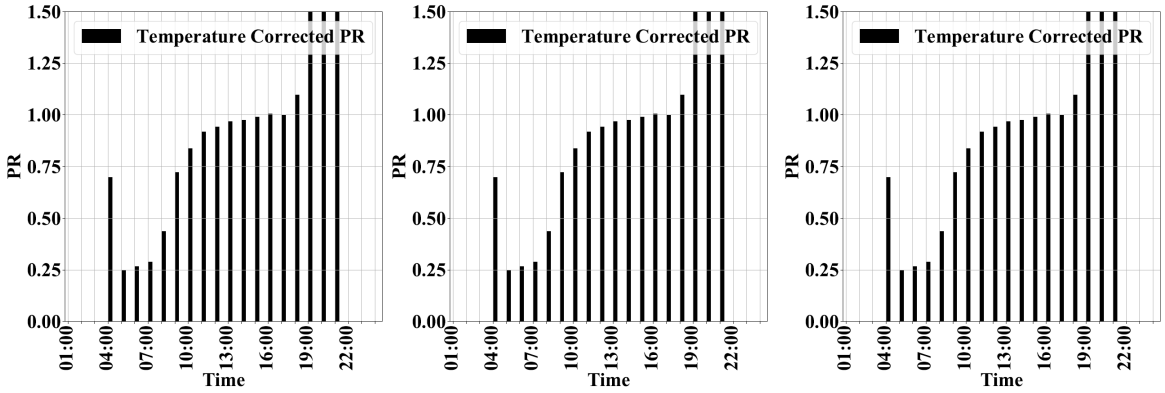

(a) *29.06.18* (b) *30.06.18*

Figure 4.13: *Plots of PR_{corr} of system 1 in three consecutive days in June and July.*

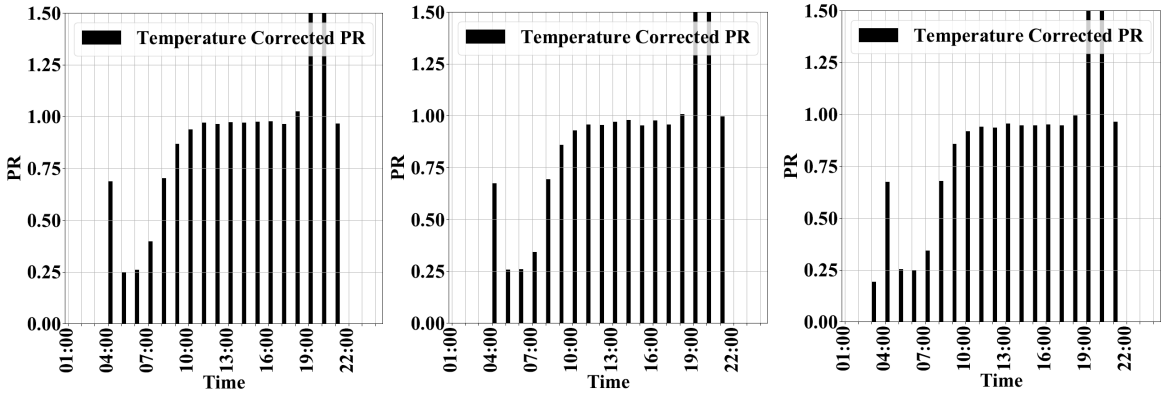

(a) *29.06.18* (b) *30.06.18* (c) *01.07.18*

Figure 4.14: *Plots of PR_{corr} of system 4 in three consecutive days in June and July.*

Another argument is the conclusion of the assessment done by M. Lave et al. This study found the Isotropic sky model to overestimate the diffuse irradiance in clear locations[16]. What they defined as a "clear location" is somewhat diffuse. However, if a "clear location" corresponds to a location with many clear days, this may be an argument for the low irradiance during the morning of a clear day, assuming the morning to be clear as well.

Following this argument, the same effect should be visible during the evening for systems oriented east. System 6 and 11 are both oriented to the east, and the dips during the evening

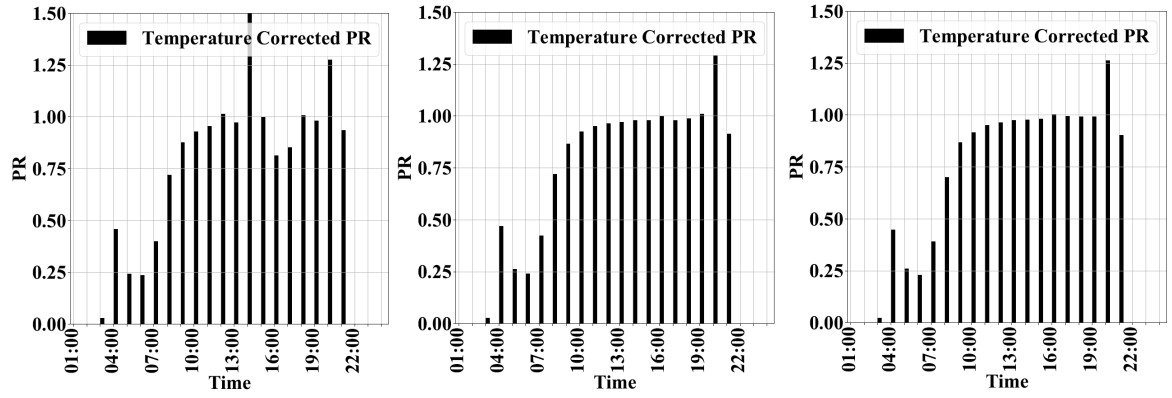

(a) *29.06.18* (b) *30.06.18* (c) *01.07.18*

Figure 4.15: *Plots of PR_{corr} of system 5 in three consecutive days in June and July.*

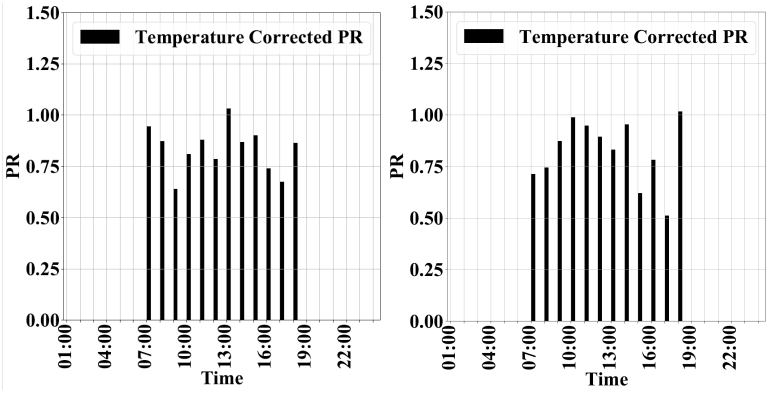

(a) *System 1* (b) *System 4*

Figure 4.16: *Plots of temperature corrected PR of system 1 and 4 in 30.03.19 (cloudy day).*

are seen in Figure E.2 and 4.18. Performance dips during the morning of system 6 may also be explained by the same underestimation, as the drop is smaller compared to system 11 that has trees located east for the system.

Height differences between the horizons of the PC systems and meteorological systems may explain the low performance. For example, system 1 has a forest located in the east, system 4 has a tree located nearby to the west, and system 5 has a mountain range located in front of it. This will reduce the incoming irradiance resulting in lower production of the PV plant. If this is the case, the low performance will increase towards winter as the elevation of the Sun is reduced.

Nearby objects causing shadows is a third reason for the low PR_{corr}. Due to the Sun's low elevation, objects in the horizon of the PV system may result in a lower irradiance on

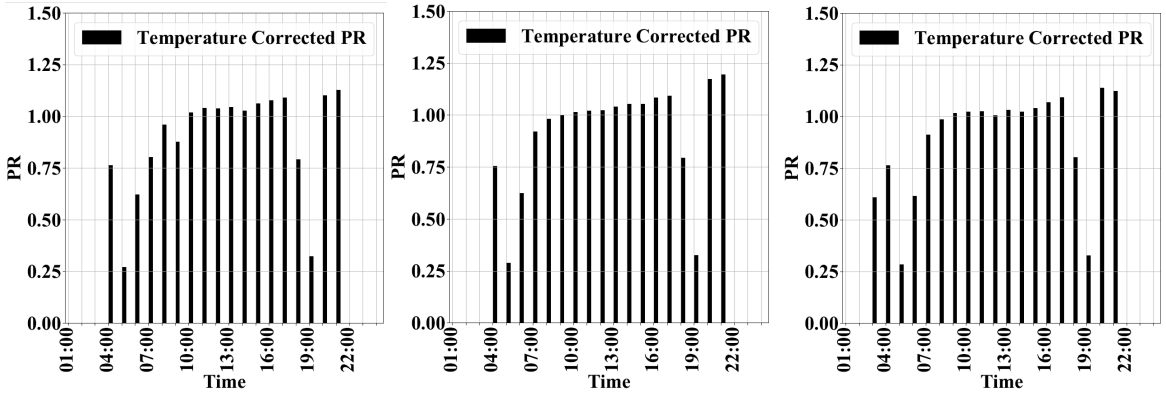

(a) *29.06.18* (b) *30.06.18* (c) *01.07.18*

Figure 4.17: *Plots of temperature corrected PR of system 6 in three consecutive days in June and July.*

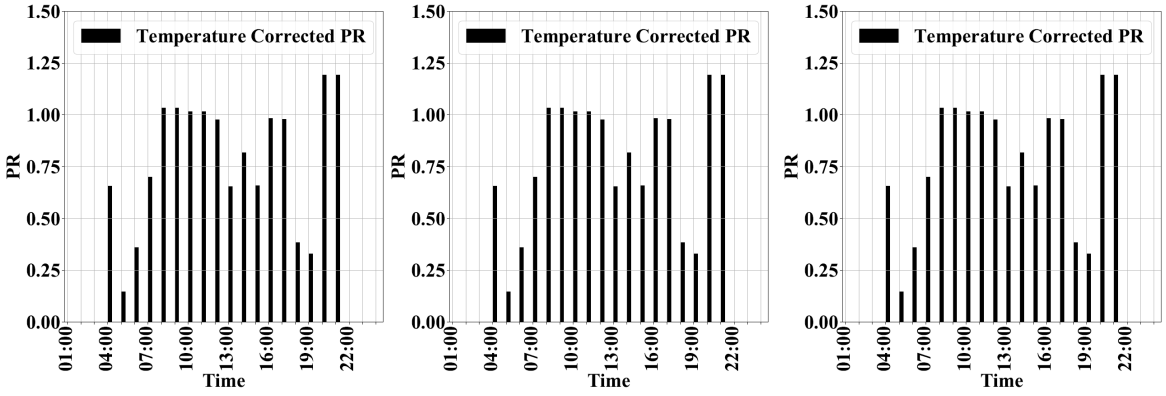

(a) *29.06.18* (b) *30.06.18* (c) *01.07.18*

Figure 4.18: *Plots of temperature corrected PR of system 11 in three consecutive days in June and July.*

the modules. System 1, 2, 4, 5, 7, 8, 11, and 14 have objects that may cause losses due to shadows, although not always observed in the hourly PR_{corr} plots. This increase the reduction of performance towards mid-winter.

Reflection is a fourth explanation of low performance. This is relevant during the mornings and mid-winter as the Sun is at the lowest, and the diffuse fraction is larger. As the diffuse irradiance comes from all directions, a part of the light is always reflected. Additionally, when the Sun elevation is low, the angle of incident on the modules becomes larger, especially for systems with a small module tilt.

A fifth explanation is differences between clearness of sky in the morning and midday. For example, there may be fog in the morning causing the irradiance to be lower at the PV systems compared to the meteorological station. However, this may also be the case in Apelsvoll.

The sixth explanation is soiling. Dust and other objects may accumulate on the PV modules preventing the irradiance from reaching the PV module. This is one of the main reasons for low performance during winter as snow cover the modules. Additionally, frost and the low Sun elevation also result in a low production [42]. The corresponding low performance continues until April when the snow has melted, and the Sun rises taller on the celestial sphere.

A final explanation is losses connected to the cable and the inverter. Cables have resistance causing loss proportional to length and diameter. The losses connected to the cable is not further studied as the length and type of cable in the systems are unknown. Inverter losses are also present, especially during low power output. Furthermore, the inverter starts to operate at a certain voltage which may cause the lowest irradiance periods to be lost. This is further discussed in section 4.4.

Reason for $PR_{corr} > 1$

$PR_{corr} > 1$ may be explained by the following factors:

- Underestimation of irradiance using the Isotropic sky model
- Height differences between the horizons of the PV system and meteorological system
- Higher irradiance differences between the location of the PV system the meteorological station

As stated earlier, the Isotropic model is generally underestimating the irradiance in high irradiance periods, as discussed in section 4.1.2. This will cause the PR_{corr} to be overestimated during high irradiance periods.

Similar to what discussed in the last section, a higher irradiance in the location of the PV module compared to the site of the meteorological station will make the PR_{corr} large. For example, there may be more cloud cover during the year in Apelsvoll compared to the location of system 6 and 14 resulting in a particularly large performance ratio.

PR_{corr} above 1 in hourly time resolution may be explained by a lower horizon at the PV module location compared to the meteorological station. Plotting hourly PR_{corr} for system 5 using both GHI data from Gausdal and Apelsvoll strengthen this argument. Figure 4.15 and 4.19, which is of the same three days but by using GHI data from Gausdal and Apelsvoll

respectively, show a lower increase of performance during the evening when using data from Gausdal (Figure 4.15) compared to data from Apelsvoll (Figure 4.19). This is explained by differences in irradiance due to differences in the horizon between Gausdal and Apelsvoll.

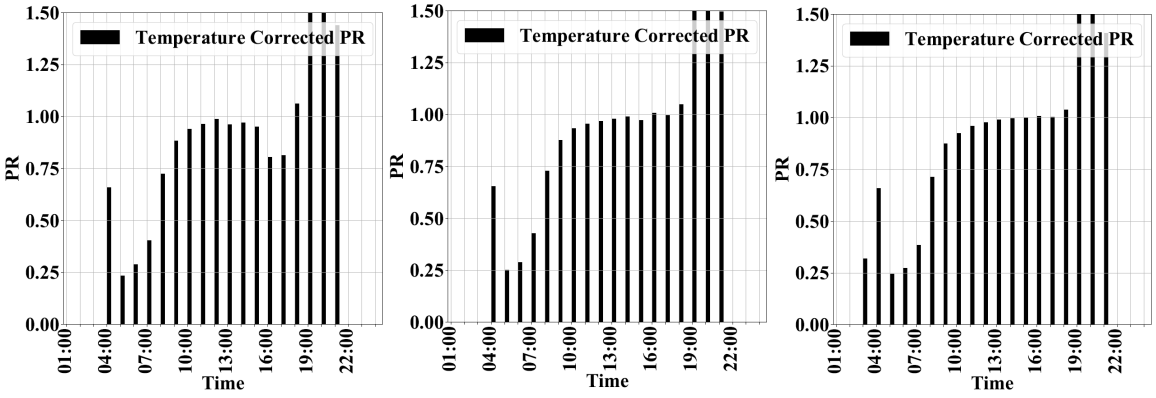

(a) *29.06.18* (b) *30.06.18* (c) *01.07.18*

Figure 4.19: *Plots of PR_{corr} of system 5 in three consecutive days in June and July.*

Uncertainty

On the other side, there are several factors that may cause PR_{corr} the uncertainty to increase. Some of the factors are:

- Pyranometer measurement uncertainty
- Inverter readings uncertainty
- Differences in weather in hourly time resolution
- Cell temperature estimation
- Errors in tilt and orientation

The first factor is the pyranometer uncertainty. This was stated to be 2% for hourly GHI values. Additionally, the meteorological stations need regular maintenance to maintain a low uncertainty, and it is not known whether the pyranometers used in this thesis are maintained regularly, or not. If maintenance is not done regularly, dirt may accumulate on the sensor, or humidity in the air may condense on the sensor causing the measurements to be inaccurate.

Thermal offset will give additional uncertainty to the measurements during low irradiance periods, while temperature differences change the measurements.

Inverter readings are also highly inaccurate. The uncertainty of the Fronius inverters has been stated to be 5%, while the uncertainty of the Steca inverters is unknown. However, M. Richter et al. reported that the uncertainty of PR could range between $\pm 4\%$ to $\pm 6\%$ if the pyranometers were of low quality and if direct inverter readings are used[39]. As the systems in this thesis use irradiance measurements from another location and inverter readings, it may be assumed that the uncertainty of the PR_{corr} are similar.

Differences in weather conditions in hourly time resolution also complicate the performance calculations. In the plots shown above (Figure 4.13 to 4.19), in appendix E, in section 4.2, and in Figure 4.20 below, it is clear that it is hard to evaluate systems accurate on hourly basis using data from another location. The reasons are the difference in irradiance, especially in days with shifting cloud cover. This results in a varying level of accuracy in daily time resolution that also was shown in section 4.2. Although the monthly PR_{corr} is somewhat inaccurate, Table 4.6 shows that the monthly and total PR_{corr} are more reasonable, as the total GHI recordings are more stable over large areas.

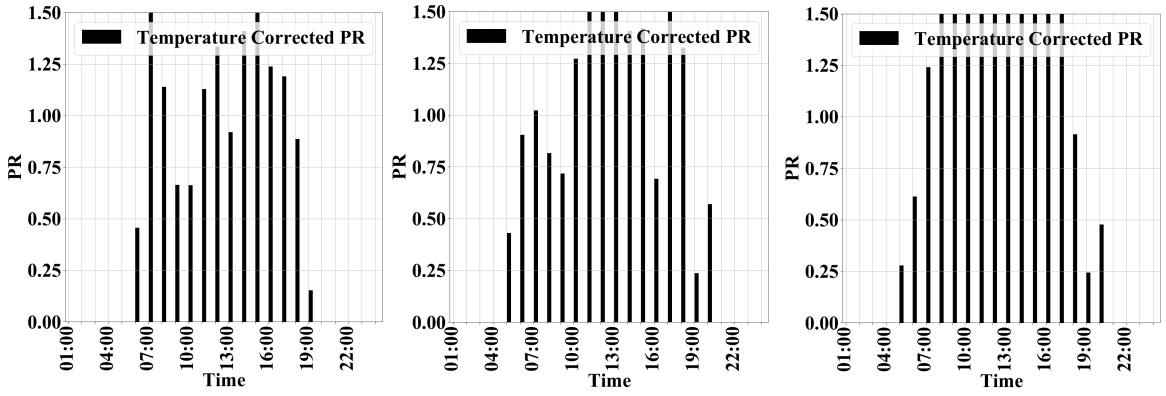

(a) *16.04.18* (b) *28.04.18* (c) *03.05.18*

Figure 4.20: *Plots of PR_{corr} of system 1 in three days in April and May showing the shortcomings of using GHI data from another location.*

A final source of uncertainty is the tilt and orientation of the systems. As shown in section 4.2, if the actual orientation is different than the given orientation, it will result in a change in estimated POA irradiance. An error in tilt will also alter the result, however not as much as the orientation. For example, if a system is oriented further west than given, the production during

late night will be larger than the estimated POA irradiance.

Finally, System 6 and 14 show a general very high performance throughout the year. This makes it difficult to compare with the other systems as it is likely that irradiance is being underestimated for the systems, or that the installed modules have a larger peak power than what used in the calculation.

4.3.1.1 Subsection summary and conclusion

The general result is that most systems have a temperature corrected performance ratio between 0.7 and 0.9 during the period from April to October. Outside this period, the performance is likely largely influenced by the local area (shadow, horizon, etc.) and whether the system owners keep removing the snow or not. As system 9 and 14 have shown, it is possible to maintain high performance during the year given a suitable location and by removing snow from the system. Additionally, as stated in section 4.2, the uncertainty added to the result by using GHI measurements increase in the winter. However, uncertainty is connected to the underestimation of POA irradiance using the Isotropic model. This cause the PR to be larger than the true PR_{corr}. Furthermore, the uncertainty of the pyranometers and inverter readings cause the uncertainty of the performance to be large.

4.3.2 Orientation dependent performance

The PR_{corr} for the period 22.08.18 to 30.03.19 was calculated for all systems. The result was put into Table 4.6 and illustrated in Figure 4.21. The system tilt is plotted along the r axis while the system orientation is plotted along the theta axis. This is to provide an overview of the orientation, tilt, and performance in the same graph.

The plot, together with the uncertainty of PR_{corr} estimations and the differences between PR_{corr} of the systems during the winter as discussed earlier, show that it is hard to conclude whether systems oriented to the east have a better performance compared to the systems oriented to the west. For example, the systems oriented between 150° and 160° (system 6 and 14) are indeed better performing compared to the systems oriented between 200° and 210° (system 3, 9, and 12). The systems oriented between 130° and 140° (system 11) are performing worse compared to the systems oriented between 220° and 230° (system 4 and 14).

Consequently, it is not possible to conclude that east oriented systems are better compared

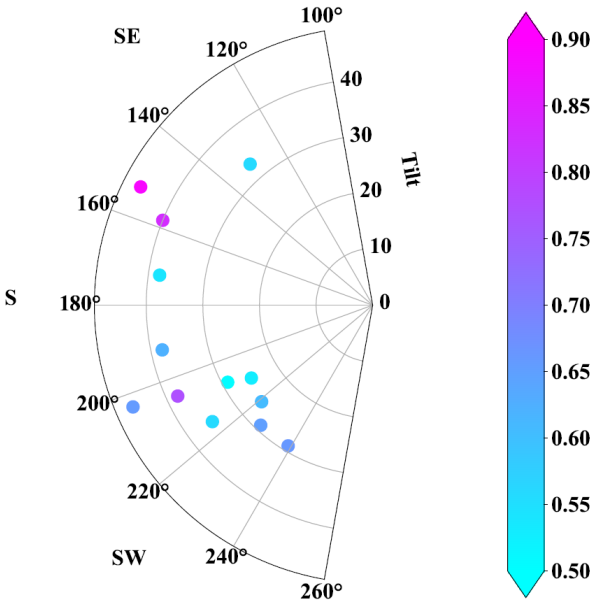

Figure 4.21: *A plot of the total temperature corrected performance ratio calculated by the Dirint/Isotropic model combination. The tilt of the system modules is along the r axis, and the system orientation is along the theta-axis. The data was collected in the time period from 22.08.2018 to 30.03.2019.*

to west oriented by comparing the total PR_{corr}. The total performance is too much affected by the winter months where the production is low explained by soiling (snow and frost), low solar elevation and intensity. Additionally, system 12 does not have recordings of the production in January and February 2019.

The monthly PR_{corr} was also calculated, and illustrated in Figure 4.22 and Table 4.6. Note that the r axis now represent the month, and that only non-zero PR_{corr} are plotted.

Compared to the systems oriented between 200° and 210° (system 3, 9, and 12), the systems oriented between 150° and 160° (system 14 and 6) are performing better every month until December, and February. Additionally, system 14 performs better than the west oriented systems in March. This indicates better performance of east faced systems, although system 6 and 14 is performing in general above 1, indicating that the irradiance estimation and temperature estimation are not equal to the irradiance at those locations. The system oriented between 130° and 140° (system 11) is performing better compared to the systems oriented between 220° and 230° (system 4 and 15) for all months until January. In January, February, and March are system 4 and 15 better which may be explained by snow. Although these observations argue for better performance of east fasted systems compared to west faced systems, it is not possible

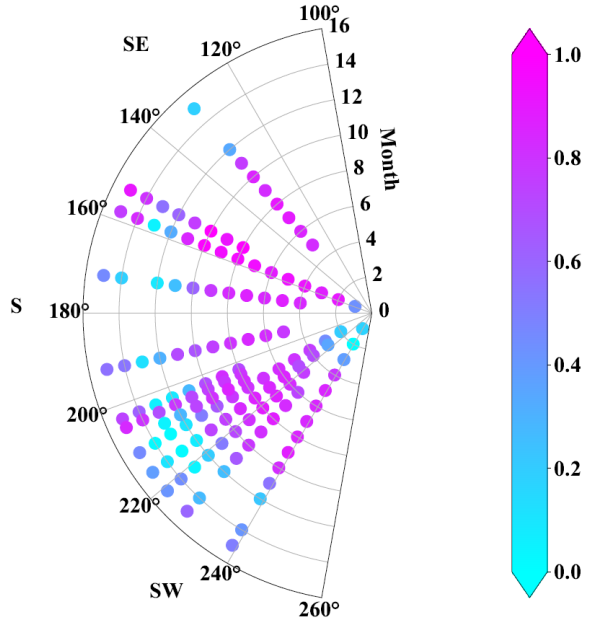

Figure 4.22: *A plot of the monthly temperature corrected performance ratio calculated by the Dirint/Isotropic model combination. The tilt of the system modules is along the r axis, and the system orientation is along the theta-axis. Only non-zero values are plotted. The data was collected in the time period from 22.08.2018 to 30.03.2019.*

to conclude as the performance differences are too small, inverter readings have an uncertainty of approximately 5%, and the pyranometer measurements have an uncertainty of 2%.

Furthermore, losses connected to shadowing and snow, especially during Spring, Autumn, and Winter, makes the comparison of systems difficult. Also, the uncertainty of the measurement equipment, cell temperature estimates, system orientation, system tilt, and POA irradiance estimates (that also got an uncertainty as the GHI measurements are collected from a location connected to it) makes the result even more uncertain.

The conclusion is therefore that it is neither possible to confirm nor deny the hypothesis of better system performance if the system is oriented to the east compared to the west.

4.3.3 Comparison of specific yield and performance ratio with other studies

As there are very few reports on temperature corrected performance ratio in Norway, the specific yield and performance ratio are compared with other studies. The Specific Yield and Performance Ratio of the systems studied in this thesis are shown in Table 4.7 and 4.8.

Imenes et al. studied a PV system oriented 200° with a 20° tilt installed on a flat roof in southern Norway[43]. The system contained 166 REC 225 W_p multi silicon (multi-Si) modules, 24 Elkem Solar 225 W_p multi-Si modules and 18 amorphous silicon modules from the Sharp NA-series. This system achieved a PR of 0.7 and 0.79 in 2013 and 2014, while the specific yield was 925 kWh/kW_p and 951 kWh/kW_p respectively.

Another study by Imenes reported performance of a system of poly-Si modules installed on a flat roof with a 10° tilt, and oriented east and west. The reported specific yield was approximately 810 kWh/kW_p and the *PR* was reported to be 0.86[44].

L. Tabita reported *PR* of 0.761 using wall mounted poly-Si modules and 0.859 using wall mounted Copper Indium Selenide (CIS) modules[45], while T. Haumann reported annual specific yields of 700 kWh/kW_p for near horizontal east and west oriented systems[46].

As not all systems have a full year of recordings, it is hard to compare the results. However, the performance ratio for system 1, 2, 5, and 7 is somewhat lower compared to these studies probably caused by low production during the winter months. On the other side, System 6 and 14 does have a very high performance ratio likely explained by different irradiance between Apelsvoll and the PV systems and an underestimation of the POA irradiance.

Table 4.7: *An overview of the total and monthly specific yield for the different systems. Note that Aug-Mar. means the total specific yield in that period, while total means for all months in operation.*

Month	1 [$\frac{kWh}{kW}$]	2 [$\frac{kWh}{kW}$]	3 [$\frac{kWh}{kW}$]	4 [$\frac{kWh}{kW}$]	5 [$\frac{kWh}{kW}$]	6 [$\frac{kWh}{kW}$]	7 [$\frac{kWh}{kW}$]	8 [$\frac{kWh}{kW}$]	9 [$\frac{kWh}{kW}$]	11 [$\frac{kWh}{kW}$]	12 [$\frac{kWh}{kW}$]	14 [$\frac{kWh}{kW}$]	15 [$\frac{kWh}{kW}$]
January	1.405	0	0	0	0	4.292	0	0	0	0	0	0	0
February	0.186	0	0	0	4.715	24.86	0	0	0	0	0	0	0
March	40.27	0	0	0	56.07	98.94	17.24	0	0	0	0	0	0
April	113.3	112.7	0	2.471	121.9	134.6	118.1	0	0	0	0	0	0
May	176.4	180.5	0	163.2	174.8	183.9	156.7	39.72	0	38.49	0	0	0
June	168.3	169.3	0	177.8	160.4	171.7	166.5	162.4	0	163.7	0	0	17.31
July	174.9	181.4	0	119.0	165.0	190.9	174.9	172.9	0	176.5	0	0	174.2
August	115.2	117.9	66.45	76.00	111.3	130.4	123.2	110.4	36.66	117.9	81.33	102.3	120.4
September	81.45	80.97	85.67	41.05	72.04	94.39	82.40	76.45	79.10	73.80	85.24	88.77	78.03
October	46.94	40.70	47.58	7.190	42.68	61.80	54.53	44.19	48.88	45.26	50.38	61.80	46.56
November	8.360	5.194	5.551	0.953	7.775	14.28	12.75	11.72	11.61	11.06	11.57	12.31	10.17
December	1.181	0.672	0.638	0.496	0.856	1.953	0.729	1.742	4.812	1.658	1.603	3.438	1.431
January	0	0	1.147	13.31	0.218	0.942	0.316	1.931	10.89	0.002	0.841	8.360	0
February	12.92	6.551	22.20	34.13	0.856	26.37	4.449	18.44	27.13	0.008	0	24.39	8.747
March	41.68	41.54	68.45	108.5	43.37	65.22	39.46	49.95	74.60	14.23	0	75.61	50.48
Aug.-Mar.	212.9	198.0	246.8	204.2	198.4	293.7	114.9	233.3	106.2	170.0	177.6	310.4	218.1
Total	982.5	937.4	297.7	679.8	962.0	1205	951.2	689.9	293.7	642.7	231.0	377.0	507.3

Table 4.8: *An overview of the total and monthly performance ratio (PR) for the systems.*

Month	1	2	3	4	5	6	7	8	9	11	12	14	15
January	0.191	0.000	0.000	0.000	0.000	0.479	0.000	0.000	0.000	0.000	0.000	0.000	0.000
February	0.000	0.000	0.000	0.000	0.216	1.000	0.000	0.000	0.000	0.000	0.000	0.000	0.000
March	0.415	0.000	0.000	0.000	0.485	0.948	0.382	0.000	0.000	0.000	0.000	0.000	0.000
April	0.831	0.780	0.000	0.000	0.803	0.974	0.746	0.000	0.000	0.000	0.000	0.000	0.000
May	0.858	0.876	0.000	0.825	0.807	0.935	0.707	0.840	0.000	0.890	0.000	0.000	0.000
June	0.845	0.842	0.000	0.826	0.831	0.886	0.859	0.826	0.000	0.858	0.000	0.000	0.803
July	0.829	0.848	0.000	0.851	0.793	0.926	0.832	0.826	0.000	0.877	0.000	0.000	0.816
August	0.881	0.857	0.746	0.913	0.830	0.983	0.890	0.824	0.859	0.932	0.867	1.041	0.903
September	0.929	0.816	0.858	0.857	0.827	0.997	0.883	0.787	0.825	0.869	0.903	0.968	0.861
October	0.894	0.653	0.746	0.776	0.711	1.063	0.815	0.725	0.809	0.928	0.874	1.091	0.849
November	0.604	0.276	0.300	0.567	0.560	0.929	0.811	0.774	0.790	0.838	0.802	0.838	0.714
December	0.244	0.095	0.095	0.220	0.116	0.361	0.080	0.340	0.870	0.373	0.319	0.674	0.282
January	0.000	0.000	0.065	0.042	0.015	0.052	0.019	0.133	0.765	0.000	0.055	0.614	0.000
February	0.451	0.204	0.677	0.486	0.024	0.919	0.113	0.593	0.876	0.000	0.000	0.885	0.293
March	0.549	0.496	0.795	0.451	0.049	0.820	0.412	0.602	0.905	0.198	0.000	0.985	0.649
Aug.-Mar.	0.724	0.592	0.718	0.665	0.579	0.909	0.611	0.681	0.846	0.611	0.551	0.974	0.711
Total	0.766	0.783	0.727	0.784	0.714	0.926	0.730	0.772	0.846	0.786	0.591	0.981	0.778

4.3.4 Section summary and conclusion

The general result is that most systems have a temperature corrected performance ratio between 0.7 and 0.9 during the period from April to October. Outside this period, the performance is likely largely influenced by the local area (shadow, horizon, etc.) and whether the system owners keep removing the snow or not. As the system 9 and 14 have shown, it is possible to maintain high performance during the year given a suitable location and by removing snow from the system.

The assessment of orientation dependent performance showed that during the summer period, the systems oriented to the east did have a larger estimated PR_{corr} compared to the systems oriented to the west. However, due to the large uncertainty of the inverter readings and the pyranometer measurement, it is no possible to conclude that the east oriented systems do have a better performance compared to west oriented systems.

4.4 Inverter performance

Finally, the loss connected to the inverter was assessed. This was done by estimating the inverter efficiency and plotted together with the yield. The efficiency was grouped by the power fraction of rated power, and the efficiency was calculated by taking the sum of AC- and DC power, and divided by each other (according to $\frac{P_{AC}}{P_{DC}}$). The same was repeated but now grouped by voltage fraction of maximum operating voltage. The result for system 1 and 2 is shown in Figure 4.23 (grouped by power) and 4.24 (grouped by voltage). All systems have similar characteristics, and all plots are found in appendix D.

Figure 4.23a shows that the inverters' efficiency curve has the expected shape. The low efficiency at the beginning of the curve is explained by a larger fraction of power consumed by the inverter, the higher power needed to control the switches at low power output[11], and losses connected to resistance of the cables. The efficiency curve shows an efficiency of 0% when reaching 95% of rated power. This is explained by the inverter never invert that high power, and therefore it is wrong. Additionally, the efficiency decreases slightly from 40% of rated power. This may be explained by the mppt missing the rated power, a larger current producing more heat, or losses connected to the converter that increase with the power fraction[11].

Looking at the same figure, it is clear that the inverters never operate on rated power (3000

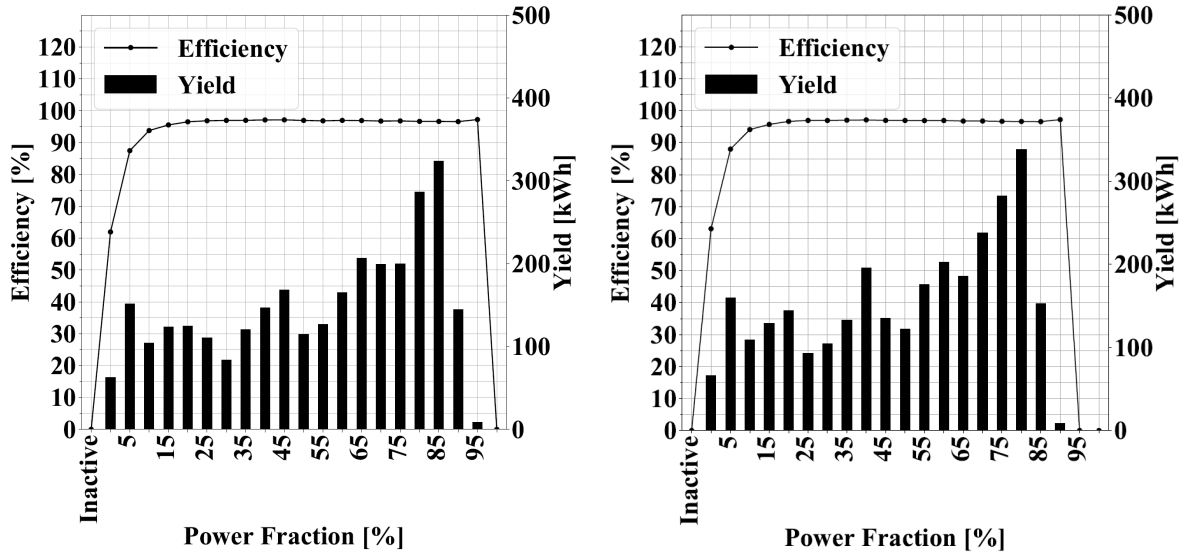

(a) *System 1* (b) *System 2*

Figure 4.23: *Plots of the efficiency curve together with the yield (bars) for system 1 and 2 grouped by power fraction* ($\frac{P}{P_{rated}}$)

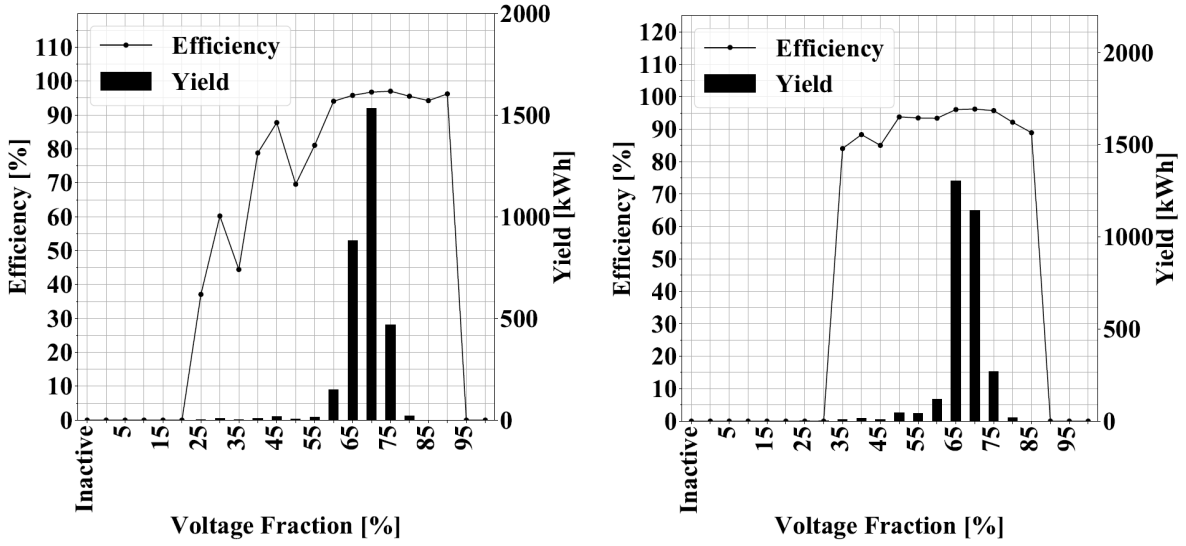

(a) *System 1* (b) *System 2*

Figure 4.24: *Plots of the efficiency curve together with the yield (bars) for system 1 and 2 grouped by voltage fraction* ($\frac{V}{V_{op,max}}$)

W) even though system peak power is 3180 W. This may be explained by lower irradiance, as system 2 (Figure 4.23b) is oriented to the south. The number of modules can also be increased to utilise the inverter. However, there are safety hazards connected to that. If the current or voltage becomes too high, there may be generating to much heat that can cause a fire. In this

study, all systems with StecaGrid 3010 inverter, except system 7, has 12 PV modules connected to it. This corresponds to a total of 463.2 V in open circuit conditions, which is within the operating voltage range. As most systems reach around 80 of the maximum rated voltage, it is possible to increase the number of modules and still be within the operation voltage range. However, this may not be done as the systems are installed on private homes.

By looking at Figure 4.23b, the efficiency is above 96% where most of the yield is produced. This indicates that the mppt is able to hold the production close to optimal conditions most of the time.

To assess how the voltage and power affect the inverter efficiency, the efficiency and yield for each string for system 7 and 9 were calculated and plotted. The result is shown in Figure 4.25 (grouped by voltage) and 4.26 (grouped by power). As seen in Figure 4.26b, the string

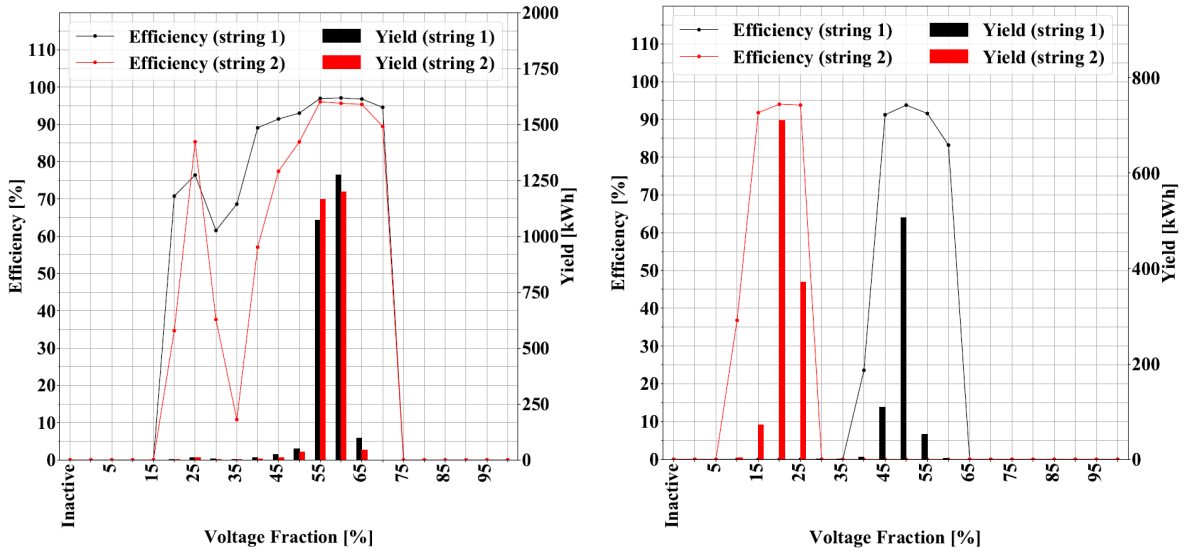

(a) *System 7* (b) *System 9*

Figure 4.25: *Plots of the efficiency curve together with the yield for string 1 (blue) and string 2 (red) dependent on voltage for System 7 (Figure 4.25a) and System 9 (Figure 4.25b).*

2 has a higher efficiency compared to string 1 where the power fraction is low, and string 1 has a higher efficiency compared to string 2 when the power fraction is larger, as expected[47]. Figure 4.26a shows the efficiency curve of house 7 that has two identical PV systems. Although equal systems, the inverters perform differently. This may be explained by the measurement uncertainty of 5%, by different temperatures of the inverter, or by the voltage of the different strings, as shown in the data sheet[36].

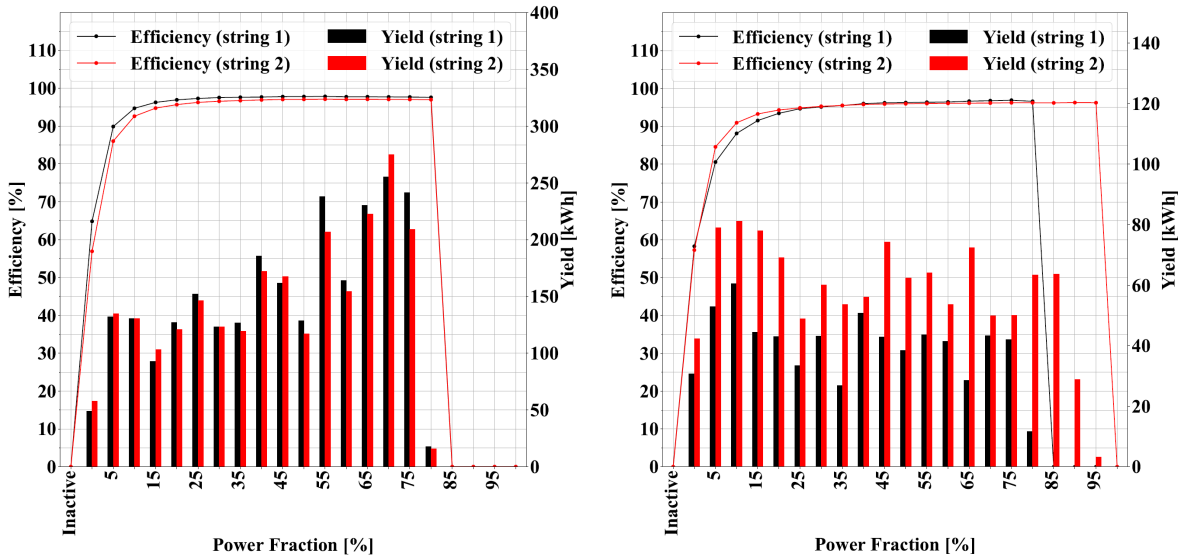

(a) *System 7* (b) *System 9*

Figure 4.26: *Plots of the efficiency curve together with the yield for string 1 (blue) and string 2 (red) dependent on power for System 7 (Figure 4.26a) and system 9 (Figure 4.26b).*

Another way of assessing the effect of the number of modules connected to the inverter is to look at the systems with different string configurations. Here, system 1-6, 8, and 11-15 have 12 modules connected to a StecaGrid 3010 which can be compared to the strings of system 7 which has two strings of 10 modules each connected to a StecaGrid 3010. The power dependent efficiency of the different systems did not show any difference in efficiency. String 2 of system 7 has the lowest efficiency until 50% power fraction. As the efficiency of equal systems varies between 1% and 2%, it is not possible to say that the difference is due to the number of modules. The difference may be explained by inverter temperature, current, or differences in power consumption, and mppt.

4.4.1 Inverter test

As detailed measurement from the AC side of the inverter was not available, the specific yield was calculated, and the result is put into Table 4.9. It shows that string 1 has a 0.051 kWh/kW$_p$ better specific yield compared to string 2. The measurements are made before the inverter, the result is therefore corresponding to cable loss, mppt efficiency, and differences between individual PV modules. Assuming perfectly equal modules (i.e. equal current), the cable losses of string 2 will be lower as the voltage is small. Additionally, the total length of the cable used

Table 4.9: *An overview of the total and monthly specific yield for the different systems.*

String	W_p [kW]	Y [kWh]	y [kWh/kW$_p$]
1	3.975	61.514	15.476
2	1.590	24.509	15.415
total (DC)	5565	68.024	15.458
total (AC)	5565	85.740	15.407

in string 1 is longer resulting to a higher loss compared to string 2. The mppt also affect the result, as the mppt find a common mpp for both strings. This result shows a larger specific yield provided by string 1 compared to string 2. This can be explained by a larger fraction of the total DC power comes from string 1 resulting in a larger influence on the mpp compared to string 2.

That being said, the result differs by less than 5%. Thus, it is not possible to conclude because the inverter readings have an uncertainty of 5%.

4.4.2 Subsection summary and conclusion

To summarise, all inverters have an inefficiency of < 5% where the majority of the yield is produced. The efficiency drops when the power fraction is lower explained by a larger fraction of energy is needed to control the inverter. The voltage-dependent efficiency curve shows that the inverter operates in a narrow voltage range indicating the mppt to work as stated in the data sheet. The efficiency is also here >95% where the majority of the yield is produced.

The test of the inverted did show a larger specific yield of string 1 (15 modules) compared to string 2 (six modules). However, the uncertainty of the readings is larger than the relative difference between the strings that makes it not possible to conclude.

5 Conclusion

Based on the evaluation of irradiance models in the period December to March, the Dirint/Isotropic model combination got the lowest *RMSE* with a value of 24.48 W/m^2 compared to 27.28 W/m^2 for the Disc/Isotropic model combination, and 28.04 W/m^2 for the Dirint/Perez model. The difference is not large, thus not possible to state that the performance is truly better compared to the other models. However, the lower *RMSE* value of the Isotropic sky model may be connected to the low irradiance in Norway, especially during the winter period, that is suitable for the Isotropic model. The Dirint decomposition model had the best performance that may be explained by the larger data set used to determine the empirical coefficients.

The study has also shown that it is possible to use irradiance data collected from other areas. However, it is important to note that the uncertainty increase towards winter, and that the local environment and climate impact the result.

Although large uncertainty, the PR_{corr} is above 0.8 for most systems in large periods of the year. The total PR is however greatly reduced due to the low production during the winter months (there is available irradiance but close to zero production). *PR* was also shown to be in the same range of performance ratios reported by other assessments.

Due to the large measurement uncertainty of the inverters and the pyranometers, and the environmental differences between PV and pyranometer locations, it is not possible to conclude whether the performance is different between systems oriented east compared to the west, or not. The comparison of total PR_{corr} did not show any evidence of better performance for east faced systems compared to the west. This is explained by the large impact of the low production on the performance during the winter months. However, comparing monthly values during the summer period showed higher PR_{corr} of systems oriented to the east compared to systems in the west.

The inverter study confirmed that the inverter performance corresponds to the performance

characteristics given by the producer, and the inverter performance was predominantly above 95%. The inverter test shows a better specific yield of the largest inverter string. Although the difference in specific yield, it is not possible to confirm the hypothesis as the inverter reading uncertainty is too high.

6 Further work

- Evaluation of irradiance models over an entire year to ensure which model that has best performance
- Perform an inverter experiment with readings readings of AC side for different strings
- Perform an experiment where the the orientation dependence is accuratly measures

Reference

[1] C. D. Keeling et al. “Atmospheric CO2 and 13CO2 Exchange with the Terrestrial Biosphere and Oceans from 1978 to 2000: Observations and Carbon Cycle Implications”. In: *A History of Atmospheric CO2 and Its Effects on Plants, Animals, and Ecosystems*. Ed. by I.T. Baldwin et al. New York, NY: Springer New York, 2005, pp. 83–113. ISBN: 978-0-387-27048-7. DOI: 10.1007/0-387-27048-5_5. URL: https://doi.org/10.1007/0-387-27048-5_5.

[2] J. Cook et al. “Quantifying the consensus on anthropogenic global warming in the scientific literature”. In: *Environmental Research Letters* 8.2 (2013), p. 024024. URL: http://stacks.iop.org/1748-9326/8/i=2/a=024024.

[3] 2014 IPCC. *Climate Change 2014: Synthesis Report. Contribution of Working Groups I, II and III to the Fifth Assessment Report of the Intergovernmental Panel on Climate Change*. IPPC, Geneve, Switzerland, 2014, p. 151.

[4] United nations. *Adoption of the Paris agreement*. Paris, France, 2015.

[5] Enerdata. *Global Energy Trends, 2018 edition. A step backward for the energy transition?* Accessed: 25.01.2019. 2018. URL: https://www.enerdata.net/publications/reports-presentations/2018-world-energy-trends-projections.html.

[6] 2014 IPPC. “Climate Change 2014: Mitigation of Climate Change. Contribution of Working Group III to the Fifth Assessment Report of the Intergovernmental Panel on Climate Change[Edenhofer, O., R. Pichs-Madruga, Y. Sokona, E. Farahani, S. Kadner, K. Seyboth, A. Adler, I. Baum, S. Brunner, P. Eickemeier, B. Kriemann, J. Savolainen, S. Schlömer, C. von Stechow, T. Zwickel and J.C. Minx (eds.)]” In: ().

[7] G. Masson, I. Kaizuka, and C. Cambiè. “A Snapshot of Global PV”. In: (2018).

[8] IEA PVPS. *National Survey Report of PV Power Applications in Norway 2016*. Accessed 25.01.2019. 2016. URL: http://iea-pvps.org/index.php?id=93&eID=dam_frontend_push&docID=4216.

[9] S. A. Muyiwa and E.T. Vågnes. "Preliminary assessment of a small-scale rooftop PV-grid tied in Norwegian climatic conditions". In: *Energy Conversion and Management* 90 (2015), pp. 458 –465. ISSN: 0196-8904. DOI: https://doi.org/10.1016/j.enconman.2014.11.028. URL: http://www.sciencedirect.com/science/article/pii/S0196890414009856.

[10] A. G. Imenes et al. "Performance of grid-connected PV system in Southern Norway". In: *2015 IEEE 42nd Photovoltaic Specialist Conference (PVSC)*. 2015, pp. 1–6. DOI: 10.1109/PVSC.2015.7355823.

[11] A. Smets et al. *Solar energy: the physics and engineering of photovoltaic conversion, technologies and systems*. UIT Cambridge, 2016.

[12] Peter Wurfel and Uli Wurfel. *Physics of solar cells: from basic principles to advanced concepts*. Wiley-VCH Verlag GmbH Co. KGaA, 2016.

[13] *PVEducation*. Accessed 10.03.2019. URL: https://pveducation.org/.

[14] F. Kasten and A. T. Young. "Revised optical air mass tables and approximation formula". In: *Appl. Opt.* 28.22 (1989), pp. 4735–4738. DOI: 10.1364/AO.28.004735. URL: http://ao.osa.org/abstract.cfm?URI=ao-28-22-4735.

[15] Robert A. Rohde. Accessed: 26.01.2019. URL: https://commons.wikimedia.org/wiki/File:Solar_Spectrum.png.

[16] M. Lave et al. "Evaluation of Global Horizontal Irradiance to Plane-of-Array Irradiance Models at Locations Across the United States". In: *IEEE Journal of Photovoltaics* 5.2 (2015), 597–606. DOI: 10.1109/jphotov.2015.2392938.

[17] I. Reda and A. Andreas. "Solar Position Algorithm for Solar Radiation Applications". In: *Solar Energy* 76.5 (2004), pp. 577–589.

[18] J. H. Meeus. *Astronomical Algorithms*. Willmann-Bell, Incorporated, 1991. ISBN: 0943396352.

[19] D.G. Erbs, S.A. Klein, and J.A. Duffie. “Estimation of the diffuse radiation fraction for hourly, daily and monthly-average global radiation”. In: *Solar Energy* 28.4 (1982), pp. 293 –302. ISSN: 0038-092X. DOI: https://doi.org/10.1016/0038-092X(82)90302-4. URL: http://www.sciencedirect.com/science/article/pii/0038092X82903024.

[20] J.F. Orgill and K.G.T. Hollands. “Correlation equation for hourly diffuse radiation on a horizontal surface”. In: *Solar Energy* 19.4 (1977), pp. 357 –359. ISSN: 0038-092X. DOI: https://doi.org/10.1016/0038-092X(77)90006-8. URL: http://www.sciencedirect.com/science/article/pii/0038092X77900068.

[21] R.R. Perez et al. “Dynamic global-to-direct irradiance conversion models”. In: *ASHRAE Transactions* 98 (Jan. 1992), pp. 354–369.

[22] H. C. Hottel and B. B. Woertz. “Evaluation of flat-plate solar heat collector”. In: *Transactions of the ASME* 64 (1942).

[23] Davies J.A. Hay J.E., ed. *Calculations of the solar radiation incident on an inclined surface*. Proc. of First Canadian Solar Radiation Data Workshop, 59. Ministry of Supply and Services, Canada.

[24] P.G. Loutzenhiser et al. “Empirical validation of models to compute solar irradiance on inclined surfaces for building energy simulation”. In: *Solar Energy* 81.2 (2007), pp. 254 –267. ISSN: 0038-092X. DOI: https://doi.org/10.1016/j.solener.2006.03.009. URL: http://www.sciencedirect.com/science/article/pii/S0038092X06000879.

[25] R. Perez et al. “Modeling daylight availability and irradiance components from direct and global irradiance”. In: *Solar Energy* 44.5 (1990), pp. 271 –289. ISSN: 0038-092X. DOI: https://doi.org/10.1016/0038-092X(90)90055-H. URL: http://www.sciencedirect.com/science/article/pii/0038092X9090055H.

[26] Matthew J. Reno and Clifford W. Hansen. “Identification of periods of clear sky irradiance in time series of GHI measurements”. In: *Renewable Energy* 90 (2016), 520–531. DOI: 10.1016/j.renene.2015.12.031.

[27] P. Ineichen and R. Perez. “A new airmass independent formulation for the Linke turbidity coefficient”. In: *Solar Energy* 73.3 (2002), 151–157. DOI: 10.1016/s0038-092x(02)00045-2.

[28] Richard Perez et al. “A new operational model for satellite-derived irradiances: description and validation”. In: *Solar Energy* 73.5 (2002), pp. 307 –317. ISSN: 0038-092X. DOI: https://doi.org/10.1016/S0038-092X(02)00122-6. URL: http://www.sciencedirect.com/science/article/pii/S0038092X02001226.

[29] Joshua Stein. *PV Performance Modeling Methods and Practices: Results from the 4th PV Performance Modeling Collaborative Workshop*. 2017. DOI: 10.2172/1347082.

[30] T. Dierauf et al. “Weather-Corrected Performance Ratio”. In: (2013). DOI: 10.2172/1078057.

[31] D L King, J A Kratochvil, and W E Boyson. “Photovoltaic Array Performance Model”. PhD thesis. Jan. 2004. DOI: 10.2172/919131.

[32] *MET Norway*. Accessed 29.01.2019. URL: http://sharki.oslo.dnmi.no/portal/page?_pageid=73,39035,73_39049&_dad=portal&_schema=PORTAL.

[33] *Instruction Manual*. Accessed: 08.05.2019. Kigg & Zonen. Oct. 2016.

[34] *Kipp Zonen Pyranometers, is an 11 better than a 10? You decide*. Accessed 08.05.2019. URL: https://www.kippzonen.com/News/855/Kipp-Zonen-Pyranometers-is-an-11-better-than-a-10-You-decide#.XNLgD6SxX1s.

[35] *IBC PolySol 260 CS4, 265 CS4*. Accessed: 09.04.2019. IBC SOLAR AG. Feb. 2016.

[36] *coolcept StecaGrid 1500, StecaGrid 2000, StecaGrid 2500, StecaGrid 3010, StecaGrid 3600, StecaGrid 4200*. Accessed: 09.04.2019. Steca Elektronik GmbH. Jan. 2018.

[37] *Fronius Galvo Light*. Accessed: 09.04.2019. IBC SOLAR AG. Sept. 2013.

[38] *Fronius Primo*. Accessed: 09.04.2019. Fronius International GmbH. Sept. 2015.

[39] M. Richter et al. “Best Practice Guide On Uncertainty in PV Modelling”. In: (2015).

[40] W. F. Holmgren, C. W. Hansen, and M. A. Mikofski. “pvlib python: a python package for modeling solar energy systems.” In: 3(29).884 (2019). DOI: 10.5281/zenodo.2227214.

[41] PVsyst. Accessed: 6.05.2019. URL: http://files.pvsyst.com/help/albedo.htm.

[42] A. G. Imenes. “Performance of zero energy homes in smart village skarpnes”. In: *2016 IEEE 43rd Photovoltaic Specialists Conference (PVSC)*. 2016, pp. 3153–3158. DOI: 10.1109/PVSC.2016.7750247.

[43] A. G. Imenes et al. “Performance of grid-connected PV system in Southern Norway”. In: *2015 IEEE 42nd Photovoltaic Specialist Conference (PVSC)*. 2015, pp. 1–6. DOI: 10.1109/PVSC.2015.7355823.

[44] A. G. Imenes. “Performance of BIPV and BAPV installations in Norway”. In: June 2016, pp. 3147–3152. DOI: 10.1109/PVSC.2016.7750246.

[45] L. Tabita. “A Study of the performance of two wall attached PV systems in a Nordic climate”. MA thesis. 2018.

[46] T Haumann. “A Bried Look at the Performance of PV in Norway”. MA thesis. 2016.

[47] N.M. Pearsall. “1 - Introduction to photovoltaic system performance”. In: *The Performance of Photovoltaic (PV) Systems*. Ed. by Nicola Pearsall. Woodhead Publishing, 2017, pp. 1 –19. ISBN: 978-1-78242-336-2. DOI: https://doi.org/10.1016/B978-1-78242-336-2.00001-X. URL: http://www.sciencedirect.com/science/article/pii/B97817824233620001X.

A Hourly measured and estimated POA irradiance

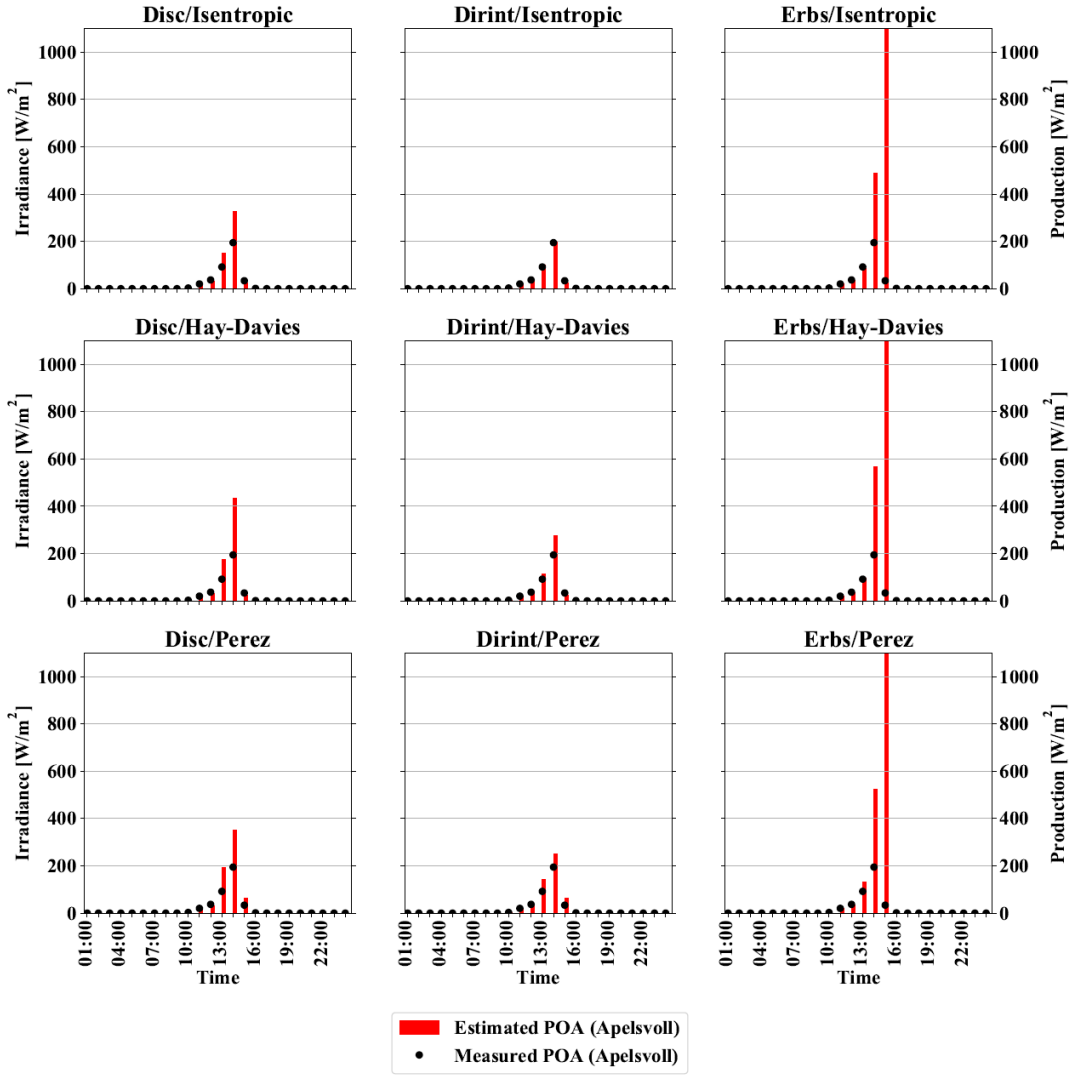

Figure A.1: *Plots of nine different model combinations together with the measured in-plane irradiance of 04.12.18. It shows that models using Erbs tend to overestimate low irradiance. Along the first axis is time, estimated in-plane irradiance per square meter is along the second axis, while the production per square meter (black dot) is along the third axis.*

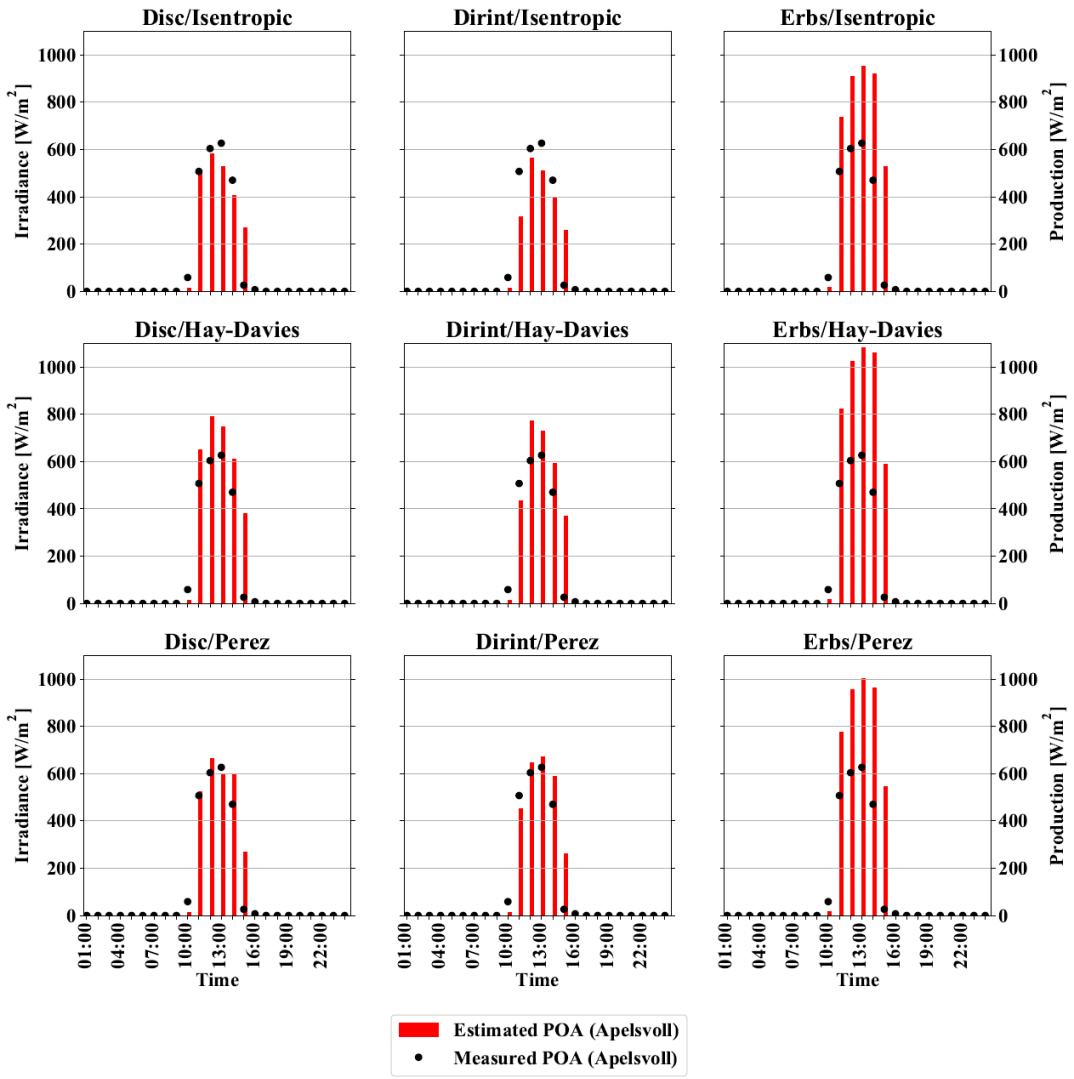

Figure A.2: *Plots of nine different model combinations together with the measured in-plane irradiance of 19.01.19. It shows that models using Erbs tend to overestimate low irradiance. Along the first axis is time, estimated in-plane irradiance per square meter is along the second axis, while the production per square meter (black dot) is along the third axis.*

B Shadow detection

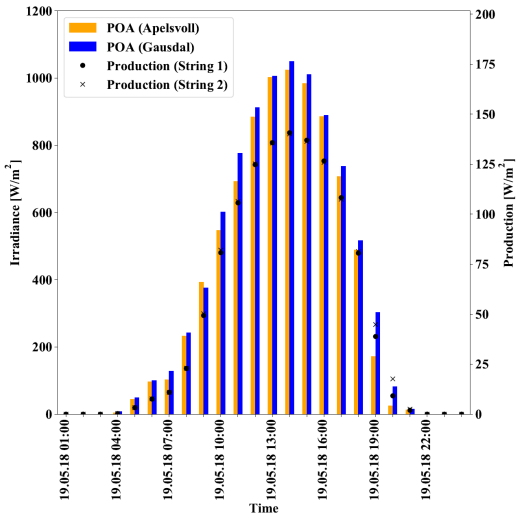

(a) *19.05.2018*

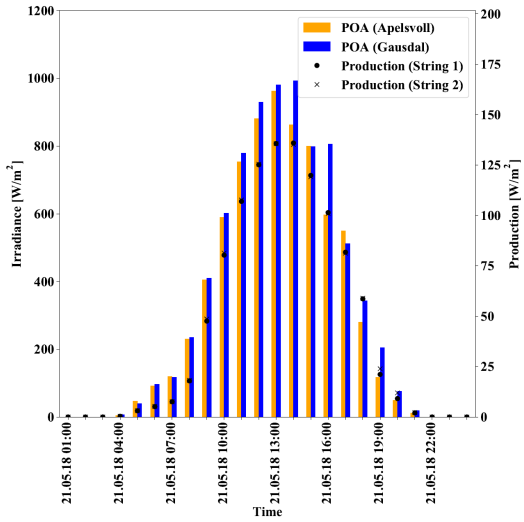

(b) *21.05.2018*

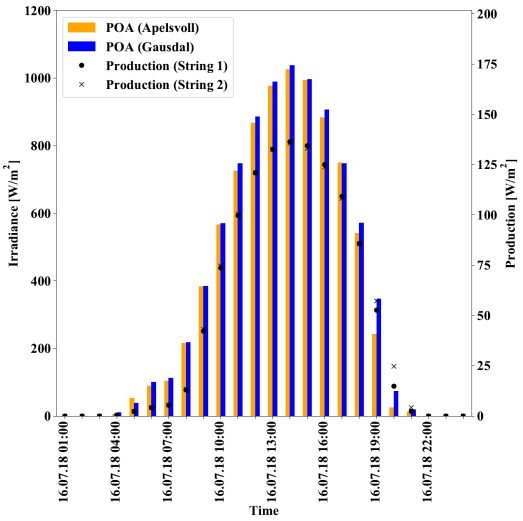

(c) *16.07.2018*

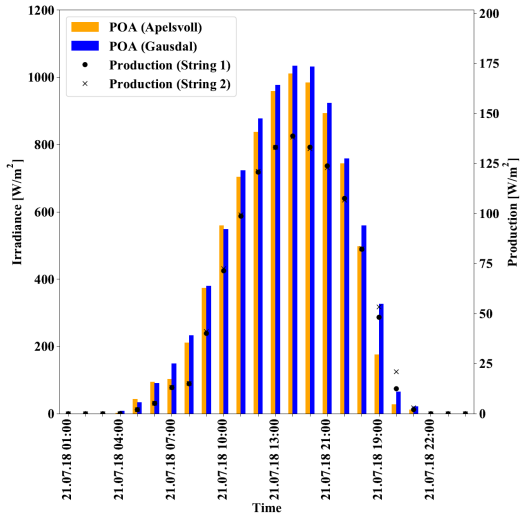

(d) *21.07.2018*

Figure B.1: The figures show a selection of plots of clear days that shows that the production of string 2 is larger in the evening compared to string 1. The rest of the day the production is similar.

C Thermal images of the systems

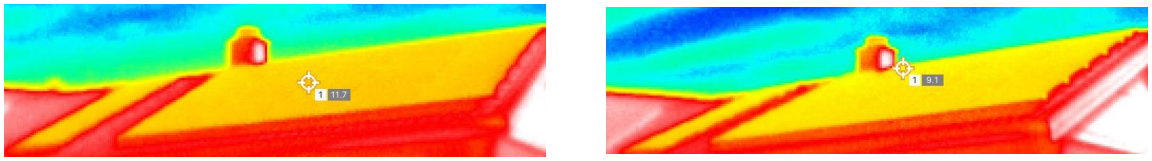

Figure C.1: *Two thermal images of system 1, taken from different angles, indicating a constant temperature over the entire system. The temperature scale is different in these images as there were difficulties finding a suitable scale. Note that the absolute temperatures shown in the images is wrong as temperature and emissivity references were not possible to set.*

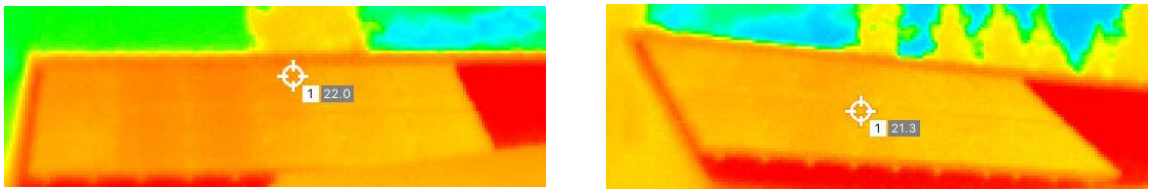

Figure C.2: *Two thermal images of system 2, taken from different angles, indicating a constant temperature over the entire system. Note that the absolute temperatures shown in the images is wrong as temperature and emissivity references were not possible to set.*

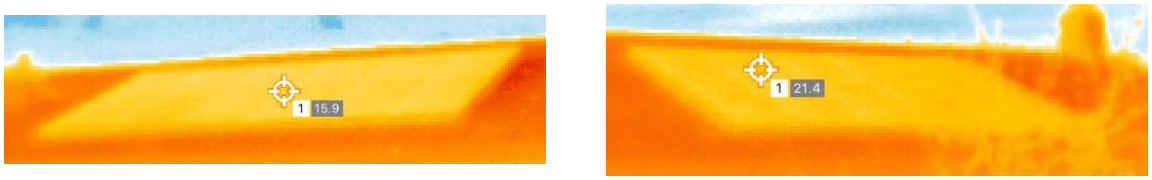

Figure C.3: *Two thermal images of system 4, taken from different angles, indicating a constant temperature over the entire system. There is a tree in to the right in image to the right. Note that the absolute temperatures shown in the images is wrong as temperature and emissivity references were not possible to set.*

Figure C.4: *Two thermal images of system 5, taken from different angles, indicating a constant temperature over the entire system. Note that the absolute temperatures shown in the images is wrong as temperature and emissivity references were not possible to set.*

Figure C.5: *Two thermal images of system 6, taken from different angles, indicating a constant temperature over the entire system. Note that the absolute temperatures shown in the images is wrong as temperature and emissivity references were not possible to set.*

Figure C.6: *Two thermal images of system 7, taken from different angles. The system was hard to get good images of, thus it is hard to say if the system has damages or not. Note that the absolute temperatures shown in the images is wrong as temperature and emissivity references were not possible to set.*

Figure C.7: *Two thermal images of system 8, taken from different angles, indicating a constant temperature over the entire system.Note that the absolute temperatures shown in the images is wrong as temperature and emissivity references were not possible to set.*

Figure C.8: *Two thermal images of system 9, taken from different angles, indicating a constant temperature over the entire system. Note that the absolute temperatures shown in the images is wrong as temperature and emissivity references were not possible to set.*

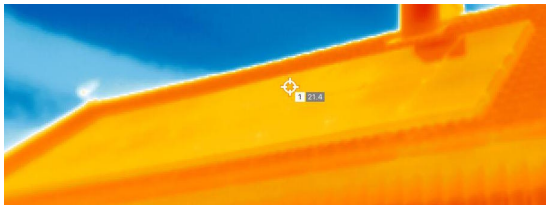

Figure C.9: *Two thermal images of system 14, taken from different angles, indicating a constant temperature over the entire system. Note that the absolute temperatures shown in the images is wrong as temperature and emissivity references were not possible to set.*

D Inverter efficiency graphs

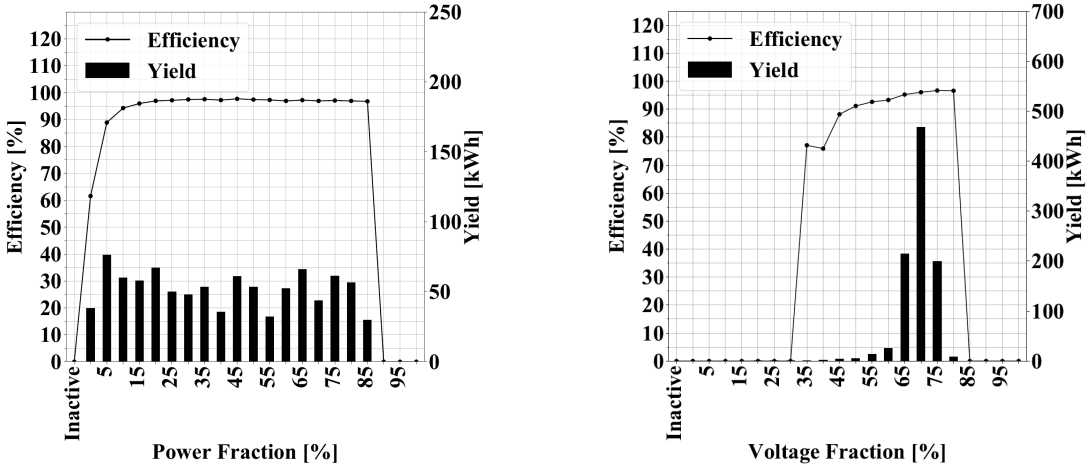

Figure D.1: *Plots of the efficiency curve together with the yield (bars) for system 3 grouped by power fraction voltage fraction ($\frac{P}{P_{rated}}$) and voltage fraction ($\frac{V}{V_{max,op}}$)*

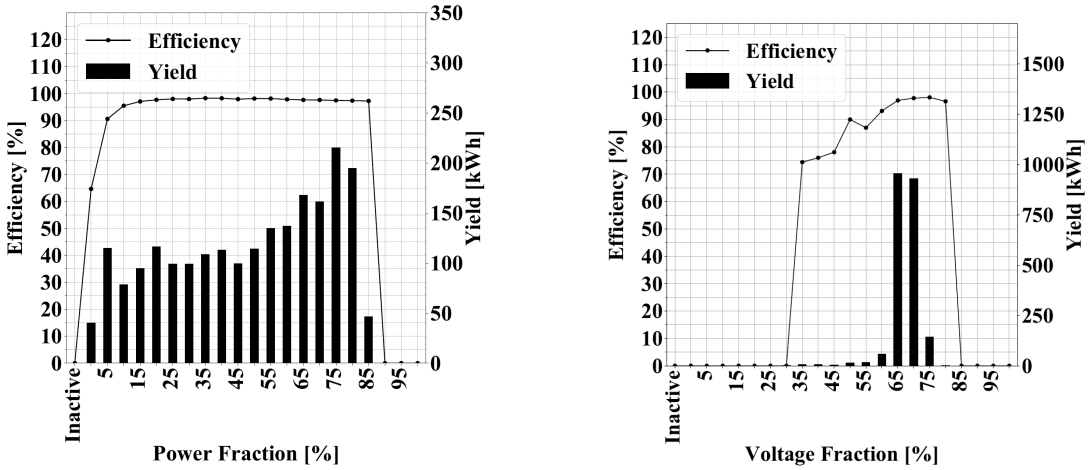

Figure D.2: *Plots of the efficiency curve together with the yield (bars) for system 4 grouped by power fraction voltage fraction ($\frac{P}{P_{rated}}$) and voltage fraction ($\frac{V}{V_{max,op}}$)*

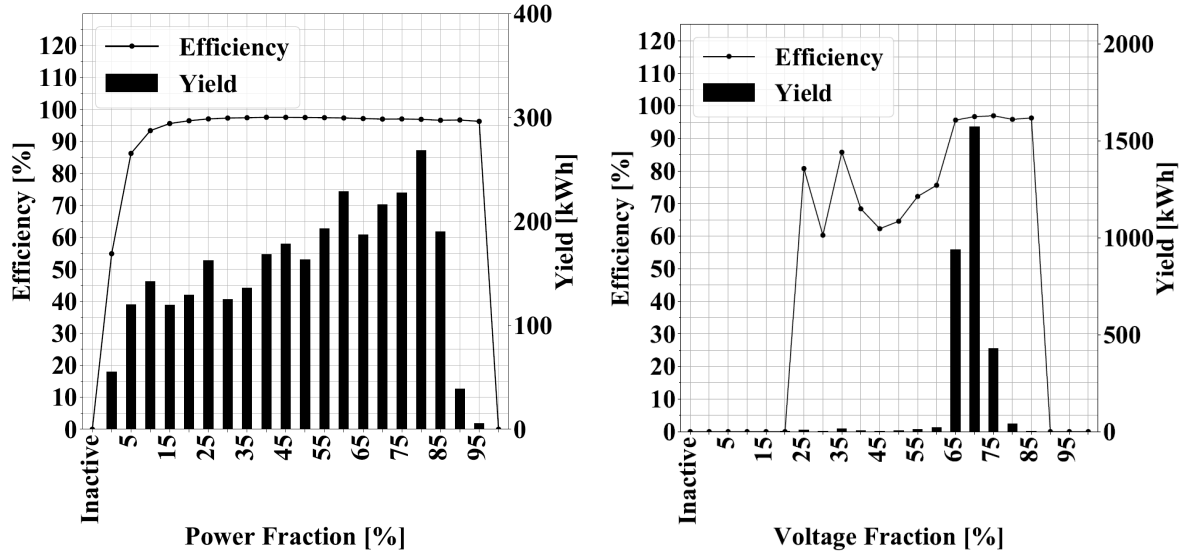

Figure D.3: *Plots of the efficiency curve together with the yield (bars) for system 5 grouped by power fraction voltage fraction ($\frac{P}{P_{rated}}$) and voltage fraction ($\frac{V}{V_{max,op}}$)*

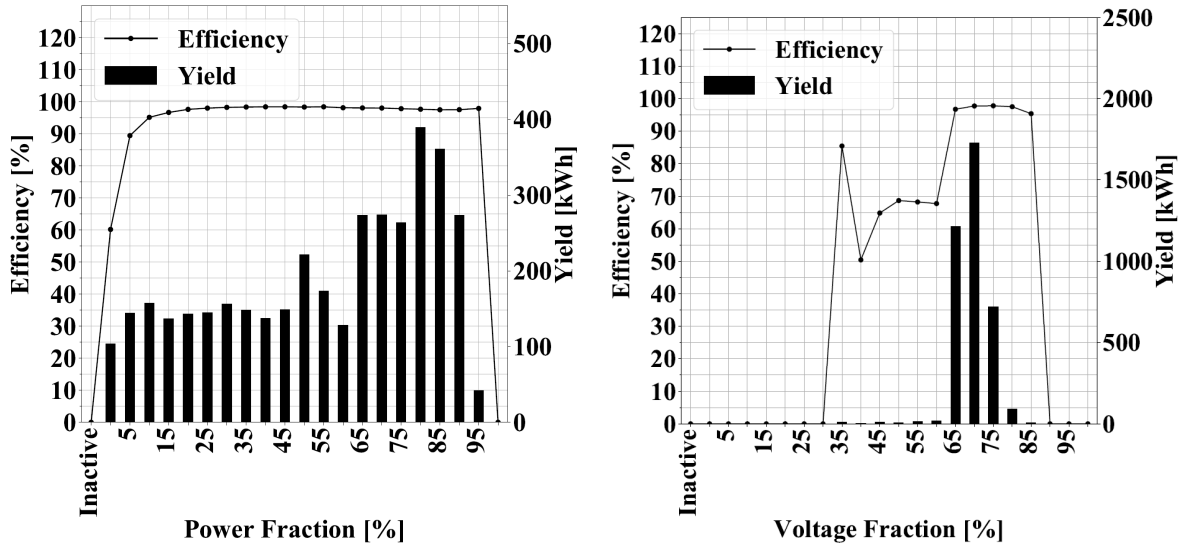

Figure D.4: *Plots of the efficiency curve together with the yield (bars) for system 6 grouped by power fraction voltage fraction ($\frac{P}{P_{rated}}$) and voltage fraction ($\frac{V}{V_{max,op}}$)*

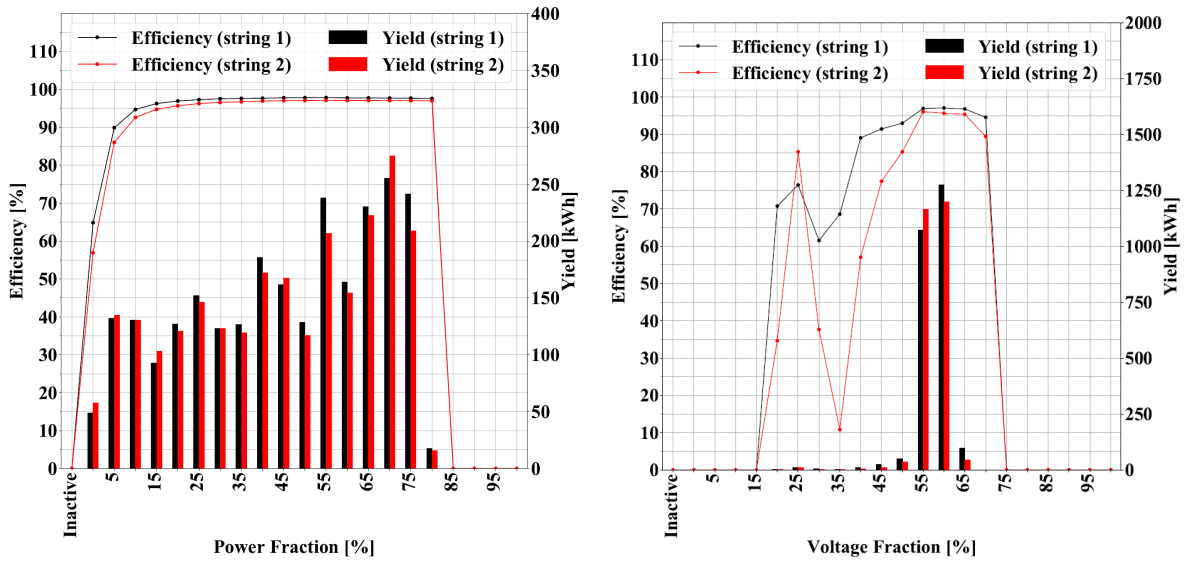

Figure D.5: *Plots of the efficiency curve together with the yield (bars) for system 7 grouped by power fraction voltage fraction ($\frac{P}{P_{rated}}$) and voltage fraction ($\frac{V}{V_{max,op}}$)*

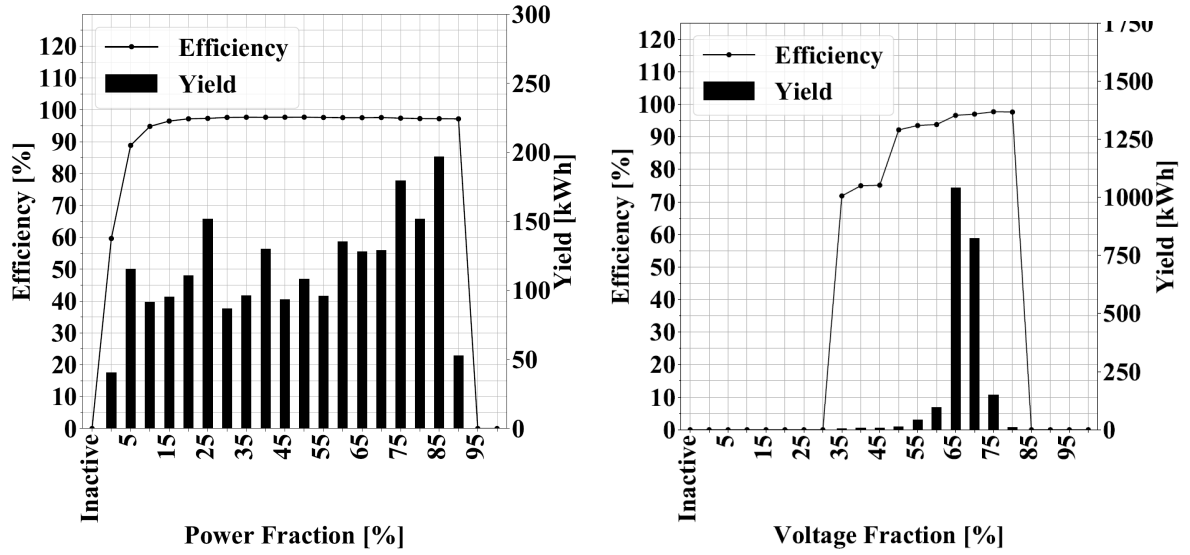

Figure D.6: *Plots of the efficiency curve together with the yield (bars) for system 8 grouped by power fraction voltage fraction ($\frac{P}{P_{rated}}$) and voltage fraction ($\frac{V}{V_{max,op}}$)*

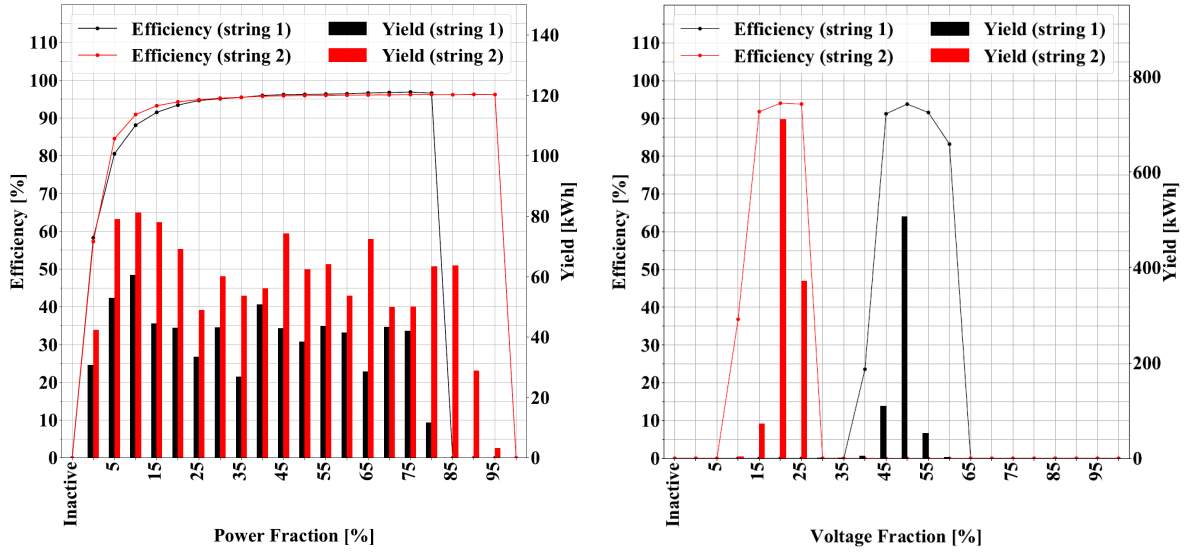

Figure D.7: *Plots of the efficiency curve together with the yield (bars) for system 9 grouped by power fraction voltage fraction ($\frac{P}{P_{rated}}$) and voltage fraction ($\frac{V}{V_{max,op}}$)*

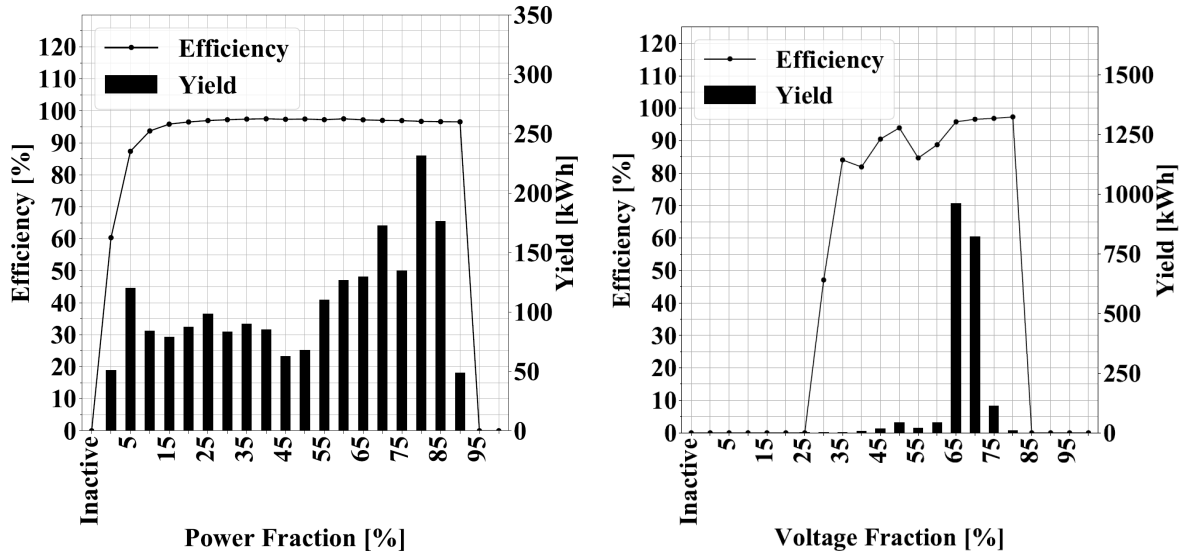

Figure D.8: *Plots of the efficiency curve together with the yield (bars) for system 11 grouped by power fraction voltage fraction ($\frac{P}{P_{rated}}$) and voltage fraction ($\frac{V}{V_{max,op}}$)*

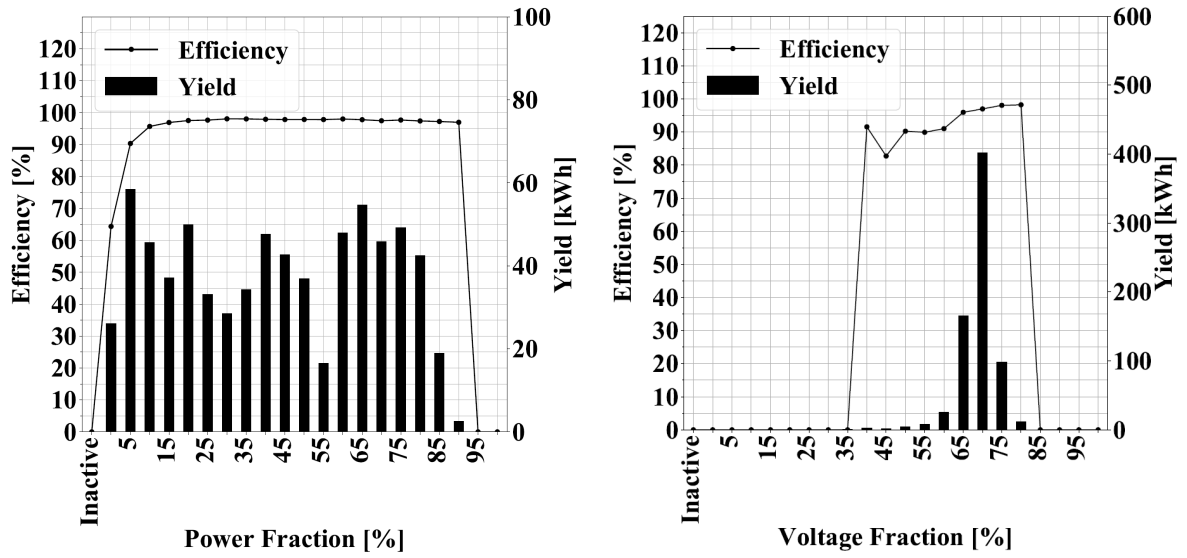

Figure D.9: *Plots of the efficiency curve together with the yield (bars) for system 12 grouped by power fraction voltage fraction ($\frac{P}{P_{rated}}$) and voltage fraction ($\frac{V}{V_{max,op}}$)*

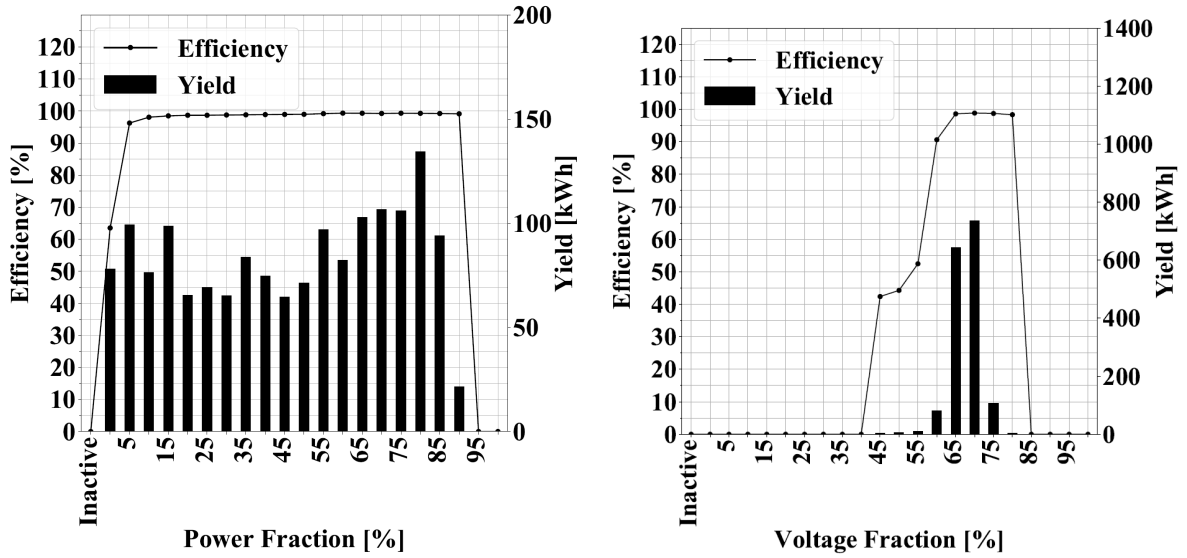

Figure D.10: *Plots of the efficiency curve together with the yield (bars) for system 14 grouped by power fraction voltage fraction ($\frac{P}{P_{rated}}$) and voltage fraction ($\frac{V}{V_{max,op}}$)*

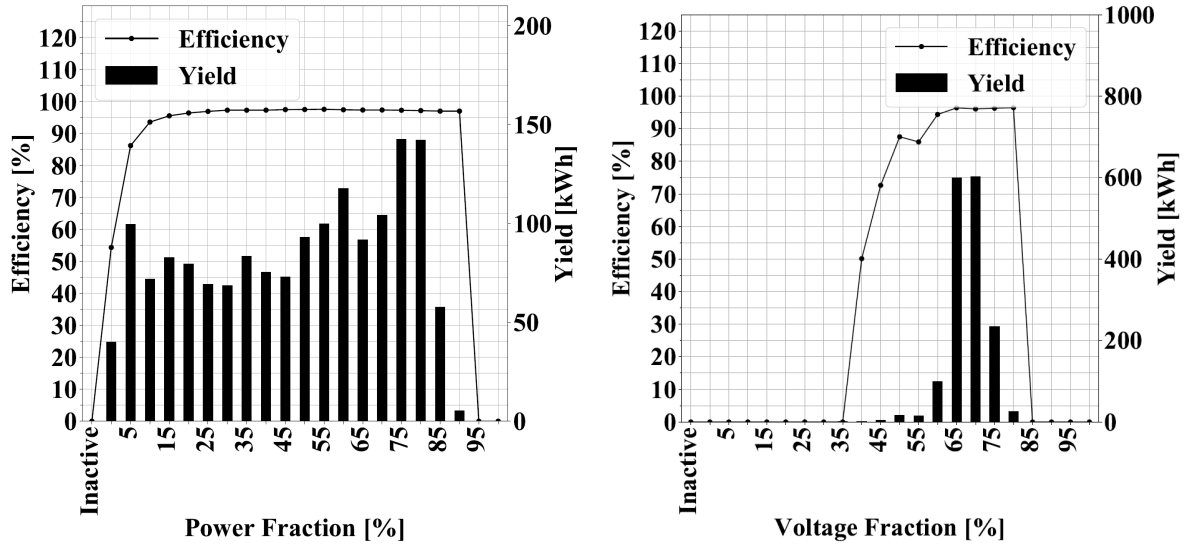

Figure D.11: *Plots of the efficiency curve together with the yield (bars) for system 15 grouped by power fraction voltage fraction ($\frac{P}{P_{rated}}$) and voltage fraction ($\frac{V}{V_{max,op}}$)*

E A selection of hourly PR plots

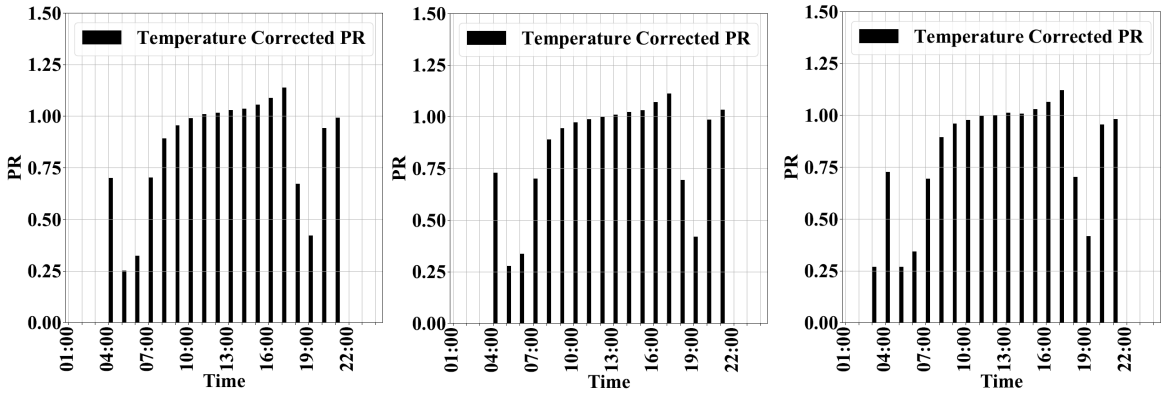

(a) *29.06.18* (b) *30.06.18* (c) *01.07.18*

Figure E.1: *Plots of PR_{corr} of system 2 in three consecutive days in June and July.*

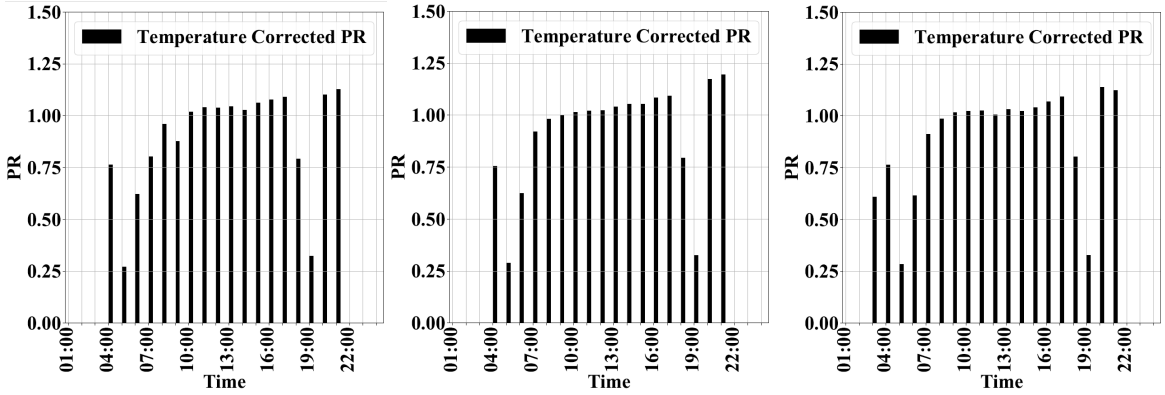

(a) *29.06.18* (b) *30.06.18* (c) *01.07.18*

Figure E.2: *Plots of PR_{corr} of system 6 in three consecutive days in June and July.*

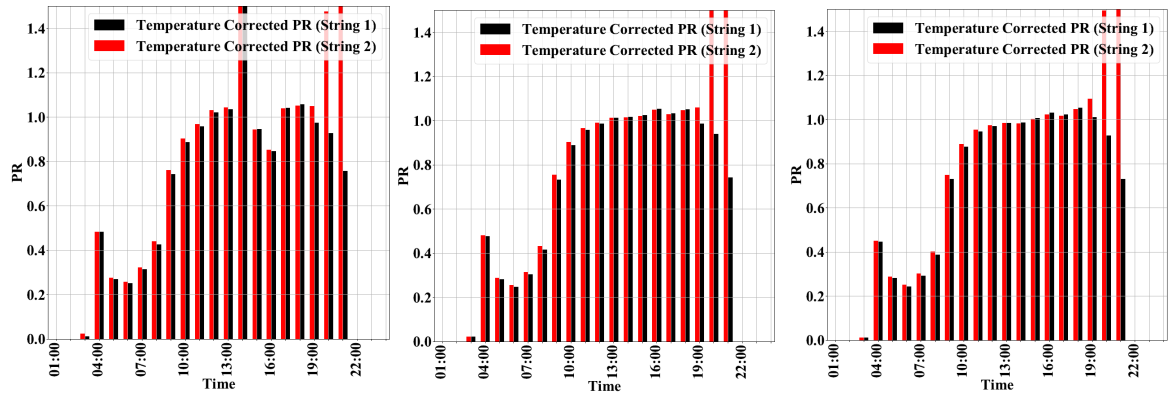

(a) *29.06.18* (b) *30.06.18* (c) *01.07.18*

Figure E.3: *Plots of PR_{corr} of system 7 in three consecutive days in June and July.*

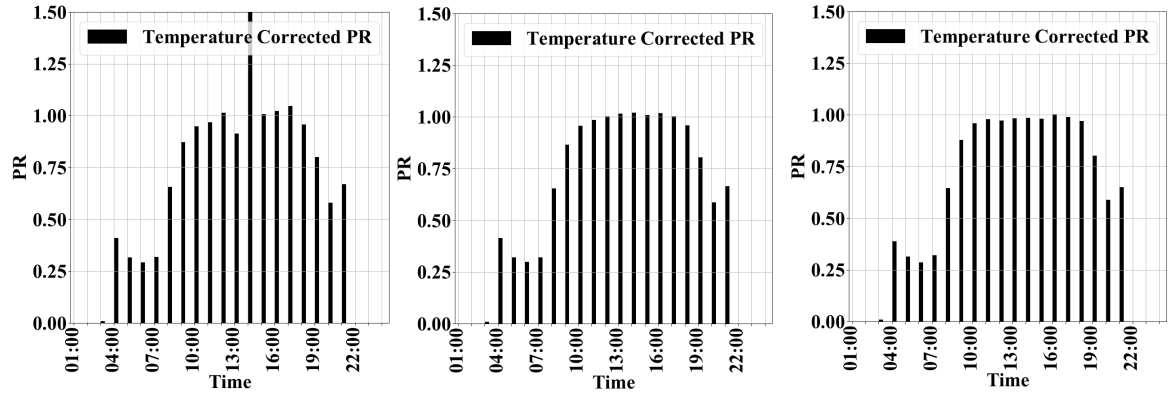

(a) *29.06.18* (b) *30.06.18* (c) *01.07.18*

Figure E.4: *Plots of PR_{corr} of system 8 in three consecutive days in June and July.*

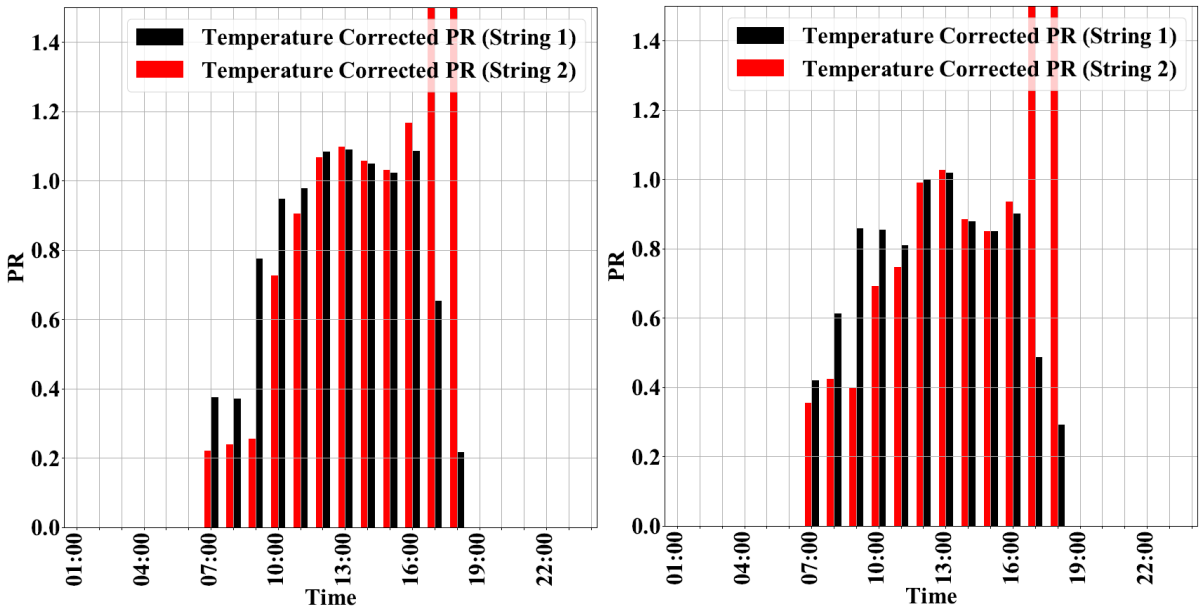

(a) *23.03.19* (b) *28.03.19*

Figure E.5: *Plots of PR_{corr} of system 9 in two days in March, 2019.*

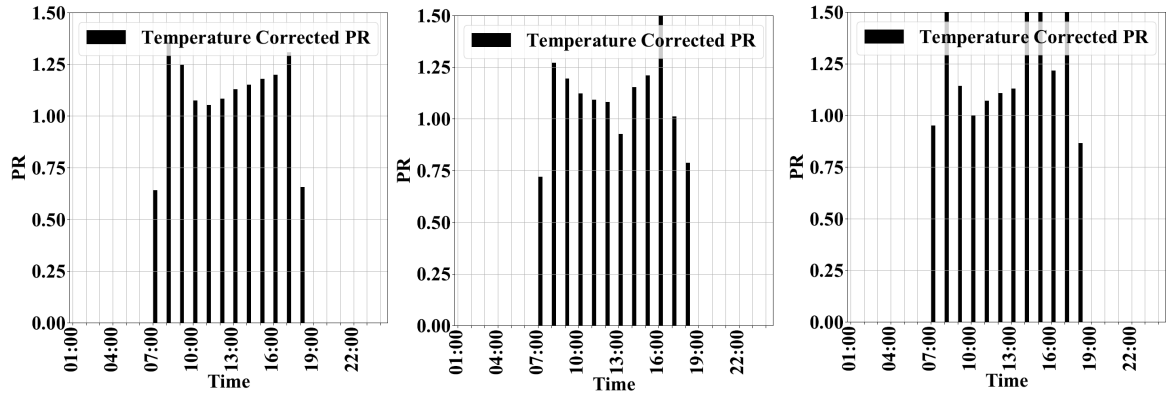

(a) *23.03.19* (b) *24.03.19* (c) *25.03.19*

Figure E.6: *Plots of PR_{corr} of system 14 in three days consecutive in March, 2019.*

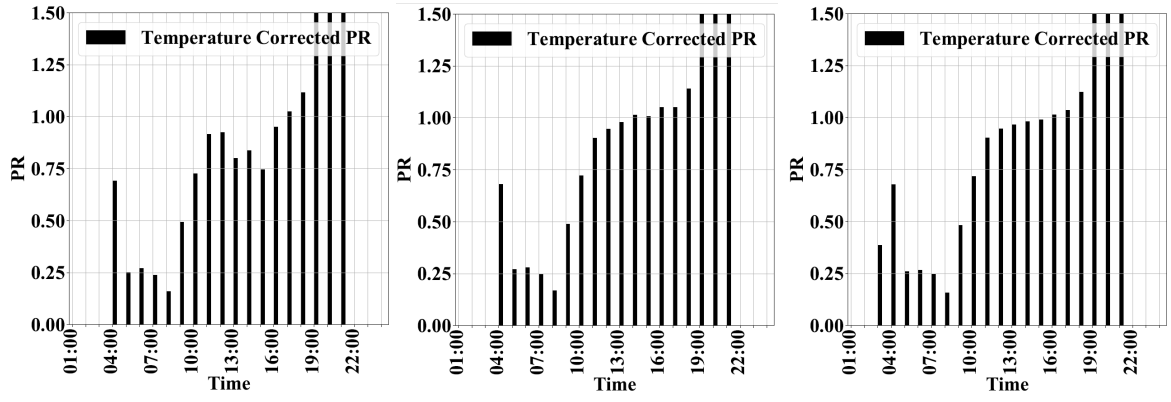

(a) *29.06.18* (b) *30.06.18* (c) *01.07.18*

Figure E.7: *Plots of PR_{corr} of system 15 in three consecutive days in June and July.*

Norges miljø- og biovitenskapelige universitet
Noregs miljø- og biovitskapelege universitet
Norwegian University of Life Sciences

Postboks 5003
NO-1432 Ås
Norway